2013

Preparation and characterization of cellulose nanoparticles and their application in biopolymeric nanocomposites

Jingquan Han
Louisiana State University and Agricultural and Mechanical College, hjingq1@tigers.lsu.edu

PREPARATION AND CHARACTERIZATION OF CELLULOSE NANOPARTICLES AND THEIR APPLICATION IN BIOPOLYMERIC NANOCOMPOSITES

A Dissertation

Submitted to the Graduate Faculty of the
Louisiana State University and
Agricultural and Mechanical College
in partial fulfillment of the
requirements for the degree of
Doctor of Philosophy

in

The School of Renewable Natural Resources

by
Jingquan Han
B.S., Northeast Forestry University, July 2007
M.S., Northeast Forestry University, June 2009
December 2013

ACKNOWLEDGEMENTS

Many people contributed to the successful completion of this dissertation. First of all, I cordially appreciate my committee chair, Dr. Qinglin Wu for his kindness, guidance, advice, wisdom, encouragement and support throughout my PhD program. He inspired me with his enthusiasm for research and gave me independence to explore new ideas on my own. He also encouraged and financed my attendance at several conferences. His talent and diligence have thoroughly motivated me and will shine on me in my future career. In addition, the financial support from Chinese Scholarship Council (CSC No.: 2009660015) is greatly appreciated.

I also greatly appreciate my committee members, Dr. Ioan I. Negulescu, Dr. Sun Joseph Chang, Dr. Alfred D. French for their inspiring and encouraging guidance, invaluable advice in my research, and their insightful comments during the entire process of this dissertation. Their suggestions and advices were constructive in my research project. It has been an honor and privilege for me to have them on my committee.

I acknowledge my laboratory fellows and friends, Dr. Runzhou Huang, Dr. Birm June Kim, Mr. Kai Chi, Mr. Kunlin Song, Dr. Chengjun Zhou, Mr. Tian Liu, Dr. Zhanhua Huang, Dr. Xiaodong Zhu, Dr. Yubo Tao, Miss Min Yu, Miss Huan Zhang, Miss Huiyuan Li and Dr. Peng Li for their help on experiments and friendships. Special thanks go to Dr. Alfred D. French for his suggestions and discussions on my research.

Last but not least, I thank all my family for their support and especially my wonderful wife Yiying Yue for her endless encouragement, recommendations, devotion, sacrifice and endless love. She is the one who should get the credit for each and every piece of success that I have achieved. She deserves it. I thank God for giving me the best wife of the world and a very happy life.

TABLE OF CONTENTS

LIST OF TABLES

LIST OF FIGURES

NOMENCLATURE

$[BMIM]^+[Cl]^-$: 1-butyl-3-methylimidazolium chloride

CI: crystallinity index

CNC I: cellulose nanocrystal with I crystalline allomorphs

CNC II: cellulose nanocrystal with II crystalline allomorphs

CNF I: cellulose nanofiber with I crystalline allomorphs

CNF II: cellulose nanofiber with II crystalline allomorphs

CNP: cellulose nanoparticle

C-RCNs: reconstituted cellulose II nanoparticles from cotton

CY: char yield

DSC: differential scanning calorimetry

DTG: derivative thermal gravimetric

FE-SEM: field emission scanning electron microscopy

FTIR: fourier transform infrared spectrometry

HPH: high-Pressure homogenization

ILs: ionic liquids

LVR: linear viscoelastic region

MCC: microcrystalline cellulose

M-RCNs: reconstituted cellulose II nanoparticles from microcrystalline cellulose

NaOH: Sodium hydroxide

PB: polyvinyl alcohol-borax hydrogel

PB-CNC I: cellulose I nanocrystal-reinforced polyvinyl alcohol-borax hydrogel

PB-CNF I: cellulose I nanofiber-reinforced polyvinyl alcohol-borax hydrogel

PB-CNC II: cellulose II nanocrystal-reinforced polyvinyl alcohol-borax hydrogel

POM: polarized optical microscopy

PVA: polyvinyl alcohol

RCNs: regenerated cellulose nanoparticle

SEM: scanning electron microscope

TEM: transmission electron microscopy

TGA: thermogravimetric analysis

XPS: X-ray photoelectron spectroscopy

XRD: X-ray diffraction

WXRD: wide-angle X-ray diffraction

ABSTRACT

Regenerated cellulose nanoparticles (RCNs) including both elongated fiber and spherical structures were prepared from microcrystalline cellulose (MCC) and cotton using 1-butyl-3-methylimidazolium chloride followed by high-pressure homogenization. The RCN has a two-step pyrolysis, different from raw MCC and cotton that had a one-step process. The crystalline structure of RCNs was cellulose II in contrast to the cellulose I form of the starting materials. Also, the RCNs have decreased crystallinity and crystallite size. The elongated RCNs produced from cotton and MCC had average lengths of 123 $\pm$34 and 112 $\pm$42 nm, and mean widths of 12 $\pm$5 and 12 $\pm$3 nm, respectively. The average diameter of spherical RCNs from MCC was 118 $\pm$ 32 nm.

Cellulose nanocrystals and cellulose nanofibers with I and II crystalline allomorphs (designated as CNC I, CNC II, CNF I, and CNF II) were isolated from bleached wood fibers by alkaline pretreatment and acid hydrolysis. The effects of concentration, particle size, surface charge, and crystal structure on the lyophilization-induced self-assembly of cellulose particles in aqueous suspensions were studied. Within the concentration range of 0.5 to 1.0 wt %, cellulose particles self-organized into lamellar structured foam composed of aligned membrane layers with widths between 0.5 and 3 μ m. At 0.05 wt %, CNC I, CNF I, CNC II, and CNF II self-assembled into oriented ultrafine fibers with mean diameters of 0.57, 1.02, 1.50, and 1.00 μ m, respectively.

Cellulose nanoparticle (CNP) reinforced Polyvinyl alcohol-borax (PB) hydrogels were prepared through a facile approach in an aqueous medium. The obtained stiff, high-water-capacity (~96%), low-density (~1.1g/cm^3), translucence hydrogels exhibited birefringence textures. These free-standing, high elasticity and mouldable hydrogels also exhibited self-recovery under continuous step strain and thermo-reversibility under temperature sweep. The

rheological tests and compression measurements confirmed the incorporation of well-dispersed CNPs to PB system significantly enhanced the compressive strength, viscoelasticity and stiffness of the hydrogels. Highly-crystalline CNPs not only tangled with PVA chains though numerous hydrogen bonds, but formed chemically crosslinked complexes with borax ions as well, thus acting as multifunctional crosslinking agents and nanofillers to physically and chemically bridge the 3D network hydrogels.

CHAPTER 1 INTRODUCTION

1.1 BACKGROUND

Cellulose, a linear polysaccharide composed of β–1–4–linked D-glucopyranose repeating units, exhibits a number of desirable properties and has become one of the most promising renewable polymeric materials. Besides the application of unmodified cellulose products, cellulose can be converted into regenerated cellulosic materials, which have been widely applied in many fields (Jiang et al. 2012; Mahmoudian et al. 2012). However, due to its partly crystalline structure, closely packed chains with van der Waals interactions, and numerous inter- and intra-molecular hydrogen bonds, cellulose cannot be dissolved in water or most conventional organic solvents. This poses a formidable obstacle to increased utilization of cellulose. Therefore, it is essential to further explore suitable cellulose dissolution methods to expedite novel applications of regenerated cellulose (Jiang et al. 2012; Lan et al. 2011; Mahmoudian et al. 2012). Recently, a new type of solvent, ionic liquids (ILs), has been gaining interest because of their potential to be eco-friendly. They have characteristics such as low melting point, low flammability, non-volatility, non-explosiveness, thermal stability and ease of recycling, and thus can possibly replace conventional volatile organic solvents (Gutowski et al. 2003; Mahmoudian et al. 2012). Structurally, ILs are composed of ions, but exist as liquids at relatively low temperatures (usually lower than 100^{o}C). The dissolution and regeneration of cellulose with ILs can promote the utilization of cellulosic materials by combining two main green chemistry principles: using environmentally preferable solvents and bio-renewable feed-stocks (Zhu et al. 2006). Dissolution in ILs has the potential to become a crucial pretreatment for enhancing enzymatic hydrolysis of cellulose because it can be done under mild condition (Kuo and Lee 2009). The desirable properties of ILs can be tailored by judicious variation of the chemical structures of the cation

and/or the anion of the ILs (Azubuike et al. 2012). The most common IL for cellulose dissolution is 1-butyl-3-methylimidazolium chloride ($[BMIM]^+[Cl]^-$), producing a cellulose solution without derivation (Lan et al. 2011; Swatloski et al. 2002). As is always found with dissolution and regeneration of cellulose (Mansikkamaki et al. 2007; Zhao et al. 2007), the crystal structure of cellulose that is dissolved in $[BMIM]^+[Cl]^-$ takes the usual cellulose II allomorph upon regeneration (Quan et al. 2010). Hence, the fundamental research needs to be conducted in order to characterize in detail the cellulose II products regenerated from ILs.

Cellulose nanocrystals (CNCs) and cellulose nanofibers (CNFs) have recently received a considerable attention due to their intrinsically appealing properties (Habibi et al. 2010). The rod-like CNCs and needle-like CNFs are mainly prepared by controlled acid hydrolysis of native cellulose sources. For wood, mean width and length of CNCs are 5 to 10 nm and 100 to 300 nm, respectively, and the CNFs are 5 to 50 nm in width and several micrometers in length (Beck-Candanedo et al. 2005; Bondeson et al. 2006). In order to expand their applications, much work has concentrated on the drying process of CNC and CNF aqueous suspensions (Peng et al. 2012). Recently, research has been attempted to use the freeze-drying technique to fabricate biomimetic cellulose foam with different microstructures and properties (Svagan et al. 2008). The lyophilization process consists of two important steps, i.e., growing of the ice crystals (freezing) and sublimation of the ice molecules (drying). Upon freezing cellulose aqueous suspensions, water is frozen into ice crystals and then most cellulose particles above the critical particle size are trapped by the moving water-ice front and confined into the interstitial spaces between ice crystals. The final structure of cellulose foam is formed as ice crystals are sublimated during the drying step (Deville and Nalla 2006; Svagan et al. 2008). Therefore, in addition to the freezing conditions, the particle size, surface charge, suspension concentration, and their relationship with

the self-assembly behavior of cellulose particles are theoretically related to the morphology and properties of the final foam. Lee and Deng (Lee and Deng 2011) reported the effects of high concentrations (above 1.0 wt%) on the microstructure and mechanical properties of cellulose microfibril foams. However, little is known about the self-assembling behavior of cellulose particles during the freeze-drying process at low suspension concentrations (e.g., below 1.0 wt%).

Polyvinyl alcohol (PVA) is one of the most important synthetic water-soluble polymers produced in the world. Because of the hydroxyl groups present in each repeating molecular unit, PVA possesses strong hydrophilic and hydrogen bonding characteristics. It can react with many types of functional groups and form chemically and/or physically crosslinked hydrogels. The PVA-based hydrogels are biocompatible, biodegradable, non-toxic and non-carcinogenic (Asher et al. 2008; Kobayashi et al. 2005). Current applications of PVA-based hydrogels include bioactuators, tissue scaffolding, artificial meniscus and cornea, aortic heart valve and wound dressing (Lin et al. 2000; VI et al. 2003). Borax ($Na_2B_4O_7 \cdot 10H_2O$), known as a non-toxic food additive, has been successfully used as a chemical crosslinking agent for PVA. Addition of a small amount of borax to PVA can lead to a remarkable increase in viscoelasticity of the PVA aqueous solutions. This is attributed to the formation of complexes between borate ions and hydroxyl functional groups of PVA, which act as a temporary cross-linker between PVA molecular chains (Inoue and Osaki 1993). Similar behavior has also been reported for polysaccharide (e.g., between borax and konjac galactomannan) (Gao et al. 2008; Koike et al. 1995). The hydrogels formed by PVA-borax complexation have received much attention because of their attractive physicochemical properties and wide applications, such as easel painting cleaning (Lin et al. 2005). However, However, most single-phase hydrogels are known to be soft and to have a low strain to failure (Yang et al. 2013a; Yang et al. 2013b). The weak mechanical

performance mainly arises from their low resistance to crack propagation and a lack of an efficient energy dissipation mechanism in the hydrogel network (Yang et al. 2012). Depending on the specific application, designing functional hydrogels requires them to at least possess sufficient mechanical strength, as well as to maintain their intrinsic properties (e.g., low density, water-retaining property, stimuli responsiveness and transparency). Consequently, the scope of hydrogel applications is often severely hindered by their poor mechanical behavior (Sun et al. 2012). To overcome this limitation, an intense effort is devoted to synthesizing tougher multi-phase hydrogels with improved mechanical properties. In order to enhance the mechanical strength and toughness of hydrogels, composite hydrogels have been prepared by incorporating nanoparticles, including carbon nanotubes, metallic particles, and clay (Shin et al. 2009). Due to their higher specific surface area, smaller particles afford a better interaction between fillers and polymer matrix, resulting in an enhancement effect in mechanical properties. Compared to most of current nanoparticles, cellulose nanoparticles (CNPs), including cellulose nanocrystals and cellulose nanofibers, are more favorable candidates, due to their renewability, high ratio of strength to weight, good processability, high water holding capacity, low density, low cost, non-toxicity and high crystallinity (Yang et al. 2013b; Zhang et al. 2011). CNCs and CNFs are isolated from cellulosic microfibrils through acid hydrolysis, where disordered or paracrystalline regions of cellulose are preferentially hydrolyzed over the crystalline regions. Depending on the acid hydrolysis conditions, the long cellulosic microfibrils undergo longitudinal cleavage and become stiff rod-like CNCs or entangled CNFs (Boluk et al. 2012; Yang et al. 2012). In our previous study, CNCs and CNFs with I and II crystalline allomorphs were successfully prepared using alkali pretreatment and/or sulfuric acid hydrolysis in combination with high-pressure homogenization (Han et al. 2013). A prerequisite for effective reinforcement of PVA hydrogels

using CNCs and CNFs is the uniform dispersion of the CNPs within the PVA aqueous suspension. CNPs do not flocculate and form homogeneous suspension or stable colloid in water because of negatively charged sulfate ester groups introduced onto crystallite surfaces during H_2SO_4 hydrolysis (Abitbol et al. 2011). Rod-shaped CNPs can further generate birefringence and ordered liquid phases at sufficiently high concentrations in aqueous mediums due to the liquid crystalline nature and anisotropic alignment of CNC I and CNF I in the aqueous dispersions (Boluk et al. 2012). Similar to PVA, CNPs are hydrophilic and polar in nature. In this regard, they are expected to be well-suited to blend with PVA in aqueous system. On the other hand, high Young's modulus, tensile strength and elastic modulus of 134, 10, and 100 GPa for cellulose crystal region have been reported (Gawryla et al. 2009; Yang et al. 2013a; Yang et al. 2013b). The combination of high mechanical performance with low density (~1.5 g/cm^3) and high aspect ratio makes them ideal nanofillers for hydrogels. However, a simple incorporation of pristine PVA into CNP suspension cannot lead to a hydrogel with good mechanical properties due to the absence of chemical cross-linker (Zhang et al. 2011). Therefore, Abitbol et al. lately used cyclic freeze-thaw method to crosslink PVA (15 wt%) and CNPs (1.5-3.0 wt%) at high loading levels to produce composite hydrogels (Abitbol et al. 2011). However, this method requires high PVA and cellulose content as well as a series of time-consuming cyclic processes.

Application of the hydrogels in many fields requires a fundamental understanding of their viscoelastic properties. Among those techniques that have been used to investigate the gelation kinetics of PB aqueous system, dynamic rheological techniques have attracted strong interest as a powerful and effective approach to study the supramolecular structure of hydrogels since in situ experiments are relatively facile to perform during the gelation process (Shi et al. 2012). The network structure and the cross-linking density are key factors derived from the rheological

characteristics of the hydrogels (Kjøniksen and Nyström 1996). The linear viscoelastic behavior in dynamic experiments of miscible gelling polymer systems can continuously monitor the development of cross-links (chemical and/or physical) and supramolecular complexes in hydrogel without disrupting gel structure, and they can further reflect the miscibility of polymer blends, supramolecular structure and cross-linking density of hydrogels in stages. As a result, effort has been devoted to the rheology study of PVA-borate complex aqueous systems over the past several decades (Angelova et al. 2011; Carretti et al. 2009). The effects of polymer concentration, molecular weight and temperature on the dynamic viscoelasticity of PVA in aqueous borax solutions were discussed (Koike et al. 1995). The thermo-dynamic, structural, and dynamic features of cross-linked PVA hydrogels and the corresponding semidilute polymer solutions were also reported (Kjøniksen and Nyström 1996). The crosslinking mechanism of borate ion with PVA chains was known to be a "di-diol" complexation, which was formed between one borate ion and two diol units. PB aqueous system rheologically behaved like elastic solids at high frequencies and like viscous liquids at low frequencies. The short relaxation time and small amount of energy required to break and reform the cross-links accounted for the "slime" consistency of these materials (Angelova et al. 2011). Above-mentioned studies indicate that dynamic rheology techniques can distinguish appropriate gelation conditions for the fabrication of PB hydrogels with desired properties. Regarding the industrial potential in the processing of related materials, the knowledge of the dynamic rheological behavior of PB-based system is very useful in equipment selection and quality control (Gouvea et al. 2009). However, to the best of our knowledge, we are unaware of any reports on the gelation mechanism and rheological viscoelasticity of PVA-borax-CNP complexes in an aqueous system. For instance, the effects of different CNPs on the rheological features of PB aqueous systems have not been

addressed. It is possible that the physically and chemically crosslinked hydrogels can exhibit some unique viscoelastic properties.

1.2 OBJECTIVES

The objectives of the research described in this work are:

1) To study the process of dissolving and regenerating cotton and MCC cellulose using $[BMIM]^+[Cl]^-$, evaluate the properties of regenerated cellulose II nanoparticles from MCC and cotton, and characterize the morphology, crystal structure, functional groups and thermal properties of the regenerated cellulose nanoparticles prepared with $[BMIM]^+[Cl]^-$.

2) To extract size-controllable cellulose particles with cellulose I and II structures from bleached wood pulp using alkali treatment and/or acid hydrolysis in combination with homogenization process, compare the crystal structure, crystallinity, hydrogen bonding patterns, surface charge, dispersion state, liquid-crystalline properties, optical transmittance and morphology of cellulose particles produced using different methods, investigate the effects of suspension concentrations, particle size, crystal structure, and surface charge on the self-assembling behavior of cellulose particles during the freeze-drying process, and describe the liquid-crystalline properties, supramolecular structure development, and self-assembling mechanism of cellulose particles during lyophilization, providing a fundamental guidance for the applications of cellulose nanoparticles as templates for layered scaffolds, filters, and storage materials.

3) To develop a facile synthesis approach for the reinforcement of PVA hydrogels by incorporating three types of well-dispersed CNPs with the presence of non-toxic borax cross-linker, produce high-water-capacity, low density and rubbery hydrogels with enhanced mechanical performance and excellent optical transmittance, and investigate the effects of

particle size, aspect ratio, crystal structure, and crystallinity of different CNPs on the density, water content, optical transmittance and compression property of the hydrogels.

4) To characterize the dynamic rheological behavior of the CNP-PVA-borax hydrogels, explore the plausible mechanism for the multi-complexation among CNPs, PVA and borax for a better understanding of the relationship between 3D network structure and hydrogel properties, investigate the effects of particle size, aspect ratio, crystal structure, surface charge and minimum overlap concentration of different CNPs on the dynamic rheological properties and performance of the hydrogels, and demonstrate the self-healing ability and thermo-reversibility of as-prepared composite hydrogels.

1.3 ORGANIZATION OF DISSERTATION

Chapter 1 provides an overall introduction of this research and the structure of the dissertation.

Chapter 2 presents the results of the cellulose II nanoparticles regenerated from 1-butyl-3-methylimidazolium chloride.

Chapter 3 describes the effect of suspension concentration, particle size, crystal structure, and surface charge of cellulose nanoparticles on their self-assembling behavior during freeze-drying.

Chapter 4 describes the facile synthesis of high-water-content mouldable polyvinyl alcohol-borax hydrogels reinforced by well-dispersed cellulose nanoparticles and study of the physical and mechanical properties of the hydrogels.

Chapter 5 describes the dynamic rheological properties and hydrogel formation mechanism of the high-water-content polyvinyl alcohol-borax hydrogels reinforced by well-dispersed cellulose nanoparticles.

Chapter 6 provides overall conclusions of the dissertation.

1.4 REFERENCES

Abitbol T., Johnstone T., Quinn T. M. and Gray D. G. 2011. Reinforcement with cellulose nanocrystals of poly(vinyl alcohol) hydrogels prepared by cyclic freezing and thawing. *Soft Matter* 7:2373-2379.

Angelova L. V., Terech P., Natali I., Dei L., Carretti E. and Weiss R. G. 2011. Cosolvent Gel-like Materials from Partially Hydrolyzed Poly(vinyl acetate)s and Borax. *Langmuir* 27:11671-11682.

Asher S. A., Kimble K. W. and Walker J. P. 2008. Enabling Thermoreversible Physically Cross-Linked Polymerized Colloidal Array Photonic Crystals. *Chemistry of Materials* 20:7501-7509.

Azubuike C. P., Rodriguez H., Okhamafe A. O. and Rogers R. D. 2012. Physicochemical properties of maize cob cellulose powders reconstituted from ionic liquid solution. *Cellulose* 19:425-433.

Beck-Candanedo S., Roman M. and Gray D. G. 2005. Effect of reaction conditions on the properties and behavior of wood cellulose nanocrystal suspensions. *Biomacromolecules* 6:1048-1054.

Boluk Y., Zhao L. Y. and Incani V. 2012. Dispersions of Nanocrystalline Cellulose in Aqueous Polymer Solutions: Structure Formation of Colloidal Rods. *Langmuir* 28:6114-6123.

Bondeson D., Mathew A. and Oksman K. 2006. Optimization of the isolation of nanocrystals from microcrystalline cellulose by acid hydrolysis. *Cellulose* 13:171-180.

Carretti E., Grassi S., Cossalter M., Natali I., Caminati G., Weiss R. G., Baglioni P. and Dei L. G. 2009. Poly(vinyl alcohol)-Borate Hydro/Cosolvent Gels: Viscoelastic Properties, Solubilizing Power, and Application to Art Conservation. *Langmuir* 25:8656-8662.

Deville S. and Nalla R. K. 2006. Freezing as a path to build complex composites (vol 312, pg 515, 2006). *Science* 312:1312-1312.

Gao S. J., Guo J. M. and Nishinari K. 2008. Thermoreversible konjac glucomannan gel crosslinked by borax. *Carbohydrate Polymers* 72:315-325.

Gawryla M. D., van den Berg O., Weder C. and Schiraldi D. A. 2009. Clay aerogel/cellulose whisker nanocomposites: a nanoscale wattle and daub. *Journal of Materials Chemistry* 19:2118-2124.

Gouvea M. R., Ribeiro C., de Souza C. F., Marvila-Oliveira I., Lucyszyn N. and Sierakowski M. R. 2009. Rheological behavior of borate complex and polysaccharides. *Materials Science & Engineering C-Biomimetic and Supramolecular Systems* 29:607-612.

Gutowski K. E., Broker G. A., Willauer H. D., Huddleston J. G., Swatloski R. P., Holbrey J. D. and Rogers R. D. 2003. Controlling the Aqueous Miscibility of Ionic Liquids: Aqueous Biphasic Systems of Water-Miscible Ionic Liquids and Water-Structuring Salts for Recycle, Metathesis, and Separations. *Journal of the American Chemical Society* 125:6632-6633.

Habibi Y., Lucia L. A. and Rojas O. J. 2010. Cellulose Nanocrystals: Chemistry, Self-Assembly, and Applications. *Chemical Reviews* 110:3479-3500.

Han J., Zhou C., Wu Y., Liu F. and Wu Q. 2013. Self-Assembling Behavior of Cellulose Nanoparticles during Freeze-Drying: Effect of Suspension Concentration, Particle Size, Crystal Structure, and Surface Charge. *Biomacromolecules* 14:1529-1540.

Inoue T. and Osaki K. 1993. Rheological Properties of Poly(Vinyl Alcohol)/Sodium Borate Aqueous-Solutions. *Rheologica Acta* 32:550-555.

Jiang G. S., Huang W. F., Li L., Wang X., Pang F. J., Zhang Y. M. and Wang H. P. 2012. Structure and properties of regenerated cellulose fibers from different technology processes. *Carbohydrate Polymers* 87:2012-2018.

Kjøniksen A.-L. and Nyström B. 1996. Effects of Polymer Concentration and Cross-Linking Density on Rheology of Chemically Cross-Linked Poly(vinyl alcohol) near the Gelation Threshold. *Macromolecules* 29:5215-5222.

Kobayashi M., Chang Y. S. and Oka M. 2005. A two year in vivo study of polyvinyl alcohol-hydrogel (PVA-H) artificial meniscus. *Biomaterials* 26:3243-3248.

Koike A., Nemoto N., Inoue T. and Osaki K. 1995. Dynamic Light-Scattering and Dynamic Viscoelasticity of Poly(Vinyl Alcohol) in Aqueous Borax Solutions .1. Concentration-Effect. *Macromolecules* 28:2339-2344.

Kuo C. H. and Lee C. K. 2009. Enhancement of enzymatic saccharification of cellulose by cellulose dissolution pretreatments. *Carbohydrate Polymers* 77:41-46.

Lan W., Liu C. F., Yue F. X., Sun R. C. and Kennedy J. F. 2011. Ultrasound-assisted dissolution of cellulose in ionic liquid. *Carbohydrate Polymers* 86:672-677.

Lee J. and Deng Y. L. 2011. The morphology and mechanical properties of layer structured cellulose microfibril foams from ice-templating methods. *Soft Matter* 7:6034-6040.

Lin H.-L., Liu Y.-F., Yu T. L., Liu W.-H. and Rwei S.-P. 2005. Light scattering and viscoelasticity study of poly(vinyl alcohol)–borax aqueous solutions and gels. *Polymer* 46:5541-5549.

Lin H.-L., Yu T. L. and Cheng C. H. 2000. Reentrant behavior of poly(vinyl alcohol)-borax semidilute aqueous solutions. *Colloid and Polymer Science* 278:187-194.

Mahmoudian S., Wahit M. U., Ismail A. F. and Yussuf A. A. 2012. Preparation of regenerated cellulose/montmorillonite nanocomposite films via ionic liquids. *Carbohydrate Polymers* 88:1251-1257.

Mansikkamaki P., Lahtinen M. and Rissanen K. 2007. The conversion from cellulose I to cellulose II in NaOH mercerization performed in alcohol-water systems: An X-ray powder diffraction study. *Carbohydrate Polymers* 68:35-43.

Peng Y. C., Gardner D. J. and Han Y. S. 2012. Drying cellulose nanofibrils: in search of a suitable method. *Cellulose* 19:91-102.

Quan S. L., Kang S. G. and Chin I. J. 2010. Characterization of cellulose fibers electrospun using ionic liquid. *Cellulose* 17:223-230.

Shi X. W., Lu A., Cai J., Zhang L. N., Zhang H. M., Li J. and Wang X. H. 2012. Rheological Behaviors and Miscibility of Mixture Solution of Polyaniline and Cellulose Dissolved in an Aqueous System. *Biomacromolecules* 13:2370-2378.

Shin M. K., Spinks G. M., Shin S. R., Kim S. I. and Kim S. J. 2009. Nanocomposite Hydrogel with High Toughness for Bioactuators. *Advanced Materials* 21:1712-+.

Sun J. Y., Zhao X. H., Illeperuma W. R. K., Chaudhuri O., Oh K. H., Mooney D. J., Vlassak J. J. and Suo Z. G. 2012. Highly stretchable and tough hydrogels. *Nature* 489:133-136.

Svagan A. J., Samir M. A. S. A. and Berglund L. A. 2008. Biomimetic foams of high mechanical performance based on nanostructured cell walls reinforced by native cellulose nanofibrils. *Advanced Materials* 20:1263-+.

Swatloski R. P., Spear S. K., Holbrey J. D. and Rogers R. D. 2002. Dissolution of cellose with ionic liquids. *Journal of the American Chemical Society* 124:4974-4975.

Vladimir L., Galaev I. Y., Plieva F. M., Savinal I. N., Jungvid H. and Mattiasson B. 2003. Polymeric cryogels as promising materials of biotechnological interest. *Trends in Biotechnology* 21:445-451.

Yang J., Han C. R., Duan J. F., Ma M. G., Zhang X. M., Xu F. and Sun R. C. 2013a. Synthesis and characterization of mechanically flexible and tough cellulose nanocrystals-polyacrylamide nanocomposite hydrogels. *Cellulose* 20:227-237.

Yang J., Han C. R., Duan J. F., Ma M. G., Zhang X. M., Xu F., Sun R. C. and Xie X. M. 2012. Studies on the properties and formation mechanism of flexible nanocomposite hydrogels from cellulose nanocrystals and poly(acrylic acid). *Journal of Materials Chemistry* 22:22467-22480.

Yang J., Han C. R., Duan J. F., Xu F. and Sun R. C. 2013b. Mechanical and Viscoelastic Properties of Cellulose Nanocrystals Reinforced Poly(ethylene glycol) Nanocomposite Hydrogels. *Acs Applied Materials & Interfaces* 5:3199-3207.

Zhang W., Yang X. L., Li C. Y., Liang M., Lu C. H. and Deng Y. L. 2011. Mechanochemical activation of cellulose and its thermoplastic polyvinyl alcohol ecocomposites with enhanced physicochemical properties. *Carbohydrate Polymers* 83:257-263.

Zhao H. B., Kwak J. H., Wang Y., Franz J. A., White J. M. and Holladay J. E. 2007. Interactions between cellulose and N-methylmorpholine-N-oxide. *Carbohydrate Polymers* 67:97-103.

Zhu S. D., Wu Y. X., Chen Q. M., Yu Z. N., Wang C. W., Jin S. W., Ding Y. G. and Wu G. 2006. Dissolution of cellulose with ionic liquids and its application: a mini-review. *Green Chemistry* 8:325-327.

CHAPTER 2 CHARACTERIZATION OF CELLULOSE II NANOPARTICLES REGENERATED FROM 1-BUTYL-3-METHYLIMIDAZOLIUM CHLORIDE[1]

2.1 INTRODUCTION

Cellulose, a linear polysaccharide composed of β–1–4–linked D-glucopyranose repeating units, exhibits a number of desirable properties and has become one of the most promising renewable polymeric materials. Besides the application of unmodified cellulose products, cellulose can be converted into regenerated cellulosic materials, which have been widely applied in many fields (Jiang et al. 2012; Mahmoudian et al. 2012). However, due to its partly crystalline structure, closely packed chains with van der Waals interactions, and numerous inter- and intra-molecular hydrogen bonds, cellulose cannot be dissolved in water or most conventional organic solvents. This poses a formidable obstacle to increased utilization of cellulose. Therefore, it is essential to further explore suitable cellulose dissolution methods to expedite novel applications of regenerated cellulose (Jiang et al. 2012; Lan et al. 2011; Mahmoudian et al. 2012).

A limited number of solvent systems have been investigated for cellulose dissolution and regeneration. These include N-methylmorpholine-N-oxide (NMMO) (Zhao et al. 2007), N-dimethylacetamide/lithium chloride (DMAC/LiCl) (Zhang et al. 2012), dimethyl sulfoxide/paraformaldehyde (DMSO/PF) (Jiang et al. 2012), 1,3-dimethyl-2-imidazolidinone/lithium chloride (DMI/LiCl) (Tamai et al. 2004), and NaOH/Urea solution (Kuo and Lee 2009). Among the solvents mentioned above, only the NMMO/water system is currently commercialized for manufacturing regenerated cellulose products, leading to the man-made cellulose with the generic name, Lyocell (Jiang et al. 2012). However, this solvent has some disadvantages associated with its application, including volatility, toxicity, formation of

[1] Reprint in part with permission from Carbohydrate Polymers
Han J. Q., Zhou C. J., French A. D., Han G. P., Wu Q. L. 2013. Characterization of cellulose II nanoparticles regenerated from 1-butyl-3-methylimidazolium chloride. *Carbohydrate Polymers* 94:773-81

byproducts, demand for harsh conditions, difficulty of solvent recovery, process instability, requirement of activation before dissolution, and investment in safety technology (Lan et al. 2011; Mahmoudian et al. 2012).

Recently, a new type of solvent, ionic liquids (ILs), has been gaining interest because of their potential to be eco-friendly. They have characteristics such as low melting point, low flammability, non-volatility, non-explosiveness, thermal stability and ease of recycling, and thus can possibly replace conventional volatile organic solvents (Gutowski et al. 2003; Mahmoudian et al. 2012). Structurally, ILs are composed of ions, but exist as liquids at relatively low temperatures (usually lower than 100 ◦ C). Rogers et al. (Swatloski et al. 2002) first showed that ILs could be nonderivatizing solvents for cellulose, and that cellulose could be dissolved in ILs without any pretreatment. So far, ILs have shown great potential for cellulose processing (Li et al. 2009) because they are efficient solvents for biomass that allow easy regeneration of cellulose upon anti-solvent addition. Compared to the NMMO/water system, dissolving cellulose in ILs is safer and easier, and the ILs can be recovered and reused after the cellulose regeneration by methods such as evaporation, ionic exchange, reverse osmosis, and salting out (Gutowski et al. 2003). By evaporating the anti-solvents, the recovery rate of $[BMIM]^+[Cl]^-$ can exceed 99.5% (Gutowski et al. 2003; Quan et al. 2010). For these reasons, ILs could replace organic solvents for a wide range of applications. Zhang and coworkers (Zhang et al. 2007) demonstrated that regenerated cellulose exhibited good mechanical properties. The dissolution and regeneration of cellulose with ILs can promote the utilization of cellulosic materials by combining two main green chemistry principles: using environmentally preferable solvents and bio-renewable feed-stocks (Zhu et al. 2006). Dissolution in ILs has the potential to become a crucial pretreatment for

enhancing enzymatic hydrolysis of cellulose because it can be done under mild condition (Kuo and Lee 2009).

The desirable properties of ILs can be tailored by judicious variation of the chemical structures of the cation and/or the anion of the ILs (Azubuike et al. 2012). The most common IL for cellulose dissolution is 1-butyl-3-methylimidazolium chloride ($[BMIM]^+[Cl]^-$), producing a cellulose solution without derivation (Lan et al. 2011; Swatloski et al. 2002). As is always found with dissolution and regeneration of cellulose (Mansikkamaki et al. 2007; Zhao et al. 2007), the crystal structure of cellulose that is dissolved in $[BMIM]^+[Cl]^-$ takes the usual cellulose II allomorph upon regeneration (Quan et al. 2010). ILs provide for versatile modification of the properties of cellulose II powders (Azubuike et al. 2012). Besides applications in smart materials, such as electro-activepaper (EAPap), sensors and actuators, regenerated cellulose II products have some preferable properties over cellulose I powders. Uses such as the recently introduced new filler/binder for solid dosage forms, and have been recommended as a second-generation multifunctional direct compression excipient, affording the manufacture of rapidly disintegrating tablets (Azubuike et al. 2012; Kumar et al. 2002). Hence, the fundamental research needs to be conducted in order to characterize in detail the cellulose II products regenerated from ILs.

In the present work, the process of dissolving and regenerating cotton and MCC cellulose using $[BMIM]^+[Cl]^-$ was studied. Regeneration was conducted by an anti-solvent strategy. The properties of regenerated cellulose II nanoparticles from MCC and cotton were evaluated and compared. The objective of this study was to characterize the morphology, crystal structure, functional groups and thermal properties of the regenerated cellulose nanoparticles pre- pared with $[BMIM]^+[Cl]^-$.

2.2 EXPERIMENTAL

2.2.1 Materials

An IL, 1-butyl-3-methylimidazolium chloride ($[BMIM]^+[Cl]^-$) with a melting point of 70 ℃ and a molecular weight of 174.67, was purchased from Sigma-Aldrich (St. Louis, MO). Cotton fabric was first cut into 4 × 20-mm fragments using a fabric cutter and then ground into smaller particles with a Wiley mill (Arthur H. Thomas Corp., Philadelphia, PA) to pass through an 80-mesh screen. The obtained particles were washed with ethanol and distilled water to remove impurities and then dried overnight in a vacuum oven (EQ-DZF-6020, MTI Corp.) at 60 ℃. Microcrystalline cellulose (MCC) (Avicel FD-100 MCC, FMC Biopolymer, Philadelphia, PA) was dried overnight in a vacuum oven at 60 ℃ before use. Acetone, ethanol and deionized water were purchased from Sigma–Aldrich (St. Louis, MO) and used without further processing. All the reagents and solvents used were of analytical grade.

2.2.2 Preparation of Cellulose Nanoparticles

2.2.2.1 Dissolution Process

Before use, solid state $[BMIM]^+[Cl]^-$, cotton and MCC were vacuum-dried at 70 ℃ for 12 h to remove the remnants of water. The presence of water can significantly impair cellulose solubility in IL by competing with the IL for hydrogen bonds to the cellulose microfibrils (Swatloski et al. 2002). After the $[BMIM]^+[Cl]^-$ totally melted into liquid, the dried MCC or cotton samples (5%, w/w) were slowly added into $[BMIM]^+[Cl]^-$ liquid with vigorous stirring. The heterogeneous mixture was immediately transferred into reaction vials. The vials were sealed and then heated in a silicone-oil bath at 125 ℃ for a period of 5 h. The dissolution process was carried out on a magnetic hot plate stirrer with safety control (Ret control, VISC., IKAMAG, CHEMGLASS-1990-35). The reaction temperature was controlled by a PT-100 temperature

sensor (PFA coated), which was directly inserted into the silicone-oil. The viscosity of the 5% (w/w) cellulose/$[BMIM]^+[Cl]^-$ solution appeared to decrease with reaction temperature and time. Therefore, in order to achieve an optimum stirring effect, the stirring velocity of the magnetic stir bar (PTFE) in each reaction vial was kept at 150 rpm during the first 2 h, and subsequently was kept constant at 350 rpm during the following 3 h. After the 5 h incubation period, a light amber-colored, translucent and viscous solution was formed, indicating the termination of the reaction between cellulose samples and $[BMIM]^+[Cl]^-$.

2.2.2.2 Regeneration Process

Distilled water was applied as the anti-solvent to stop the reaction and regenerate the cellulose nanoparticles from $[BMIM]^+[Cl]^-$. After the dissolution process, the cellulose/$[BMIM]^+[Cl]^-$ suspension was poured into an excess of distilled water and off-white precipitates formed immediately. After being stirred for about 20 min, the precipitates temporarily dispersed in the solution. The diluted suspension was filtered through filter paper (Grade-5, Whatman) under vacuum. The powdery off-white solids were then filtered and washed repeatedly with ethanol and water/acetone mixture. Subsequently, the filtered products were re-dispersed in distilled water and then centrifuged at 40 ℃ for 20 min with a constant speed of 12,000 rpm (Sorvall RC-5B Refrigerated Superspeed Centrifuge, Du Pont Instruments) to further remove the residual $[BMIM]^+[Cl]^-$. Thereafter, the precipitates, which were centrifuged three times, were eventually placed in regenerated cellulose dialysis tubes (Fisher Scientific, Pittsburgh, PA, USA) with a molecular weight cut off of 12,000–14,000 and dialyzed against distilled water for 24 h. After a series of filtering, centrifugation, and dialysis operations, hydrophilic $[BMIM]^+[Cl]^-$ was eliminated from the final product. The final concentration of the cellulose aqueous suspension was about 1% (w/w). The suspensions were stored at 10 ℃. Based

on the initial weight of the cellulose in $[BMIM]^+[Cl]^-$, the yield of the reconstituted cellulose II nanoparticles was estimated to be 30–40 wt.%. The RCNs prepared from MCC and cotton were designated as M-RCNs and C-RCNs, respectively.

2.2.2.3 Homogenization Process

To further enhance the dispersion of RCNs in water, mechanical homogenization was applied to the RCN suspension. The RCNs in aqueous suspension was processed through a high-pressure homogenizer (Microfluidizer M-110P, Microfluidics Corp., Newton, MA, USA) equipped with a pair of Z-shaped interaction chambers (one 200 μm ceramic, and one 87 μm diamond) under an operating pressure of 207 MPa (Yue et al. 2012). After ten passes through the homogenizer, the final RCN suspensions lacked visible aggregation and presented a pale bluish–purple color, indicating an excellent dispersity of nanoparticles in aqueous suspension. The homogenized M-RCNs and C-RCNs suspensions were stored at 10 ℃.

2.2.2.4 Freeze-drying Process

The M-RCN and C-RCN suspensions were quickly frozen by mixing acetone and dry ice in an ice pot. After being completely frozen, the samples were immediately transferred to a freeze-dryer (FreeZone plus 2.5 L, Labconco Corp., Kansas, MO, USA) and freeze-dried at a sublimating temperature of -88 ℃ under vacuum for three days to sublimate the solvent water directly from solid phase to gas phase. The final freeze-dried M-RCNs and C-RCNs were stored in plastic bags before performing further characterizations.

2.2.3 Characterizations

2.2.3.1 Wide-angle X-ray Diffraction (WXRD)

It is well known that the mechanical properties of cellulose products were strongly dependent on the crystallinity and crystal structure. To determine the crystal structure and

crystallinity, WXRD patterns of the untreated MCC, raw cotton, M-RCNs and C- RCNs were measured by Bruker/Siemens D5000X-ray automated powder X-ray diffractometer. Before testing, cotton and MCC powder samples were dried in a vacuum oven at 60 ℃ for 24 h to remove moisture. The M-RCN and C-RCN powder samples were obtained by freeze drying their corresponding suspensions. The WXRD data were generated by a diffractometer with Cu-Ka radiation (λ= 1.542 Å) at 40 kV and 30 mA over the range 2θ = 5 °–40 °, a size step of 0.02 °, and a time step of 2.0 s, (1.0 h per scan). The data were further analyzed using the MDI Jade 6.5.26 software (Serial#: MDI-R99691, Materials Data Inc., Livermore, CA). For each sample, the background was fitted with a software-generated cubic-spline function. Subsequently, the whole pattern was smoothed three times by a parabolic filter to reduce excess noise. The degree of crystallinity or crystallinity index (CI, %) for each sample was determined (Kumar et al. 2009; Li et al. 2010) by eq. 2.1 :

$$CI(\%) = 100\frac{I_{Max} - I_{Am}}{I_{Max}} \tag{2.1}$$

where I_{Max} is the maximum intensity of the principal peak, and I_{Am} is the intensity of diffraction attributed to amorphous cellulose.

The crystallite size of each sample perpendicular to the (2 0 0) planes, w (nm), was calculated by the Scherrer equation (eq. 2.2) (Liu et al. 2010):

$$w = \frac{K\lambda}{\beta\cos\theta} \tag{2.2}$$

where θ is the diffraction angle, K = 0.94 (correction factor), λ = 0.154 nm and β is the corrected angular width in radians at half maximum intensity of the [2 0 0] peak.

2.2.3.2 Fourier Transform Infrared Spectrometry (FTIR)

FTIR spectra of raw cotton, untreated MCC, C-RCNs and M- RCNs were measured with a Bruker FTIR analyzer (Tensor-27, Bruker Optics Inc., Billerica, MA) in the attenuated total reflectance (ATR) mode. All spectra were obtained in transmittance mode on a Zn/Se ATR crystal cell at room temperature. For each measurement, approximately 5 mg of the freeze-dried powder samples were pressed into the sample chamber of FTIR equipment and then 64 scans were taken with a resolution of 4 cm^{-1} and a spectral range of 4000–600 cm^{-1}. Three replicated measurements were recorded for each condition.

2.2.3.3 Transmission Electron Microscopy (TEM)

For the analysis, the concentration of the aqueous RCN suspensions was diluted from 1% to 0.01% (w/w). The diluted RCN suspension was treated with an ultrasonic bath (Model 3510, Branson, MS) prior to the TEM operation. A droplet (5 μl) of a diluted suspension of RCNs was negatively stained with a droplet (5 μl) of 2% (wt) uranyl acetate for about 2 min to enhance the contrast of the TEM images. Then the mixture was immediately deposited on the surface of a 400-mesh carbon-coated copper grid. The excess liquid on the grid was absorbed by using a tiny piece of filter paper to touch the edge of the grid. The morphology of obtained RCNs was characterized by using TEM (JEOL 100CX, JEOL, Inc., Peabody, MA) with an accelerating voltage of 80 kV. The distribution of RCN dimensions was evaluated from TEM images by using ImageJ 1.45k software (Rasband, W.S., ImageJ, U. S. National Institutes of Health, Bethesda, MD, http://imagej.nih.gov/ij/, 1997–2011). For each sample, one hundred particles were randomly selected and measured from several TEM images. The statistics and histograms of RCN dimensions were calculated and designed by Origin 8.5.0 software (SR1 b161, OriginLab Corp., Northampton, MA).

2.2.3.4 Thermogravimetric Analysis (TGA)

The degradation and dehydration of M-RCNs and C-RCNs were characterized by a thermo-gravimetric analyzer TGA (TA Q50 Instruments Inc., New Castle, DE) in a nitrogen atmosphere. Approximately 5 mg freeze-dried samples in a platinum pan were heated from 50 to 550 ℃ at a heating rate of 10 ℃/min under a nitrogen flow of 60 mL min^{-1}. Before the data acquisition segment, the sample was equilibrated at 25 ℃ for 5 min to obtain an isothermal condition. The weight-loss rate was obtained from derivative thermogravimetric (DTG) data.

2.3 RESULTS AND DISCUSSION

2.3.1 WXRD Analysis

The WXRD results showed that the regeneration of MCC and cotton resulted in significant changes in crystalline structure and crystallinity. The WXRD patterns of raw cotton and untreated MCC had a different structure compared to their corresponding regenerated cellulose nanoparticles produced by $[BMIM]^+[Cl]^-$ (Figure 2.1). Figure 2.1 shows that the WXRD pattern of native cotton sample had the three characteristic peaks of cellulose I crystal structure at 2θ = 14.9 °, 16.4 °, and 22.5 ° assigned to (1 $\bar{1}$ 0), (1 1 0), and (2 0 0), respectively. Upon dissolution and regeneration of cotton cellulose in the $[BMIM]^+[Cl]^-$ solvent system, the characteristic peaks were found at 2θ = 11.7 °(1 $\bar{1}$ 0), 20.1 °(1 1 0), and 21.6 °(0 2 0), which were attributed to the cellulose II crystalline allomorph. Nearly identical, cellulose I peaks were found for untreated MCC, and the same cellulose II peaks were found for regenerated MCC. This transformation from cellulose I to cellulose II because of dissolution and regeneration in $[BMIM]^+[Cl]^-$ agrees with earlier findings (Quan et al. 2010). Therefore, $[BMIM]^+[Cl]^-$ cannot only be used to extract cellulose nanoparticles from lignocellulosic biomass (as discussed below), but also help convert cellulose I to cellulose II during the process.

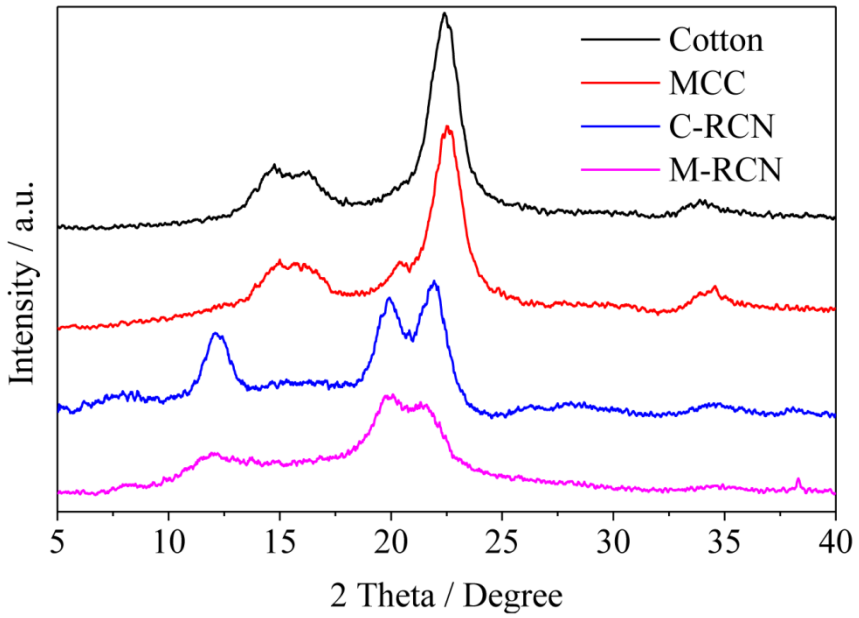

Figure 2.1 X-ray diffraction analysis of raw cotton, C-RCNs, untreated MCC and M-RCNs.

The crystallinity index is related to the strength and stiffness of fibers (Wang et al. 2007a; Wang et al. 2007b). After the dissolution and regeneration in $[BMIM]^{+}[Cl]^{-}$, the CI of the M-RCN and C-RCN were 52.1% and 61.8%, compared to the values of 76.7% and 80.0% for the native material, respectively. The similar decrease in CI values for reconstituted cellulose II powders was previously reported in the literatures (Azubuike et al. 2012; Jin et al. 2012; Kumar et al. 2002). Note that CI values for cellulose I and II cannot be directly compared, but in general comparable crystallinities of I and II should result in substantially lower CI values for cellulose I. This is because the 16 ° 2-θ position for measuring the amorphous intensity for cellulose II is considerably further from neighboring peaks than is the 18 ° 2-θ position for cellulose I peaks (AD French and M Santiago Citrón, manuscript in preparation.) Therefore, in the present case, with CI values for the RCN being lower than the untreated cotton and MCC samples, the crystallinities of the RCN much would be much lower. Lower CI implied a more amorphous structure, resulting in a more disordered structure, which was also observed in TEM images

below. Besides, the crystallite size of untreated MCC and cotton cellulose calculated perpendicular to the (2 0 0) planes were 54.6 and 56.9 nm, while the M-RCNs and C-RNCs had a crystallite size of 51.2 and 48.9 nm, respectively. The reduced crystallite sizes of RNCs were likely because of the incomplete growing of crystallites after regeneration (Gao et al. 2011). It was reported that the regenerated celluloses with lower CI are much easier to be enzymatically hydrolyzed to glucose, providing a better pretreated cellulose source for biodegradation process (Lee et al. 2009).

2.3.2 FTIR Analysis

The original cotton powders and C-RCNs obtained after treatment with $[BMIM]^+[Cl]^-$ showed similar FTIR spectra (Figure 2.2). For original cotton powders, the broad bands in the 3650–3000 cm^{-1} region were hydrogen-bond OH stretching vibrations and the peak at 2900 cm^{-1} corresponded to -CH stretching vibrations (Lu and Hsieh 2010). After $[BMIM]^+[Cl]^-$ treatment, the CH stretching vibration was shifted from 2901 cm^{-1} to 2893 cm^{-1}, the CO at C-6 stretching vibration was moved from 1033 cm^{-1} to 1025 cm^{-1}, and COC vibration at β-glycosidic linkage was switched from 897 cm^{-1} to 894 cm^{-1} (Table 2.1). The transformation could be explained by changes in the torsion angles of the glycosidic linkge (Ray and Sarkar 2001). These changes in the FTIR spectra of cotton cellulose upon reacting with $[BMIM]^+[Cl]^-$ indicated that $[BMIM]^+[Cl]^-$ transformed the cellulose crystal structure from I to II. The untreated MCC and M-RCNs obtained after treatment with $[BMIM]^+[Cl]^-$ showed similar FTIR spectra (Figure 2.2). Both MCC and M-RCNs spectra showed strong hydrogen bonded OH stretching vibrations in the range of 3600–3000 cm^{-1}. The $-CH_2-(C_6)-$ bending vibration and CH stretching vibration had peaks around 1430 and 2900 cm^{-1}, respectively. The peak at 1644 cm^{-1} was the O-H bending of adsorbed water. Some typical band characteristics of FTIR spectra related to the transition from

cellulose I to cellulose II were also observed in Table 2.1. In addition, the absence of $[BMIM]^+[Cl]^-$ peaks in the spectra of M-RCNs and C-RCNs indicated that the IL was completely removed during the purification sequence of filtering, centrifugation, and dialysis. Therefore, the FTIR data together with the XRD results confirmed that the crystal structure was transformed from cellulose I to cellulose II during the IL treatments.

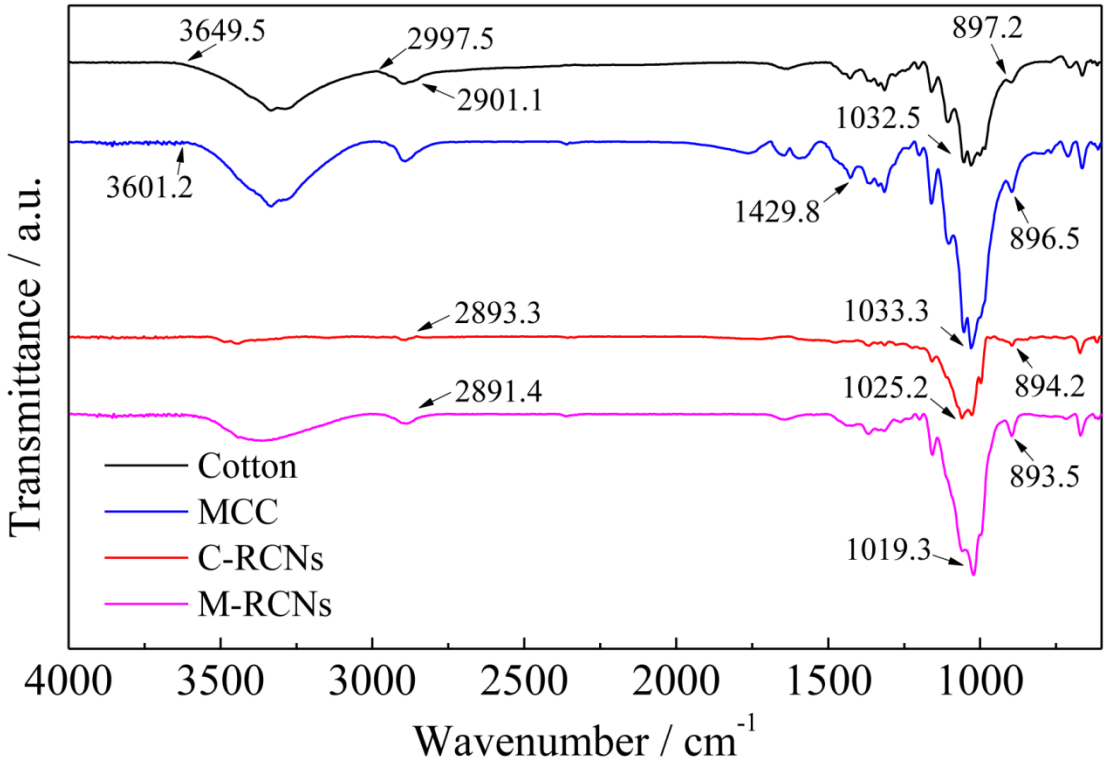

Figure 2.2 FTIR spectra of raw cotton, C-RCNs, untreated MCC and M-RCNs.

Table 2.1 Band characteristics of FTIR spectra related to transition from cellulose I to II

Raw Material	Peak assignment					
	-CH stretching (cm^{-1})		-CO at C-6 stretching (cm^{-1})		COC at β-glycosidic linkage (cm^{-1})	
	BT [a]	AT	BT	AT	BT	AT
Cotton	2901	2893	1033	1025	897	894
MCC	2900	2892	1033	1025	896	893

[a] BT and AT: before and after the $[BMIM]^+[Cl]^-$ treatment.

2.3.3 Morphology and Dimension Distribution of Regenerated Cellulose II Nanoparticles

Figure 2.3 shows the typical TEM micrographs of M-RCNs and C-RCNs. Figure. 2.3a and b shows that M-RCNs and C-RCNs present similar shape and moderate dispersibility. They were wavy, disordered and partly fused, which might be caused by the reduced crystallinity of cellulose (confirmed by WXRD patterns). Similar morphology was also observed in the regenerated cellulose II fibers by the TEMPO-mediated oxidation or alkaline treatments (Hirota et al. 2012). In addition, some curve-structured nanoparticles appeared to form thicker bundles of aggregates for M-RCNs and C-RCNs that are slightly different from the needle-like cellulose nanocrystals/whiskers produced by conventional acid hydrolysis process (Liu et al. 2010). Similar observations were reported previously, and the cellulose in aqueous suspension is known to have a general tendency to aggregate in parallel with each other (Marchessault et al. 1959). Several possible explanations for cellulose aggregation were presented previously in related studies. The negative staining was considered to induce an artificial aggregation of cellulose on the surfaces of carbon-coated copper grids, because water and uranyl acetate were evaporated and blotted up in the drying step (Elazzouzi-Hafraoui et al. 2008). Another reason for agglomeration is a surface ionic charge of the cellulose (Liu et al. 2010).

To evaluate the dimension of M-RCNs and C-RCNs based on TEM observations, the nanoparticles in aqueous suspension needs to be further dispersed by high-pressure homogenization process. Compared with M-RCNs (Figure 2.3a) and C-RCNs (Figure 2.3b) without high-pressure homogenization, some homogenized M-RCNs (Figure 2.3d) and C-RCNs (Figure 2.3c) presented a relatively uniform shape, and partial RCN aggregates were separated to a certain degree. Occasional aggregation still existed after high-pressure homogenization. This phenomenon suggested that high-pressure homogenization treatment could partly disperse the

aggregated cellulose by intense mechanical shearing forces and enhance the dispersibility of cellulose in aqueous suspension (Liu et al. 2010).

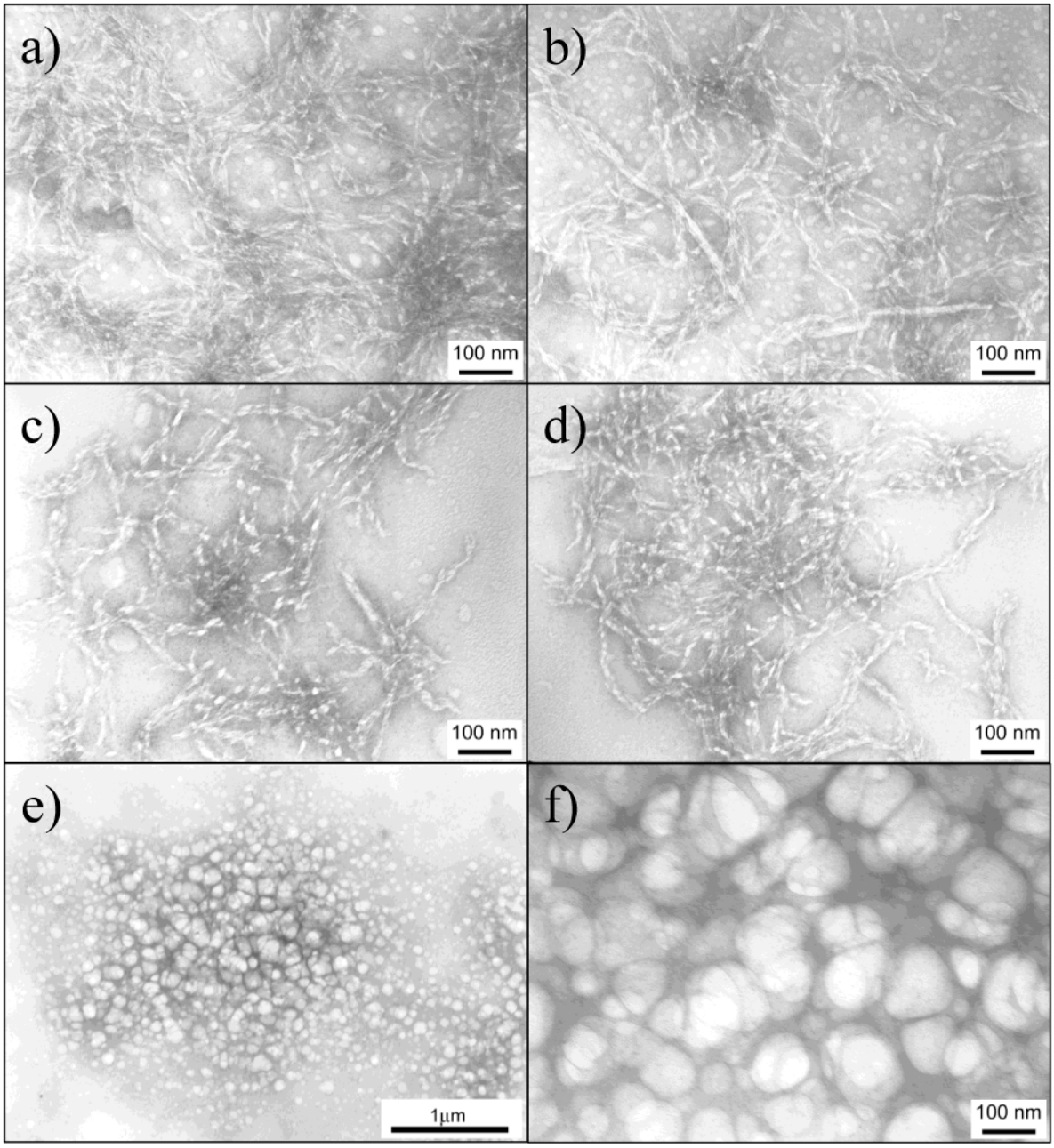

Figure 2.3 TEM images of M-RCNs (a), C-RCNs (b), homogenized M-RCNs (c), homogenized C-RCNs (d) and spherical RCNs (e, f).

Table 2.2 The dimension statistics of M-RCNs, C-RCNs and spherical RCNs (S-RCNs)

Parameters	C-RCNs		M-RCNs		S- RCNs
	Length (nm)	Width (nm)	Length (nm)	Width (nm)	Diameter (nm)
Sample size	100	100	100	100	100
Mean	123	12	112	12	118
Maximum	197	23	204	23	226
Mode (M)	125	13	113	13	107
Minimum	60	4	39	6	47
Standard deviation (S)	34	5	42	3	32
95% C.I. of Mean [a]	[116,130]	[12,13]	[103,120]	[11,13]	[112,125]
Aspect ratio [b]	9.96		9.21		NA

[a]: 95% Confidence interval;

[b]: Aspect ratio is calculated by Mean of Length divided by Mean of Width.

The dimension of homogenized M-RCNs and C-RCNs is presented in Table 2.2 and the size distribution of each sample was plotted as histogram (Figure 2.4). Because cellulose tended to agglomerate in parallel and overlap longitudinally, the accurate determination of RCN dimensions was challenging. It was believed that cellulose II had some disordered regions or defects at 100–200 nm intervals periodically present along the length direction, which was defined as the dimension of cellulose II nanoparticles (Hirota et al. 2012). Therefore, the length and width of RCNs can be measured directly from TEM images by using ImageJ 1.45k software. The width was defined as the largest dimension measured along the each nanoparticle, perpendicular to its long axis (Elazzouzi-Hafraoui et al. 2008). The statistical results of RCN dimensions are summarized in Table 2.2. For fiber-type C-RCNs, the average width and length were approximately 12 ± 5 and 123 ± 34 nm, respectively. The corresponding aspect ratio was 9.96 calculated by mean length/mean width. For fiber-type M-RCNs, the mean width and length

were approximately 12 ± 3 and 112 ± 42 nm, respectively. The dimension of RCNs was similar to that of the regenerated cellulose II nanoparticles prepared by TEMPO-mediated oxidation of mercerized cellulose (Hirota et al. 2012). The corresponding aspect ratio was 9.21, which is slightly less than the aspect ratio of C-RCNs. It was reported that these celluloses II nanoparticles regenerated from ILs had relatively better flow properties and higher bulk and tap densities, which was advantageous in tableting, especially in the manufacture of tablets with high-dose drugs (Azubuike et al. 2012).

The corresponding size distribution of M-RCNs and C-RCNs was further plotted on the histograms in Figure 2.4. All the lengths and widths showed an asymmetrical log-normal distribution (referred to as a Galton's distribution). Previous studies applied a log-normal function *Y* to fit this type of size distribution of objects obtained by fragmentation (eq. 2.3) (Elazzouzi-Hafraoui et al. 2008):

$$Y = Ke^{\frac{-(\ln M)^2 - \ln X}{S^2}} \tag{2.3}$$

where *S* is the standard deviation, *K* is the fitting coefficient, and *M* is the mode. To obtain the specific equations for each sample, the corresponding *S* and *M* values were statistically calculated using Origin 8.5 software and are summarized in Table 2.2.

In addition to the fiber-type nanoparticles, spherical regenerated cellulose II nanoparticles (Spherical RCNs) produced from MCC were also observed in TEM images (Figure 2.3e and f). Figure 2.3f with a 100 nm scale bar is an enlarged image of the central part of Figure 2.3e with a 1 μm scale bar. The average diameter was 118 ± 32 nm (Table 2.2). The approximate spherical RCNs formed irregular aggregates from their initial globular particles. Similar spherical cellulose II particles were previously observed in the 12% (w/w) NaOH treated bacterial cellulose (Shibazaki et al. 1997).

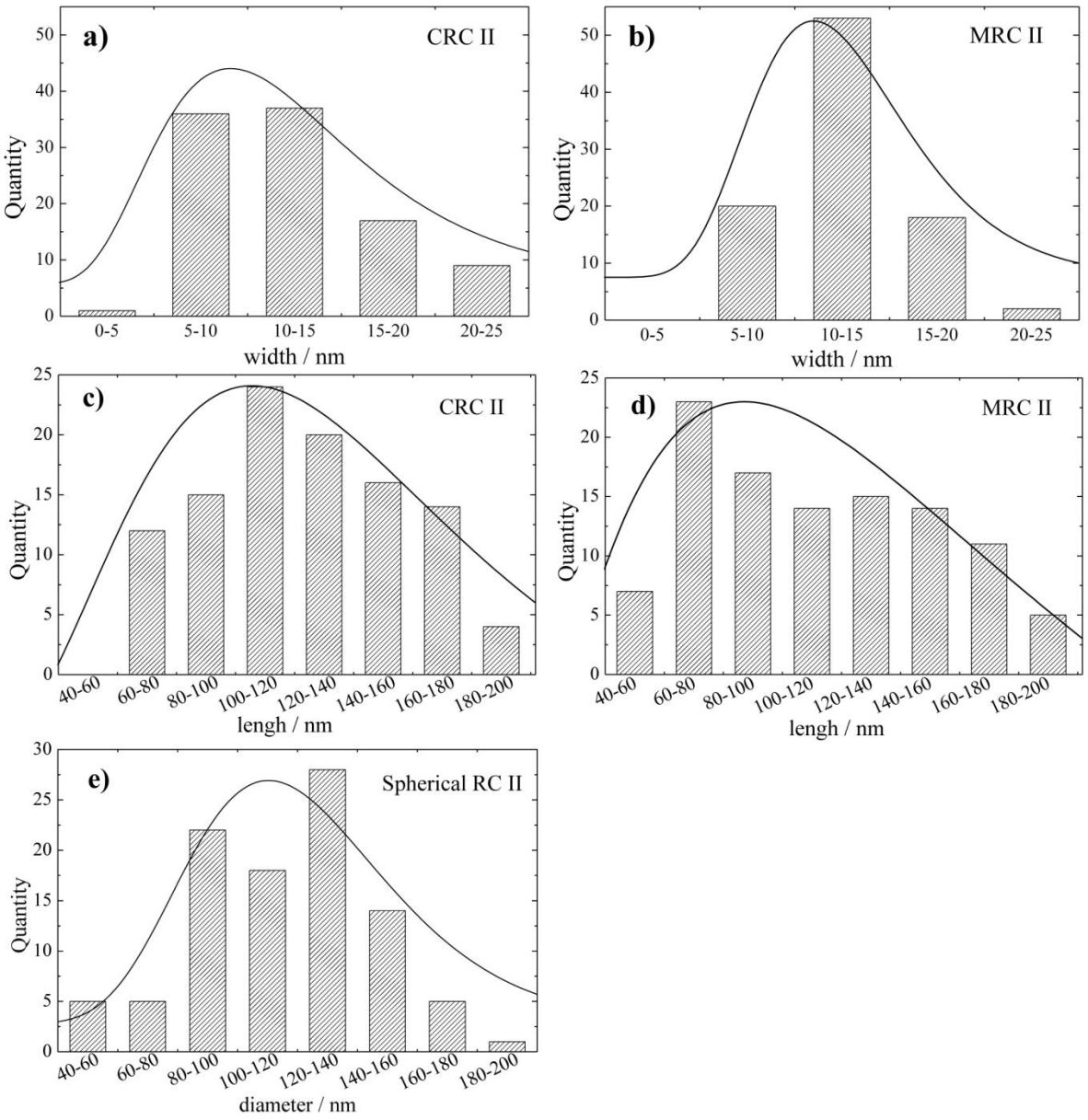

Figure 2.4 The dimension distribution of homogenized M-RCNs, C-RCNs and spherical RCNs. (a) and (b) width distribution of C-RCNs and M-RCNs; (c) and (d) length distribution of C-RCNs and M-RCNs; (e) diameter distribution of spherical RCNs.

In addition, similar spherical cellulose I that resulted from a mild acid hydrolysis concentration, or from a combination of both hydrochloric and sulfuric acids and ultrasonic treatment have also been reported. The spherical cellulose demonstrated better thermal stability than fiber-like cellulose (Lu and Hsieh 2010; Wang et al. 2007a; Wang et al. 2008; Wang et al.

2007b). Since $[BMIM]^+[Cl]^-$ can dissolve cellulose more effectively than acid solutions at certain conditions, the formation mechanism of spherical RCNs in ILs could be inferred from the perspective of reaction kinetics. For acid hydrolysis of cellulose molecules, the hydrolysis reaction started from the surface and then gradually permeated into the inner amorphous region (Wang et al. 2008). In contrast, $[BMIM]^+[Cl]^-$, with a better capability of dis- solving cellulose, the IL molecules could instantly penetrate the inner amorphous region of cellulose, leading to a simultaneous reaction both at the surface and in the inner amorphous regions of MCC. This process might cause some MCC particles to first transfer to the irregular spherical shape, instead of fiber-like cellulose nanoparticles.

2.3.4 TGA results

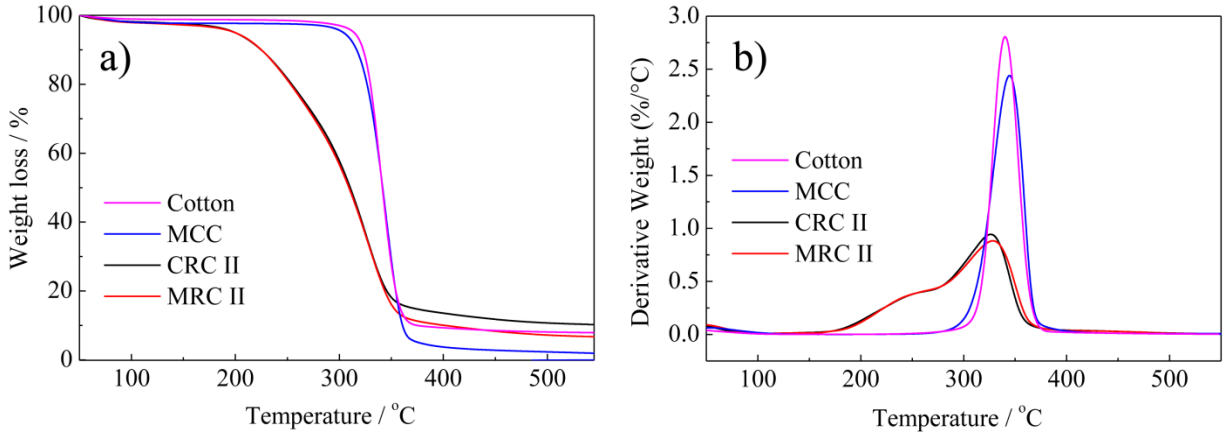

Figure 2.5 Thermo gravimetric (TG) curves (a) and derivatives of thermo gravimetric (DTG) curves (b) for untreated MCC, M-RCNs, raw cotton, and C-RCNs.

Thermogravimetric (TG) curves and derivative thermogravimetric (DTG) curves of raw cotton, untreated MCC and the corresponding freeze-dried M-RCNs and C-RCNs are shown in Figure 2.5. Table 2.3 lists extrapolated onset temperature (T_o, ℃), the maximum thermal degradation temperature (T_{max}, ℃), the maximum weight loss rate (R_{max}, %/℃) and char yields (CY, %) for various samples. All samples had a small weight loss in the low temperature (less

than 125 ℃) range, corresponding to the evaporation of absorbed water in raw materials and final RCN materials.

The original MCC showed a typical decomposition behavior with an onset degradation temperature (T_o) of 300.3 ℃, and the maximum thermal degradation temperature (T_{max}) occurred at 344.3 with the maximum weight loss rate (R_{max}) of 2.4%/ ℃ (Table 2.3). The degradation of the original MCC occurred within a relatively narrow temperature range and had only one pyrolysis process in the DTG curve. The main mass loss step of the original MCC ranged from 300.3 to 376.1 ℃. The corresponding char yield (CY) at 550 ℃ is 1.9%.

Table 2.3 Onset degradation temperature (T_o), maximum thermal degradation temperature (T_{max}), maximum weight loss rate (R_{max}), and char yield (CY) at 550 ℃ in the thermal degradation process of each sample obtained from TG and DTG curves

Sample	T_o (℃)	Stage I		Stage II		CY (wt%)
		T_{max} (℃)	R_{max} (%/℃)	T_{max} (℃)	R_{max} (%/℃)	
MCC	300.3	---	---	344.3	2.4	1.9
MRC II	205.8	254.7	0.4	328.4	0.9	6.7
Cotton	310.6	---	---	340.3	2.7	7.9
CRC II	200.8	258.7	0.4	325.8	0.9	10.3

On the other hand, the M-RCNs showed a different decomposition behavior than the original MCC (Figure 2.5a). The more gradual thermal transitions began at a relatively lower T_o of 205.8 ℃. Similar gradual thermal transitions of cellulose were reported previously (Lu and Hsieh 2010). The degradation of M-RCNs occurred within a wider temperature range and had two well-separated pyrolysis processes in the DTG curve. The first process of weight loss ranged from 205.8 ℃ to 268.2 ℃ with the T_{max} at 254.7 ℃. The second, which dominated the overall pyrolysis, ranged from 268.2 ℃ to 361.4 ℃ with the T_{max} at 328.4 ℃, having relatively higher char residue, nearly 6.7%, at 550 ℃ (Figure 2.5b). A similar two-step pyrolysis of acid-treated cellulose nanocrystals was reported previously (Wang et al. 2007a; Wang et al. 2007b).

For the original cotton (Figure 2.5a), a typical decomposition trend with an onset degradation temperature of 310.6 ℃ was observed, and this coincided with a large mass loss, resulting in 7.9% char yield (CY) at 550 ℃. The maximum thermal degradation temperature (T_{max}) occurred at 340.3 ℃ with the maximum weight loss rate (R_{max}) of 2.7%/ ℃ (Table 2.3). The degradation of the original cotton occurred within a relatively narrow temperature range and had only one pyrolysis process in the DTG curve. The main mass loss step of the original cotton ranged from 310.6 ℃ to 368.7 ℃.

Similarly, the C-RCNs also exhibited significantly different thermal behavior than the original cotton, showing more gradual thermal transitions that began at a relative lower T_o of 200.8 ℃. The degradation of C-RCNs occurred within a wider temperature range and had two well-separated pyrolysis processes in the DTG curve. The C-RCNs lost approximately 25% of the original mass in the 200.8–273.4 ℃ region followed by another 55% mass loss between 273.4 ℃ and 366.7 ℃, having a relatively higher char residue, nearly 10.3% CY, at 550 ℃. The maximum thermal degradation temperatures (T_{max}) of stage 1 and stage 2 were 258.7 ℃ and 325.8 ℃, respectively, and the corresponding CY were 0.4 and 0.9%/ ℃, respectively (Figure 2.5b).

Therefore, the untreated MCC and native cotton samples showed similar one-step pyrolysis processes, while the M-RCNs and C-RCNs had similar two-step pyrolysis processes. Thermal behavioral differences between the RCNs and the original cellulose sources may be due to different decomposition–gasification processes. T_o and T_{max} values of M-RCNs and C-RCNs were lower than the representative values for original MCC and cotton. Similar phenomenon was reported previously (Chen et al. 2012). This demonstrated that the thermal stability of cellulose decreased after regeneration from $[BMIM]^+[Cl]^-$, which was consistent with the observed

decrease of CI of cellulose dissolved in $[BMIM]^+[Cl]^-$. Although the regenerated cellulose had a lower onset temperature for decomposition, the char yield (CY) at 550 ℃ of M-RCNs and C-RCNs was greater than that of MCC or cotton (Table 2.3). The decrease in thermal stability could be due to several reasons. First, the adhesion of the anion group from the ionic liquid onto the surface of cellulose nanoparticles could have an effect on thermal behavior of cellulose (Kim et al. 2001). Second, the high surface area of cellulose nanoparticles might diminish their thermostability due to the increased exposure surface area to heat (Lu and Hsieh 2010).

2.3.5 Mechanism of the Dissolution and Regeneration

Based on the results obtained above, the possible mechanism of dissolution of cellulose in $[BMIM]^+[Cl]^-$ could be inferred as follows. Native cellulose is a semi-crystalline polymer consisting of highly crystalline and amorphous regions. The inter- and intra-molecular hydrogen bonds of cellulose chains need to be disrupted in order to dissolve cellulose (Jin et al. 2012). The previous studies on the mechanism of the cellulose dissolution in ILs showed that the interactions between the hydroxyls of cellulose and the anions of the ILs played an important role in this process. When cellulose was dissolved in $[BMIM]^+[Cl]^-$, the ion pairs in $[BMIM]^+[Cl]^-$ dissociated to individual $[BMIM]^+$ cation and $[Cl]^-$ anion (Jin et al. 2012). The hydrogen and oxygen atoms of the cellulose molecules formed electron donor-electron acceptor complexes with the charged species of the $[BMIM]^+[Cl]^-$ (Pinkert et al. 2009). On the one hand, the dissociated $[BMIM]^+[Cl]^-$ enters the space between the cellulose chains. Then free $[Cl]^-$ anions associated with the hydroxyl proton of H-O ··H bonds. Meanwhile, free $[BMIM]^+$ cations attack the oxygen atoms of H-O ··H bonds. This interaction resulted in the separation of the hydroxyl groups of the different cellulose chains leading to the swelling behavior of cellulose fibrils. On the other hand, within a single cellulose chain, $[Cl]^-$ anions attack the carbon atoms of

the β-1,4-glycosidic bonds and $[BMIM]^+$ with its electron rich aromatic π system interacted with the oxygen atom of the β-1,4-glycosidic bonds via non- bonding or π electrons. These interactions resulted in the breakage of the extensive hydrogen bonding network between two cellulose chains and the breakage of the β-1,4-glycosidic bonds within cellulose chains, which further led to the dissolution and degradation of cellulose into a molecular level (Kosan et al. 2008). It was also reported that $[Cl]^-$ anions were mainly responsible for the effective dissolution of cellulose due to the higher strength and larger interaction energy of $[Cl]^-$ anions with the oligomer.

However, the subtle structural and size changes of cellulose occurred not only in the solubilization state but also in the reconstitution stage. Rapid mixing of the cellulose/$[BMIM]^+[Cl]^-$ solution with distilled water (polar solvent) resulted in precipitation of cellulose as powdery flocs. This phenomenon indicated that the cellulose dissolved in $[BMIM]^+[Cl]^-$ could reconstitute with the presence of anti-solvent. In the regeneration process, hydrogen-bonding properties still played a key role in the reconstruction of cellulose in cellulose/water/$[BMIM]^+[Cl]^-$ system (Swatloski et al. 2002). Because the O-H ··O type H-bond is far stronger than the C-H ··O type H-bond, $[BMIM]^+[Cl]^-$ prefers to form H-bonds with water molecules (Ding et al. 2012). This is the reason why $[BMIM]^+[Cl]^-$ has a strong water absorbability. As a result, the H-bonds between cellulose and $[BMIM]^+[Cl]^-$ were weakened with addition of water into cellulose/$[BMIM]^+[Cl]^-$ system. During the regeneration process, the H-bonds between cellulose chains reconnected with each other, resulting in the reconstitution and precipitation of cellulose. However, the TGA data showed that the onset decomposition temperature for regenerated cellulose was about 100 ℃ lower than that for original cellulose. This decreased thermal stability indicated the decrease in molecular weight of regenerated

cellulose (Chen et al. 2012). In addition, WXRD results suggested that the crystallinity index of cellulose decreased for both MCC and cotton during dissolution and regeneration. The lower crystallinity of regenerated cellulose indicated that this interaction was not sufficient to completely reestablish the strong H-bond network of original microcrystalline cellulose. Therefore, the cellulose dissolved in $[BMIM]^+[Cl]^-$ could only regain a lower crystallinity and reconstitute into nano-sized particles with cellulose II crystalline allomorph upon the addition of water during regeneration. The nanoparticles could be further dispersed steadily in water through high-pressure homogenization treatment. Based on the initial weight of the cellulose in $[BMIM]^+[Cl]^-$, the yield of the reconstituted cellulose II nanoparticles was estimated to be 30–40 wt%, supporting the aforementioned hypothesis on the formation of regenerated cellulose nanoparticles. The theoretical interpretations provided assistance to develop appropriate IL-based solvents for dissolution and processing of cellulose (Xu et al. 2012).

2.4 CONCLUSIONS

In this work, regenerated cellulose II nanoparticles were successfully produced from MCC and cotton by using a combined IL and high-pressure homogenization treatment. The crystal structures of cellulose were transformed from cellulose I to II with decreased crystallinities during the ILs treatment. The fiber-type C-RCNs had an average length of 123 ± 34 nm, an average width of 12 ± 5 nm, while the fiber-type M-RCNs had an average length of 112 ± 42 nm, an average width of 12 ± 3 nm. The original samples showed similar one-step pyrolysis processes, while the M-RCNs and C-RCNs had similar two-step pyrolysis processes. The dimension distribution of cellulose II nanoparticles regenerated from $[BMIM]^+[Cl]^-$ followed the asymmetrical log-normal distribution. The properties of RCNs characterized in this

study provided some fundamental information for the potential application of RCNs in biomedicine field such as tablet excipients.

2.5 REFERENCES

Azubuike C. P., Rodriguez H., Okhamafe A. O. and Rogers R. D. 2012. Physicochemical properties of maize cob cellulose powders reconstituted from ionic liquid solution. *Cellulose* 19:425-433.

Chen H. Z., Wang N. and Liu L. Y. 2012. Regenerated cellulose membrane prepared with ionic liquid 1-butyl-3-methylimidazolium chloride as solvent using wheat straw. *Journal of Chemical Technology and Biotechnology* 87:1634-1640.

Ding Z. D., Chi Z., Gu W. X., Gu S. M., Liu J. H. and Wang H. J. 2012. Theoretical and experimental investigation on dissolution and regeneration of cellulose in ionic liquid. *Carbohydrate Polymers* 89:7-16.

Elazzouzi-Hafraoui S., Nishiyama Y., Putaux J. L., Heux L., Dubreuil F. and Rochas C. 2008. The shape and size distribution of crystalline nanoparticles prepared by acid hydrolysis of native cellulose. *Biomacromolecules* 9:57-65.

Gao Q. Y., Shen X. Y. and Lu X. K. 2011. Regenerated bacterial cellulose fibers prepared by the NMMO center dot H2O process. *Carbohydrate Polymers* 83:1253-1256.

Gutowski K. E., Broker G. A., Willauer H. D., Huddleston J. G., Swatloski R. P., Holbrey J. D. and Rogers R. D. 2003. Controlling the Aqueous Miscibility of Ionic Liquids: Aqueous Biphasic Systems of Water-Miscible Ionic Liquids and Water-Structuring Salts for Recycle, Metathesis, and Separations. *Journal of the American Chemical Society* 125:6632-6633.

Hirota M., Tamura N., Saito T. and Isogai A. 2012. Cellulose II nanoelements prepared from fully mercerized, partially mercerized and regenerated celluloses by 4-acetamido-TEMPO/NaClO/NaClO2 oxidation. *Cellulose* 19:435-442.

Jiang G. S., Huang W. F., Li L., Wang X., Pang F. J., Zhang Y. M. and Wang H. P. 2012. Structure and properties of regenerated cellulose fibers from different technology processes. *Carbohydrate Polymers* 87:2012-2018.

Jin Z. W., Wang S., Wang J. Q. and Zhao M. X. 2012. Effects of plasticization conditions on the structures and properties of cellulose packaging films from ionic liquid [BMIM]Cl. *Journal of Applied Polymer Science* 125:704-709.

Kim D. Y., Nishiyama Y., Wada M. and Kuga S. 2001. High-yield carbonization of cellulose by sulfuric acid impregnation. *Cellulose* 8:29-33.

Kosan B., Michels C. and Meister F. 2008. Dissolution and forming of cellulose with ionic liquids. *Cellulose* 15:59-66.

Kumar R., Mago G., Balan V. and Wyman C. E. 2009. Physical and chemical characterizations of corn stover and poplar solids resulting from leading pretreatment technologies. *Bioresource Technology* 100:3948-3962.

Kumar V., de la Luz Reus-Medina M. and Yang D. 2002. Preparation, characterization, and tabletting properties of a new cellulose-based pharmaceutical aid (vol 235, pg 129, 2002). *International Journal of Pharmaceutics* 248:261-261.

Kuo C. H. and Lee C. K. 2009. Enhancement of enzymatic saccharification of cellulose by cellulose dissolution pretreatments. *Carbohydrate Polymers* 77:41-46.

Lan W., Liu C. F., Yue F. X., Sun R. C. and Kennedy J. F. 2011. Ultrasound-assisted dissolution of cellulose in ionic liquid. *Carbohydrate Polymers* 86:672-677.

Lee S. H., Doherty T. V., Linhardt R. J. and Dordick J. S. 2009. Ionic Liquid-Mediated Selective Extraction of Lignin From Wood Leading to Enhanced Enzymatic Cellulose Hydrolysis. *Biotechnology and Bioengineering* 102:1368-1376.

Li C. L., Knierim B., Manisseri C., Arora R., Scheller H. V., Auer M., Vogel K. P., Simmons B. A. and Singh S. 2010. Comparison of dilute acid and ionic liquid pretreatment of switchgrass: Biomass recalcitrance, delignification and enzymatic saccharification. *Bioresource Technology* 101:4900-4906.

Li Q., He Y. C., Xian M., Jun G., Xu X., Yang J. M. and Li L. Z. 2009. Improving enzymatic hydrolysis of wheat straw using ionic liquid 1-ethyl-3-methyl imidazolium diethyl phosphate pretreatment. *Bioresource Technology* 100:3570-3575.

Liu H. Y., Liu D. G., Yao F. and Wu Q. L. 2010. Fabrication and properties of transparent polymethylmethacrylate/cellulose nanocrystals composites. *Bioresource Technology* 101:5685-5692.

Lu P. and Hsieh Y. L. 2010. Preparation and properties of cellulose nanocrystals: Rods, spheres, and network. *Carbohydrate Polymers* 82:329-336.

Mahmoudian S., Wahit M. U., Ismail A. F. and Yussuf A. A. 2012. Preparation of regenerated cellulose/montmorillonite nanocomposite films via ionic liquids. *Carbohydrate Polymers* 88:1251-1257.

Mansikkamaki P., Lahtinen M. and Rissanen K. 2007. The conversion from cellulose I to cellulose II in NaOH mercerization performed in alcohol-water systems: An X-ray powder diffraction study. *Carbohydrate Polymers* 68:35-43.

Marchessault R. H., Morehead F. F. and Walter N. M. 1959. Liquid Crystal Systems from Fibrillar Polysaccharides. *Nature* 184:632-633.

Pinkert A., Marsh K. N., Pang S. S. and Staiger M. P. 2009. Ionic Liquids and Their Interaction with Cellulose. *Chemical Reviews* 109:6712-6728.

Quan S. L., Kang S. G. and Chin I. J. 2010. Characterization of cellulose fibers electrospun using ionic liquid. *Cellulose* 17:223-230.

Ray D. and Sarkar B. K. 2001. Characterization of alkali-treated jute fibers for physical and mechanical properties. *Journal of Applied Polymer Science* 80:1013-1020.

Shibazaki H., Kuga S. and Okano T. 1997. Mercerization and acid hydrolysis of bacterial cellulose. *Cellulose* 4:75-87.

Swatloski R. P., Spear S. K., Holbrey J. D. and Rogers R. D. 2002. Dissolution of cellose with ionic liquids. *Journal of the American Chemical Society* 124:4974-4975.

Tamai N., Tatsumi D. and Matsumoto T. 2004. Rheological properties and molecular structure of tunicate cellulose in LiCl/1,3-dimethyl-2-imidazolidinone. *Biomacromolecules* 5:422-432.

Wang L. L., Han G. T. and Zhang Y. M. 2007a. Comparative study of composition, structure and properties of Apocynum venetum fibers under different pretreatments. *Carbohydrate Polymers* 69:391-397.

Wang N., Ding E. Y. and Cheng R. S. 2007b. Thermal degradation behaviors of spherical cellulose nanocrystals with sulfate groups. *Polymer* 48:3486-3493.

Wang N., Ding E. and Cheng R. S. 2008. Preparation and 'liquid crystalline properties of spherical cellulose nanocrystals. *Langmuir* 24:5-8.

Xu H., Pan W. X., Wang R. X., Zhang D. J. and Liu C. B. 2012. Understanding the mechanism of cellulose dissolution in 1-butyl-3-methylimidazolium chloride ionic liquid via quantum chemistry calculations and molecular dynamics simulations. *Journal of Computer-Aided Molecular Design* 26:329-337.

Yue Y. Y., Zhou C. J., French A. D., Xia G., Han G. P., Wang Q. W. and Wu Q. L. 2012. Comparative properties of cellulose nano-crystals from native and mercerized cotton fibers. *Cellulose* 19:1173-1187.

Zhang H., Wang Z. G., Zhang Z. N., Wu J., Zhang J. and He H. S. 2007. Regenerated-cellulose/multiwalled-carbon-nanotube composite fibers with enhanced mechanical properties prepared with the ionic liquid 1-allyl-3-methylimidazolium chloride. *Advanced Materials* 19:698-+.

Zhang X. M., Liu X. Q., Zheng W. G. and Zhu J. 2012. Regenerated cellulose/graphene nanocomposite films prepared in DMAC/LiCl solution. *Carbohydrate Polymers* 88:26-30.

Zhao H. B., Kwak J. H., Wang Y., Franz J. A., White J. M. and Holladay J. E. 2007. Interactions between cellulose and N-methylmorpholine-N-oxide. *Carbohydrate Polymers* 67:97-103.

Zhu S. D., Wu Y. X., Chen Q. M., Yu Z. N., Wang C. W., Jin S. W., Ding Y. G. and Wu G. 2006. Dissolution of cellulose with ionic liquids and its application: a mini-review. *Green Chemistry* 8:325-327.

CHAPTER 3 SELF-ASSEMBLING BEHAVIOR OF CELLULOSE NANOPARTICLES DURING FREEZE DRYING: EFFECT OF SUSPENSION CONCENTRATION, PARTICLE SIZE, CRYSTAL STRUCTURE, AND SURFACE CHARGE[2]

3.1 INTRODUCTION

Foam biomaterials with well-defined structures are desirable for a wide range of applications, including drug delivery, tissue engineering, green packaging and automotive components (Lee and Deng 2011). They have high strength-to-weight ratios and porosities to carry and/or store other materials to form composites. By controlling their microstructures, the properties of the materials can be readily tuned. Among the available techniques, freeze-drying has been shown as a novel, low-cost, simple and versatile route for the preparation of foam biomaterials with controlled structures (Dash et al. 2012). During the freezing process of an aqueous suspension, suspended particles are organized in the intervening space between growing ice crystal fronts, leading to an ordered structure after sublimation of ice crystal templates.

Cellulose nanocrystals (CNCs) and cellulose nanofibers (CNFs) have recently received a considerable amount of attention due to their intrinsically appealing properties (Habibi et al. 2010). The rod-like CNCs and needle-like CNFs are mainly prepared by controlled acid hydrolysis of native cellulose sources. For wood, mean width and length of CNCs are 5 to 10 nm and 100 to 300 nm, respectively, and the CNFs are 5 to 50 nm in width and several micrometers in length (Beck-Candanedo et al. 2005; Bondeson et al. 2006). In order to expand their applications, much work has concentrated on the drying process of CNC and CNF aqueous suspensions (Peng et al. 2012).

[2] Reprint in part with permission from Biomacromolecules
Han J. Q., Zhou C. J., Wu Y. Q., Liu F. Y., Wu Q. L. 2013. Self-Assembling Behavior of Cellulose Nanoparticles during Freeze-Drying: Effect of Suspension Concentration, Particle Size, Crystal Structure, and Surface Charge. *Biomacromolecules* 14:1529-40.

Recently, research has been attempted to use the freeze-drying technique to fabricate biomimetic cellulose foam with different microstructures and properties (Svagan et al. 2008). Lee and Deng (Lee and Deng 2011) prepared cellulose microfibril foams with a lamellar channel or a cross-linked network structure using a directional freezing technique. They investigated the effect of freezing temperature and suspension concentrations on the microstructure and mechanical properties of cellulose microfibril foams. Subsequently, Dash et al. (Dash et al. 2012) fabricated cellulose nanowhisker foams with a uniform layer structure, and they discussed the relationship between the freezing conditions and the microstructures obtained. However, some fundamental research still needs to be conducted in order to understand the self-organization of cellulose particles during the freeze-drying process. The lyophilization process consists of two important steps, i.e., growing of the ice crystals (freezing) and sublimation of the ice molecules (drying). Upon freezing cellulose aqueous suspensions, water is frozen into ice crystals and then most cellulose particles above the critical particle size are trapped by the moving water-ice front and confined into the interstitial spaces between ice crystals. The final structure of cellulose foam is formed as ice crystals are sublimated during the drying step (Deville and Nalla 2006; Svagan et al. 2008). Therefore, in addition to the freezing conditions, the particle size, surface charge, suspension concentration, and their relationship with the self-assembly behavior of cellulose particles are theoretically related to the morphology and properties of the final foam. Lee and Deng (Lee and Deng 2011) reported the effects of high concentrations (above 1.0 wt%) on the microstructure and mechanical properties of cellulose microfibril foams. However, little is known about the self-assembling behavior of cellulose particles during the freeze-drying process at low suspension concentrations (e.g., below 1.0 wt%).

In the present study, size-controllable cellulose particles with cellulose I and II structures were extracted from bleached wood pulp (BWP) using alkali treatment and/or acid hydrolysis in combination with homogenization process. The crystal structure, crystallinity, hydrogen bonding patterns, surface charge, and morphology of cellulose particles produced using different methods were compared. The dispersion state, liquid-crystalline properties and optical transmittance of cellulose aqueous suspensions were also studied. The objectives of the work were to investigate the effects of suspension concentrations (0.05 to 1.0 wt%), particle size, crystal structure, and surface charge on the self-assembling behavior of cellulose particles during the freeze-drying process. This research described the liquid-crystalline properties, supramolecular structure development, and self-assembling mechanism of cellulose particles during lyophilization, providing a fundamental guidance for the applications of cellulose nanoparticles as templates for layered scaffolds, filters, and storage materials (Dash et al. 2012; Deville and Nalla 2006).

3.2 EXPERIMENTAL

3.2.1 Materials

Bleached wood pulp, W-50 grade of KC Flock, provided by Nippon Paper Chemicals Co., LTD (Tokyo, Japan) was dried overnight in a vacuum oven at 60 ℃ before use. Sulfuric acid (95–98 wt%, VMR, West Chester, PA, USA) was of analytical grade and was diluted to a concentration of 64 wt% and 48 wt% before use. Sodium hydroxide (NaOH over 97.0% purity, ACS, MS, USA) was dissolved in distilled water to prepare a 20wt% aqueous solution. All reagents and solvents used were of analytical grade.

3.2.2 Preparation of CNCs and CNFs with cellulose I and II structures

Approximately 30 g of BWP were pretreated by an excess of 20 wt% aqueous NaOH solution for 4 h at room temperature. The obtained slurry was filtered and thoroughly washed

with distilled water until a neutral pH was reached. The pretreated wood fibers (designated as mercerized wood pulp) were then dried at 40 ℃ in a vacuum oven for 48 hours prior to further processing. For the CNCs with cellulose I structure (designated as CNC I), dry BWP was hydrolyzed using 64 wt% sulfuric acid at a fiber-to-acid ratio of 1 to 20. The mixture was stirred vigorously at 45 ℃ for 1 h and the acid hydrolysis was immediately quenched by diluting 15-folds with cold water. The diluted solution was filtered through a piece of filter paper (Grade-5, Whatman) under vacuum. The obtained wet cream-like off-white slurry material was then re-dispersed in distilled water and the mixture was stirred for 20 minutes. To further remove the residual acid, they were centrifuged at 26 ℃ for 20 min with a constant speed of 12,000 rpm (Sorvall RC-5B Refrigerated Superspeed Centrifuge, Du Pont Instrument, NH, USA). The CNCs were separated from the suspension by centrifuging after each washing. After three centrifugation cycles, the ivory-colored CNC precipitate obtained was placed in regenerated cellulose dialysis tubes with a molecular weight cut-off of 12,000 to 14,000 (Fisher Scientific, Pittsburgh, PA, USA) and dialyzed against distilled water for several days until neutral pH was reached. The resultant concentration of CNC suspension was about 0.85 wt%. For the preparation of CNFs with cellulose I structure (designated as CNF I), 48 wt% sulfuric acid was used and the other conditions were identical with those for CNC I. For the preparation of CNCs and CNFs with cellulose II structure (designated as CNC II and CNF II), 64 wt% and 48 wt% sulfuric acid were used to hydrolyze the mercerized wood pulp, respectively. All other processing conditions were the same as those used for cellulose I material.

3.2.3 High-pressure Homogenization (HPH) process

To further enhance the dispersity of obtained cellulose nanoparticles in water, mechanical homogenization was applied to the obtained aqueous suspensions. They were processed through

a high-pressure homogenizer (Microfluidizer M-110P, Microfluidics Corp., Newton, MA, USA) equipped with a pair of Z-shaped interaction chambers (one 200 μm ceramic, and one 87 μm diamond) under an operating pressure of 207 MPa. The CNC and CNF suspensions passed through the interaction chamber at a rate of 135 mL/min for five passes. The final fifth pass CNC and CNF suspensions without visible aggregation presented a pale bluish-purple color, indicating an excellent dispersity of CNCs and CNFs in aqueous suspensions. The concentration of homogenized CNC and CNF suspensions was 0.7 wt%. The concentration of each homogenized suspension was adjusted to the target levels by adding or evaporating water from the original suspensions. For the preparation of suspensions with higher concentrations, suspensions at lower concentrations were evaporated under vacuum at 65 ℃ with a rotational speed of 30 rpm in a rotary evaporator (RE300, Yamato Scientific America Inc., Santa Clara, CA, USA). The processing time was about 20-40 min, depending on the initial and desired concentrations. The concentration of each suspension was determined gravimetrically through weighing 3g of each suspension before and after the evaporation of water in air (heating for 25 min in an oven at 100 ℃). The final CNC and CNF suspensions were sealed in glass containers and stored at 5 ℃ in a refrigerator. The total yield of homogenized CNCs and CNFs (both I and II) was approximately 35% (based on the initial BWP weight), which was close to the values reported in the literature (Bondeson et al. 2006; Lu and Hsieh 2012).

3.2.4 Lyophilization

The obtained CNC (I, II) aqueous suspensions and SCNF (I, II) colloidal suspensions were freeze-dried at four dilute concentration levels (i.e., 0.05, 0.1, 0.5, and 1.0 wt%) to investigate the detailed morphology development and self-assembling mechanism of CNCs and CNFs during lyophilization. The corresponding volume concentrations were, respectively, 0.03,

0.07, 0.34, and 0.67 vol% based on a cellulose density of 1.5 g/cm^3 (Boluk et al. 2012). Approximately 200 mL of each suspension at a certain concentration level was poured into a 300 mL fast-freeze-drying flask (FreeZone, Labconco Corp., Kansas, MO, USA) and then was quickly frozen in a ultra-low-temperature freezer at -75 ℃ for about 2 hours. After being completely frozen, the samples were immediately transferred to a freeze-dryer (FreeZone plus 2.5 L, Labconco Corp., Kansas, MO, USA) and freeze-dried at a sublimating temperature of -88 ℃ under vacuum for three days to sublimate the solvent water directly from solid phase to gas phase. The final freeze-dried samples were sealed in plastic bags before performing further characterizations.

3.2.5 Fourier Transform Infrared Spectrometry (FTIR)

FTIR spectra of raw BWP, CNC I, CNF I, CNC II and CNF II were measured using a Bruker FTIR analyzer (Tensor-27, Bruker Optics Inc., Billerica, MA). All spectra were obtained in a transmittance mode on a Zn/Se ATR crystal cell at room temperature. For each measurement, approximately 5 mg of the freeze-dried powder samples were pressed into the sample chamber of the FTIR equipment, and 64 scans were taken with a resolution of 4 cm^{-1} and a spectral range of 4000-600 cm^{-1}. Three replicated measurements were recorded for each condition.

3.2.6 Wide-angle X-ray Diffraction (WXRD)

WXRD patterns of the untreated BWP, CNC I, CNF I, CNC II, and CNF II were measured using a Bruker/Siemens D5000X-ray automated powder X-ray diffractometer. Before testing, each freeze-dried sample was dried again in a vacuum oven at 60 ℃ for 24 h to remove moisture. The WXRD data were generated by a diffractometer with Cu-Ka radiation (λ = 1.542Å) at 40 kV and 30 mA over the angular range 2θ = 5 ºto 40 º, a step size of 0.02 degree, and a step time of 2.0 s, (1.0 h per scan). The data were further analyzed using the MDI Jade 6.5.26

software (Serial No.: MDI-R99691, Materials Data Inc., Livermore, California). For each sample, the background was fitted with a software-generated cubic-spline function. Subsequently, the whole pattern was smoothed by a parabolic filter to reduce excess noise.

The degree of crystallinity or crystallinity index (CI, %) for each sample was determined using eq. (3.1) (Segal et al. 1959)

$$CI(\%) = 100\frac{I_{Max} - I_{Am}}{I_{Max}} \tag{3.1}$$

where, I_{Max} is the maximum intensity of the principal peak, and I_{Am} is the intensity of diffraction attributed to amorphous cellulose. The *CI* values were calculated based on the original data without fitting background.

3.2.7 Transmission Electron Microscopy (TEM)

For the TEM analysis, concentrations of the aqueous suspensions were diluted to 0.05 to 0.1 wt%. The diluted suspensions were treated with an ultrasonic bath (Model 3510, Branson, MS) prior to the TEM operation. A droplet (5 μL) of diluted suspension was negatively stained with a droplet (5 μL) of 2 wt% uranyl acetate for about 2 min to enhance the contrast of TEM images. Then the mixture was immediately deposited on the surface of a 400-mesh carbon-coated copper grid. The excess liquid on the grid was absorbed by using a tiny piece of filter paper to touch the edge of the grid. The morphology of obtained CNCs and CNFs (I and II) was characterized by using Transmission Electron Microscope (JEOL 100CX, JEOL, Inc., Peabody, MA) with an accelerating voltage of 80 kV. The particle dimension was calculated with TEM images using ImageJ 1.45k software (Rasband, W.S., ImageJ, U. S. National Institutes of Health, Bethesda, MD, http://imagej.nih.gov/ij/, 1997-2011). For each sample, one hundred particles were randomly selected and measured from several TEM images. The width was defined as the

largest dimension measured along each particle, perpendicular to its long axis (Elazzouzi-Hafraoui et al. 2008). Statistical parameters of particle size were calculated using the Origin 8.5.0 software (SR1 b161, OriginLab Corp., Northampton, MA).

3.2.8 Polarized Optical Microscopy (POM) Observations

The 1.0 wt% sample suspensions were transferred into a paired slide glass cell with a 0.5-mm thick spacer and observed using an Olympus BH-2 polarization optical microscope (Olympus Optical Co., LTD, Tokyo, Japan) equipped with a 530-nm retardation plate at room temperature. Each sample was allowed to stand overnight at 30℃ to achieve the slow evaporation of water on the sample edge. The texture of the liquid crystal phase was examined between a pair of crossed polarizers and the pictures were taken with a digital camera.

3.2.9 Optical Transmittance

The CNC and CNF (I and II) aqueous suspensions with concentration 0.05 to 1.0 wt% were introduced into a UV quartz cuvette with PTFE cover (dimension of 45×12.5×12.5-mm, and layer thickness of 10 mm). The optical transmittance of each aqueous suspension was measured at wavelength from 300 to 800 nm using a UV-Vis spectrophotometer (Evolution 600 PC, Thermo Electron Corp., USA). The data was collected at a scan speed of 240 nm/min and a band width of 2 nm. The transmission spectra were measured using distilled water as a reference to correct the transmittance of the dispersions. All tests were carried out at room temperature. The mean transmittance of each sample was calculated by averaging the transmittances over the wavelength ranging from 300 to 800 nm.

3.2.10 Field Emission Scanning Electron Microscopy (FE-SEM)

Prior to the FE-SEM observation, all freeze-dried samples were vacuum dried at 40℃ for 48 h. The morphology of the freeze-dried samples was examined by a FE-SEM (FEI QuantaTM

3D FEG Dual Beam SEM/FIB, Hillsboro, Oregon, USA) at an accelerating voltage of 5.0 kV. Before images were acquired, samples were mounted on SEM aluminum stubs with conductive carbon tape and sputter-coated with gold under vacuum at 20 mA for 2 min. The particle dimension was obtained from the analysis of FE-SEM images using ImageJ 1.45k software (Rasband, W.S., ImageJ, U. S. National Institutes of Health, Bethesda, MD, http://imagej.nih.gov/ij/, 1997-2011). For each sample, one hundred particles were randomly selected and measured from several FE-SEM images. The statistical analysis was performed using Origin 8.5.0 software (SR1 b161, OriginLab Corp., Northampton, MA).

3.2.11 Surface Charge Measurements

The zeta potential values (ζ, mV) of CNC I, CNC II, CNF I, and CNF II in aqueous suspensions were determined by a ZetaTrac analyzer (MicroTrac Inc., Largo, FL, USA) based on the principles of dynamic light scatting. A 3 mW laser source with 780-nm wave length was used as light source. Each sample suspension (0.05 wt%) was measured three times at 25 ℃ and pH of 7.0. The particular concentration of 0.05 wt% was within the proper range where the electric double layers on the cellulose particles barely overlap with each other (Uetani and Yano 2012). To further determine the surface charge of dried samples, X-ray photoelectron spectroscopy (XPS) was performed on the freeze-dried samples using a Specs PHOIBOS-100 spectrometer (SPECS, Berlin, Germany) with a Al Ka irradiation (1486.61 eV) at 10 kV and 10 mA. Each sample was mounted onto a holder with a piece of double-sided conductive tape and then placed in a vacuum in the range of 1 to $5x10^{-9}$ torr. Samples were analyzed at a take-off angle of 85 ° with respect to their surfaces. Survey scans were recorded with 1.0 eV step and 40 eV analyzer pass energy, while high-resolution spectrum of Na 1s and S 2p were recorded with 0.1 eV step and 40 eV analyzer pass energy. The Specslab 2.25 software was used to subtract the noise from

XPS spectra to smooth the data. No degradation of the specimens during the XPS analyses was detected. The atomic ratio of sulphur to oxygen (*S*/*O*) was calculated from corresponding peak area based on the following equation (eq. 3.2):

$$S/O = (A_O / A_C) \times (S_S / S_O) \quad (3.2)$$

where A_O and A_C are the integrated peak areas for oxygen and sulfur, respectively. S_S (0.54) and S_O (0.66) are the corrected sensitivity factors.

3.3 RESULTS AND DISCUSSION

3.3.1 Cellulose Structure and Hydrogen Bonding by FTIR

The FTIR spectra of BWP, CNC I, CNF I, CNC II and CNF II are shown in Figure 3.1. The broad band of stretching vibrations of CH and OH groups within 3650-3000 cm^{-1} region was observed in all spectra, showing the principal functional groups found in lignocellulosic materials (Kamphunthong et al. 2012; Zuluaga et al. 2009). The intense peak around 1643 cm^{-1} in all spectra corresponds to the O-H bending of adsorbed water (Johar et al. 2012). Although the FTIR samples were dried, the water adsorbed in the cellulose molecules was difficult to be removed completely due to the cellulose-water interaction (Moran et al. 2008).

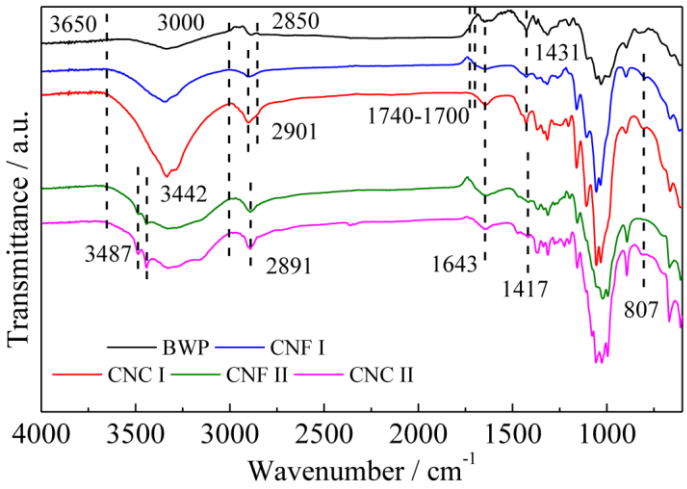

Figure 3.1 FTIR spectra of BWP, CNC I, CNF II, CNC II and CNF II.

The absorbance band within 1740-1700 cm^{-1} is attributed to the C=O stretching of methyl ester and carboxylate groups in pectin, the acetyl and uronic ester groups of the hemicelluloses or to the ester linkage of carboxylic group of the ferulic and p-coumaric acids of lignin and/or hemicelluloses (Ouajai and Shanks 2005; Wang et al. 2007). In addition, lignin presented the characteristic peak at 2850 cm^{-1} originating from C-H stretching vibration, the peak at 830 cm^{-1} attributed to an aromatic C-H out-of-plane vibration and absorbance band in the range 1500-1600 cm^{-1} corresponding to the aromatic skeletal vibration (Ouajai and Shanks 2005; Zuluaga et al. 2009). However, for the BWP, the absence of these signals in the spectra clearly verified the complete absence of lignin, pectin and hemicellulose. Therefore, the BWP used in this study was confirmed to contain only cellulose. After sulfuric acid hydrolysis, no significant differences were observed in the spectrum of CNC I and CNF I compared with that of BWP, indicating that the cellulose molecular structure was not changed in the case of acid hydrolysis (Johar et al. 2012; Li et al. 2009).

After BWP was subjected to the 20 wt% NaOH treatment, the spectra of CNC II and CNF II were different from those of BWP, CNC I and CNF I. As shown in Figure 3.1, compared with CNC I and CNF I, the spectra of CNC II and CNF II presented the two small bands at 3487 and 3442 cm^{-1} that were assigned to the intra-molecular hydrogen bonding in cellulose II (Sao et al. 1987). The maximum absorbance of CH stretching vibrations in methyl and methylene was also shifted from 2901 cm^{-1} to 2890 cm^{-1}, influenced by the transformation related to the change of intra- and intermolecular bonds (Oh et al. 2005). The absorbance peaks at 2894 cm^{-1} became sharper for CNC II and SCNF II, showing a cellulose II crystal structure (Gwon et al. 2010). The band at 1431 cm^{-1} assigned as symmetric CH_2 bending was weakened and shifted to a lower wave number 1419 cm^{-1}, indicating development of new inter- and intra-molecular hydrogen

bonds and a change of the conformation of CH_2OH at C-6 from the *tg* to the *gt* form (Oh et al. 2005). The bands at 1319 cm^{-1} assigned as CH_2 wagging, 1203 cm^{-1} attributed to C-OH in plane at C-6 bending, 1161 cm^{-1} corresponding to C-O-C asymmetric stretching at β-glucosidic linkage, 1031 cm^{-1} ascribed to C-O at C-6 stretching, 983 cm^{-1} arisen from C-O stretching at C_6 and 897 cm^{-1} assigned as C-O-C asymmetric stretching were shifted to 1313, 1197, 1157, 1022, 993 and 894 cm^{-1}, respectively, indicating the transition from cellulose I to II (Gwon et al. 2010; Oh et al. 2005). In addition, the appearance of the peak at 1227 cm^{-1} assigned as C-OH bending in plane at C_6, the disappearance of the band at 1105 assigned as ring stretching in plane, the increasing intensity of the band near 894 cm^{-1} assigned as C-O-C asymmetric stretching at the β-(1-4)-glycosidic linkage and 668 cm^{-1} assigned as COH out of plane bending were also representative indexes of the conversion into cellulose II (Dinand et al. 2002; Gwon et al. 2010; Oh et al. 2005).

Cellulose particles prepared with sulfuric acid had negatively charged surfaces due to the esterification of hydroxyl groups by sulfate ions. CNC I and CNF I both present the symmetrical C-O-S vibration at 807 cm^{-1} associated with the C-O-SO_3 group (Wang et al. 2009). However, the sulfate content of CNC II and CNF II was too low to be detected by FTIR. It was thus inferred that CNC I and CNF I carried more sulfate groups on their surfaces, which was further determined by zeta potential (Table 3.1) and XPS experiments (Figure 3.6d).

The hydrogen bonding patterns of cellulose I and II are known to be different. Therefore, the number of hydrogen bonding sites changes during the transition of crystal structure. The IR index (i.e., a ratio of IR intensity at a given wavenumber to that at the reference wavenumber) values based on the absorbance peaks at 894 cm^{-1} was used to analyze the conformation and hydroxyl intensity changes from cellulose I to II during alkaline treatment (Yue et al. 2012). It was calculated that the OH stretching vibration within the region 3,100 to 3,800 cm^{-1} of cellulose

II was higher than that of cellulose I. For example, the IR index values for CNC I and CNC II at 3,338 cm^{-1} are 0.851, and 1.030, respectively. The increased IR index values indicated that the resulting CNC II had more -OH groups on the crystal surface, which promoted the occurrence of hydrogen bonding.

3.3.2 Cellulose Structure and Crystallinity Index by WXRD

The X-ray diffractograms of BWP, CNC I and CNC II are shown in Figure 3.2a. The WXRD spectra of BWP and CNC I were nearly identical, indicating that the crystalline structure of native cellulose was maintained during the acid hydrolysis. Both X-ray diffraction diagrams of BWP and CNC I exhibited a sharp high peak at 2θ=22.6 ºand two overlapped weaker diffraction peaks at 2θ =15.1 ºand 16.6 º, assigned to (002), (101) and ($10\bar{1}$) planes, respectively, indicating the crystallographic form of cellulose I (Liu and Hu 2008). Compared with BWP, the peak for the (101) plane (2θ = 15.1 º) became more intense and separated from the ($10\bar{1}$) (2θ = 16.6 º) peak for CNC I, as reported previously (Lu and Hsieh 2010).

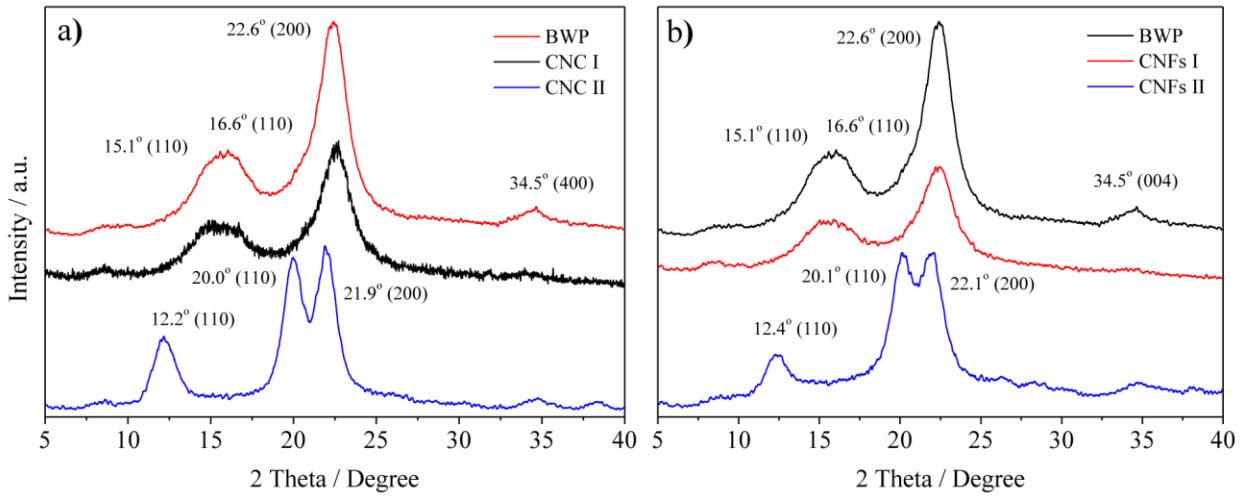

Figure 3.2 X-ray diffraction patterns of BWP, CNC I and CNC II (a); CNF I and CNF II (b)

Upon the pretreatment of BWP in the 20 wt% NaOH solution, the peaks at 2θ = 15.1 ° and 2θ = 16.6 ° disappeared and a new peak at 2θ = 12.2 ° (1$\underline{1}$0) formed. The (200) peak at 2θ = 22.6 ° was split into two weaker peaks located at 2θ = 20.0° (110) and 2θ = 21.9° (200) with similar intensities, suggesting the transformation of crystalline structure from cellulose I to cellulose II (Mahadeva and Kim 2009; Zuluaga et al. 2009). The rearrangement in intermolecular hydrogen bond and agglomeration between the chains during mercerization process led to the polymorphic transformation from 'parallel' chains in cellulose I to 'antiparallel' chains in cellulose II (Yue et al. 2012).

The X-ray diffraction patterns of CNF I and CNF II are shown in Figure 3.2b. Three cellulose I peaks at 2θ = 15.1 ° (101), 16.6 ° (10$\underline{1}$) and 22.6 ° (002) were present in CNF I. After the mercerization, the pattern of CNF II exhibited the peaks located at 2θ = 12.4 ° (1$\underline{1}$0), 20.1 ° (110), and 22.1 ° (200), respectively, indicating the conversion of cellulose I into a weaker cellulose II crystal structure. The mercerization of cellulose fibers has three distinct steps: fiber swelling, disruption of the crystalline areas and formation of new crystalline lattice after rinsing away alkali solution. When the concentration of NaOH solution reaches to the critical value (e.g., 20 wt%, in this case), the dehydrated hydroxide ions could easily penetrate and disrupt the cellulose lattice, and the crystalline structure of the cellulose started to be swelled and relaxed. After a complete swollen state formed, the hydrated hydroxide ions penetrated the inside of the crystal, and underwent a thorough reaction with the cellulose molecules (Liu and Hu 2008). The CI of untreated BWP was found to be 70.5%, which was close to the CI of microcrystalline cellulose (Liu et al. 2010). After acid hydrolysis treatment, CNC I and CNF I exhibited decreased CI values of 66.4% and 57.6%, respectively. After the alkaline treatment and acid hydrolysis, the CI values of CNC II and CNF II were 73.6 % and 71.5 %, respectively. The CI

values for cellulose I and II cannot be directly compared, but in general comparable crystallinities of I and II should lead to substantially lower CI values for cellulose I (Han et al. 2013). The subtle differences between BWP and CNC II (or CNF II) were not significant enough to be considered as an increase in crystallinity.

3.3.3 Morphology of CNCs and CNFs (I and II)

A comparison of the morphology of CNCs (I, II) and CNFs (I, II) isolated from BWP by different chemical treatments is presented in Figure 3.3. The insert images show the dispersion states of these four samples at the 1.0 wt% concentration level. Raw BWP contained large sized fiber bundles composed of many microfibrils. These fiber clusters had an average length larger than 300μm and an average width of 15μm (Table 3.1). Because of their large dimension, the BWP without any treatment did not suspend, but highly precipitated in water. After treatment with 64 wt% H_2SO_4 followed by a further HPH process, CNC I suspension was converted into the light purple transparent homogenized CNC I suspension without any visible flocculate (Insert in Figure 3.3a and Figure 3.4f). The amorphous regions of cellulose were preferentially hydrolyzed by sulfuric acid, while the crystalline regions that had a higher resistance to acid attack remained intact (Habibi et al. 2010), resulting in the isolation of nano-sized cellulose crystals. The dispersion of the CNC I in water was promoted by the charged surface sulfate esters, which were generated by the reaction between hydroxyl groups of cellulose and sulfuric acid, and was further improved by the high turbulence and shear forces during HPH treatment (determined by the following optical transmittance measurement). Figure 3.3a revealed that homogenized CNC I were well-isolated and exhibited rod-like structure (wider at the middle than at the ends), which was a typical observation of dispersed cellulose nanocrystals (Kvien et al. 2005). The average length and width of homogenized CNC I were 149 $\pm$ 40 and 9 $\pm$ 2 nm,

respectively (Table 3.1). These values were consistent with those of previous literatures (Beck-Candanedo et al. 2005; Liu et al. 2010).

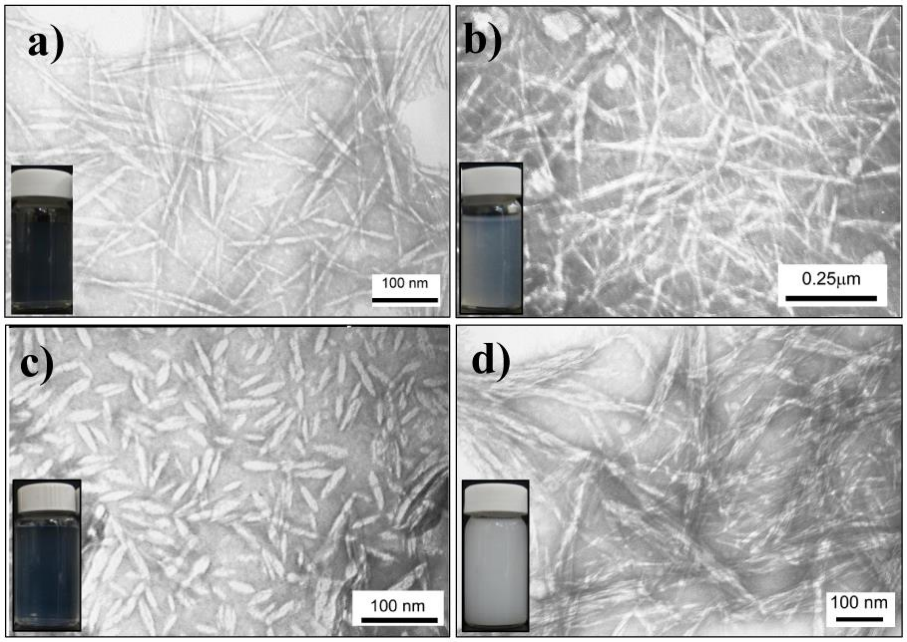

Figure 3.3 TEM images of CNC I (a), CNF I (b), CNC II (c) and CNF II (d), and the insert in each image representing the corresponding dispersion state of each cellulose suspension at the concentration of 1.0 wt%. (All the dispersions were prepared by a 2h stirring after preparation, and the photograph was taken after a resting of 48 h).

After being subjected to the combined treatment of 48 wt% H_2SO_4 and homogenization, BMP was acid-hydrolyzed into larger–sized CNF I instead of CNC I (Figure 3.3b). CNF I dispersed homogeneously in water and formed a stable purple colloidal suspension without visible aggregation (Insert in Figure 3.3b and Figure 3.4f). Due to stress on drying down on the substrate, or induced compression or tension stress on removal from the cell wall (Manley 1964), CNF I became deformed and kink without buckling. The individual nature of CNF I can be clearly observed in Figure 3.3b, and CNF I oriented longitudinally in bundles. The average length and width of CNF I obtained were estimated to be 732 ± 208 nm and 21 ± 7 nm, respectively. Typical CNFs had a diameter in the 10 to 40 nm range and lengths exceeding several micrometers (Henriksson et al. 2008; Sehaqui et al. 2010). Compared with the size of

reported CNFs produced from wood, the width of obtained CNF I was similar and the lengths were, however, smaller. Thus, these materials were relatively short CNFs.

Table 3.1 Dimension parameters and zeta potential of raw wood fiber, CNC, and CNF (I and II).

Sample	Dimension		Aspect Ratio [b]	Zeta potential (mV)
	Mean ± Standard Deviation [a] (nm)			
Wood fiber	Length	> 300,000	>20.0	ND [c]
	Width	15,000 ± 4,000		
CNC I	Length	149 ± 40	16.6	-57.07 ± 1.06
	Width	9 ± 2		
CNF I	Length	732 ± 208	36.6	-32.61 ± 1.12
	Width	21 ± 7		
CNC II	Length	46 ± 18	9.4	-0.63 ± 0.08
	Width	5 ± 1		
CNF II	Length	616 ± 200	38.0	ND
	Width	16 ± 4		

[a] Based on 100 samples per group.

[b] A ratio of mean sample length to mean sample width.

[c] Not determined.

The acid-hydrolysis conditions are known to affect the properties of produced cellulose particles. Longer hydrolysis time and/or increased acid-to-pulp weight ratio resulted in a smaller fiber dimension, while higher hydrolysis temperature induced some side reactions such as dehydration or carbonization, leading to dark yellow or black products (Beck-Candanedo et al. 2005; Dong et al. 1998). In the present study, CNF I was ~5 times longer in length and ~2.5 times thicker in width compared with CNC I (Table 3.1). It was thus illustrated that the particle size was successfully controlled by varying the acid concentration with other conditions being

optimized. During the hydrolysis in an acidic environment, the cellulose molecular chains that existed in the amorphous portions were randomly oriented in a spaghetti-like arrangement leading to a more accessible non-crystalline domain. Consequently, the acid diffused preferentially into the amorphous regions, hydrolyzed the accessible glycosidic bonds and transversely releasing individual crystallites (Dong et al. 1998).

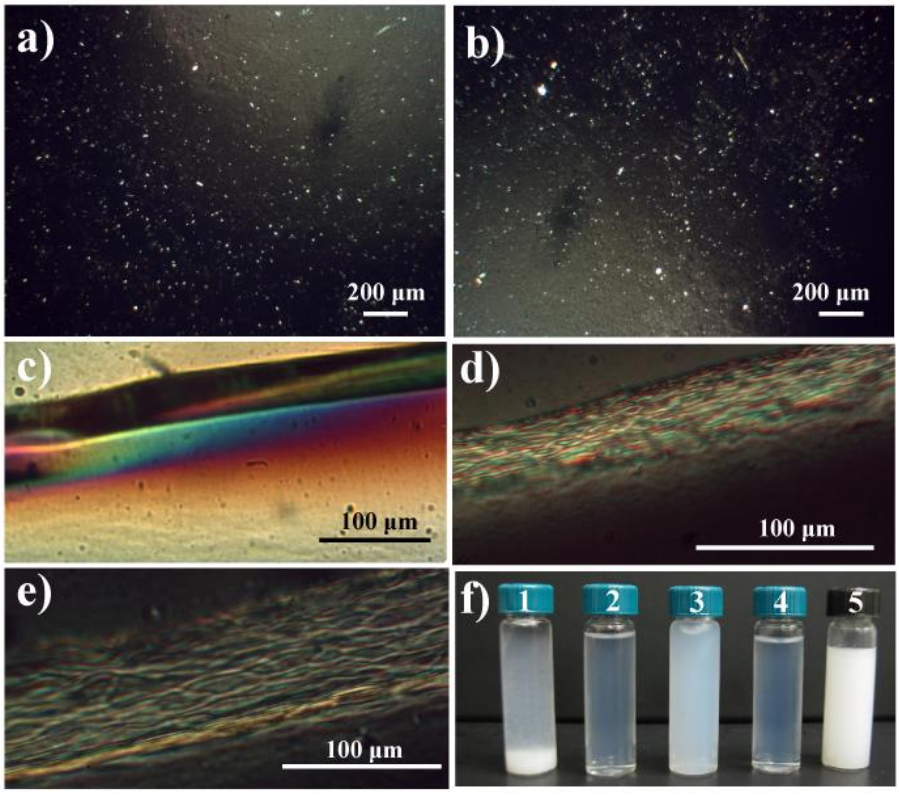

Figure 3.4 Aqueous suspensions of 1.0 wt% CNC I (a, c) and1.0 wt% CNF I (b, d and e) viewed through crossed polarizers showing the macroscopic birefringence, and the dispersion states (c) of non-homogenized cellulose suspension (1), CNC I (2), CNF I (3), CNC II (4), and CNF II (5) suspensions at the 1.0 wt% concentration. (All dispersions were prepared by a 2h stirring after preparation, and the photograph was taken after a resting of seven days).

Because of the surface esterification of hydroxyl groups of cellulose with sulfate groups, the surfaces of CNC I and CNF I carried a mutually repulsive negative electrostatic charge (confirmed by FTIR, XPS and ζ measurements), and thus formed stable suspensions or hydrogel in water. It was reported that the rigid rod-like cellulose I nanoparticles had a strong tendency to

align along a vector direction in water, creating a birefringent phenomenon that can be observed under POM (Lima and Borsali 2004). The 1.0 wt% dispersions of CNC I and CNF I both showed typical birefringence when observed between crossed polarizers, thus suggesting a liquid crystalline behavior (Figure 3.4a-e). The birefringent nature of H_2SO_4-prepared cellulose nanoparticles depends on the suspension concentration. Interestingly, CNC I and CNF I tended to self-organize into liquid crystalline alignment at a higher concentration, leading to a stronger birefringence. After 12h of standing, the edge of suspension sample was concentrated due to the slow evaporation of water, creating an iridescent pattern and the macroscopic birefringence (Figure 3.4c-e).

After BWP was subjected to mercerization treatment (20 wt% NaOH) before acid-hydrolysis (64 wt% H_2SO_4), the crystal structure of cellulose molecules was transformed from I to II (confirmed by the XRD and FTIR data above), and the resulting CNC II material is shown in Figure 3.3c. The morphology and dispersion state of CNC II were similar to those of CNC I (Insert in Figure 3.3c and Figure 3.4f), but their dimension was much smaller. As shown in Table 3.1, the average width and length of CNC II were 55% and 31% of those of CNC I, respectively. It was recently reported that the CNC II prepared by treatment of microcrystalline cellulose with sulfuric acid with controlled hydrolysis process also tended to be shorter and thinner than the CNC I, and their size distributions were less polydispersed (Sebe et al. 2012). Presumably, the interpretation of size difference could be inferred from the mechanism of mercerization and acid-hydrolysis. The acid hydrolysis of cellulose is a heterogeneous process. During the mercerization process, the cellulose fibers were converted into a swollen state that involved formation of one or more soda-cellulose complexes in aqueous sodium hydroxide, providing larger space and more opportunities for hydronium ions to penetrate the swollen cellulose chains to break down the

glycosidic bonds in amorphous regions (Dinand et al. 2002; Dong et al. 1998). In addition, after the BWP was treated with 20 wt% NaOH and then with 48% H_2SO_4, CNF II was isolated (Figure 3.3d). The morphology and dimension of CNF II obtained were similar to those of CNF I (Table 3.1). CNF II colloidal suspension was homogeneous and stable, but the color was white and turbid compared with CNF I at the same concentration (Insert in Figure 3.3d and Figure 3.4f). It was shown that the parallel-to-antiparallel reorganization of cellulose chains could also be initiated in the amorphous regions of alkali-swollen nanofibers. The molecules from adjacent cellulose I nanofibers with opposite chain polarity could then rearrange and crystallize into antiparallel cellulose II upon being washed in water (Zuluaga et al. 2009).

The aspect ratio is one of the most important parameters in determining reinforcing capability of CNCs and CNFs (Wang et al. 2007). As shown in Table 3.1, the corresponding aspect ratios of CNC I, CNF I, CNC II and CNF II were 16.6, 36.6, 9.4 and 38.0, respectively. Therefore, a greater reinforcing efficiency and further applications related can be expected from these nanoparticles, especially CNF I and II (Kamphunthong et al. 2012).

3.3.4 UV Optical Transmittance of Cellulose Dispersions

Figure 3.5a shows UV–Vis light transmittance spectrum of water dispersions of non-homogenized CNC I (N-CNC I), homogenized CNC I and CNF I at the concentrations of 0.05 and 0.1 wt% at a visible wavelength range of 300 to 800 nm. The visible light transmittance (Tr., %) of cellulose suspension largely depends on particle size and the dispersion of particles in the aqueous suspension. At the same concentration level, the light transmittances of non-homogenized CNC I suspensions were lower than those of homogenized CNC I suspensions in the whole measurement range of wavelength. The mean Tr. of 0.05 and 0.1 wt% CNC I suspensions were 91.32% and 84.87%, respectively. After HPH process, the mean Tr. of 0.05

and 0.1 wt% CNC I suspensions increased to 97.76 and 95.48%, respectively. Without HPH process, acid-hydrolyzed CNC I formed into larger assembled aggregates in water, leading to an undesirable dispersion of CNC I and the consequent phase separation in water (Figure 3.4f). When CNC I aqueous suspension was exposed under visible spectrum of sunlight, the incident light was not only absorbed within the larger CNC I aggregates, but was reflected or scattered at interfaces of separated phases, resulting in little light being transmitted through the CNC I suspension (Yu et al. 2009). Therefore, HPH process promoted the dispersion of CNC I in water. However, the morphology of each CNC I was mostly unchanged after homogenization, suggesting that the fifth pass HPH process only dispersed CNC I but did not reduce their dimension (determined by the TEM results above). At each concentration level, CNF I suspension showed a much lower Tr. than that of CNC I suspension at 300 to 800 nm wavelength range. Compared with the CNC I suspensions, the mean Trs. of 0.1% and 0.05% CNF I suspensions decreased by 38.81% and 23.17%, respectively. This reduction in light transmission suggested that the transmittances of cellulose suspensions decreased with the increase of the size of cellulose particles. The average length of CNF I (732 nm) was almost five times longer than that of CNC I (149 nm) (Table 3.1). When the cellulose suspension is subjected to visible light, the reflection and refraction on the surface of cellulose particle may theoretically occur if the particle size is larger than 400 nm, resulting in a loss of light transmittance (Tang and Liu 2008). This phenomenon was also demonstrated by the photographs of cellulose suspensions (Inserts in Figure 3.3). At the same concentration, the color of CNC I was much lighter than that of CNF I.

Figure 3.5b shows the luminous transmittance spectra of CNC II and CNF II aqueous suspensions with the concentrations from 0.05 to 1.0 wt%. The transmittance of CNC II and

CNF II suspension increased with the decrease of the cellulose concentration across the whole wavelength range used.

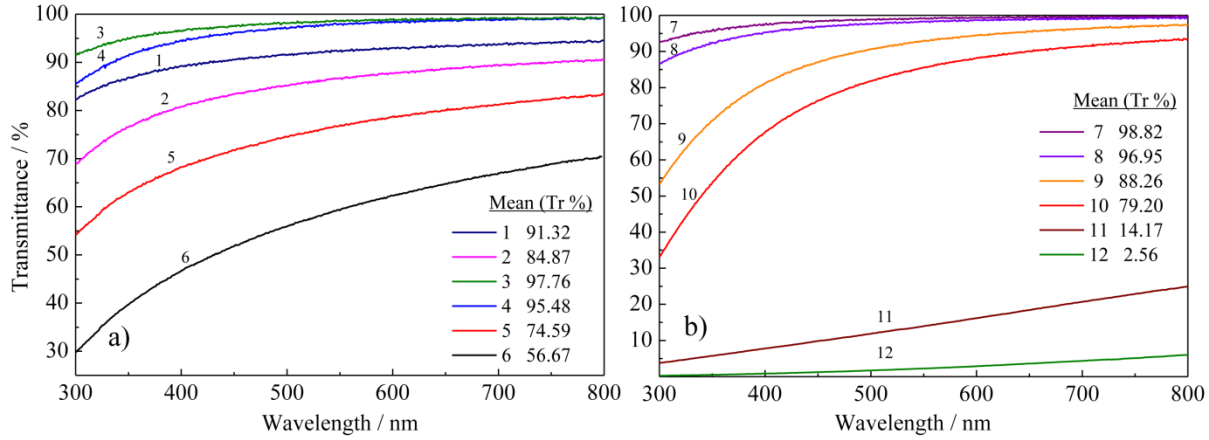

Figure 3.5 UV–Vis transmittance spectra of water dispersions of (a): 1-0.05wt% N-CNC I, 2-0.1wt% N-CNC I, 3-0.05wt% CNC I, 4-0.1wt% CNC I, 5-0.05wt% CNF I, and 6-0.1wt% CNF I, and (b): CNC II (7-0.05wt%, 8-0.1wt%, 9-0.5wt%, and 10-1.0wt%), and CNF II (11-0.05wt%, and 12-0.1wt%).

With substantially increased cellulose concentration, the probability of reflection/refraction of visible light between particles per unit volume increased, and less light was transmitted through the suspension. Consequently, the mean Tr. of CNC II suspension decreased from 98.82 to 79.20% when the cellulose concentration increased from 0.05 to 1.0 wt%. Similar results were also observed for CNC I and CNF I suspensions (Figure 3.5a). At each concentration level, CNF II suspension showed much lower Tr. than that of CNC II suspension at 300 to 800 nm wavelength range. Compared with the CNC II suspensions, the mean Tr. of 0.1wt% and 0.05wt% CNF II suspensions decreased by 94.39% and 84.65%, respectively. This result indicated that the particle size had stronger effect on the Tr. of cellulose II than that of cellulose I. In addition, for CNC II and CNC I, when the wavelength of incidence light ranging from 600 to 800 nm, 0.05% and 0.1% suspensions basically presented the same Tr. at each wavelength, which differed from the light transmittances at wavelength 300–600 nm. This trend

indicated that for the CNC aqueous suspension with a concentration lower than 0.1%, the concentration variation had little effect on the Tr. at wavelength 600–800 nm. Furthermore, the differences of Tr. between two crystal structures were also observed. At each concentration level, the Tr. of CNC II was slightly higher than that of CNC I over the whole range of wavelength. A possible reason was that the average length of CNC II (46 nm) was almost three times smaller than that of CNC I (149 nm) (Table 3.1).

3.3.5 Surface Charges and Electrostatic Repulsion Determined by Zeta Potential and XPS Measurements

The zeta potential (ζ) has been used to study the surface charges of cellulose materials (Iyer and Jayaram 1971). To investigate the effect of the surface charges on the lyophilization-induced self-assembling behavior of the obtained cellulose samples, the ζ values of CNC I, CNC II, CNF I, and CNF II in aqueous suspensions (0.05 wt%) were measured (Table 3.1). Based on the optical transmittance results at the same concentration, the mean Tr. of the CNF II suspension was much lower than the other samples (Figure 3.5), indicating that the CNF II material was not as stable as the other three samples in aqueous suspensions. The instability of CNF II in the suspension at the 0.05 wt% level made it difficult to determine its zeta potential value. Measurements on CNC I, CNC II, and CNF I showed that they carried negative electrical charges because of the presence of sulfate ester (-O-SO_3-) groups on their surfaces (also as determined from FTIR and XPS measurements). The ζ values of CNC I, CNC II, and CNF I were -57.07 ± 1.06, -0.63 ± 0.08, and -32.61 ± 1.12 mV, respectively, which were within the typical ζ range of cellulose particles as previously reported (Boluk et al. 2011; Boluk et al. 2012; Hasani et al. 2008; Teixeira et al. 2010). The ζ (absolute value) of CNC I was higher than that of the CNF I, indicating that CNC I carried more -O-SO_3- groups on their surfaces. No effective methods could remove the sulfate group from the sulfuric acid- hydrolyzed material completely

and the esterification levels of cellulose particles highly depend on hydrolysis time and acid concentrations (Dong et al. 1998; Gu et al. 2013). Hence, the possible reason was that higher H_2SO_4 concentration introduced more sulfate groups on the CNC I surfaces during the acid-hydrolysis process. It was also found that the ζ (absolute value) of CNC II was much lower than that of CNC I or CNF I. Therefore, the sulfur content of CNC II was much lower than that of CNC I or CNF I, which was consistent with the FTIR and XPS analysis data. Some Na^+ ions absorbed by the CNC II and CNF II during the NaOH pretreatment still remained on the fiber surfaces even after fiber washing as shown by the following XPS results (Figure 3.6c). It was reported previously that the absolute value of ζ and the electrostatic repulsion of cellulose nanoparticles were reduced due to the electrostatic screening effect of cation counterion Na^+ (Zhong et al. 2012). Based on the double layer theories proposed by Helmholtz in 1879, the counterions in solution can shield the surface charges of particles, resulting in the screening effect of cation counterion Na^+ in acid-hydrolyzed cellulose aqueous suspension (Boluk et al. 2011). Therefore, the lower absolute value of ζ for CNC II was expected and was due to the adsorption of residue Na^+ counterions on negatively charged CNC II surfaces. It is well known that negatively charged particles are repelled from each other, leading to the electrostatic repulsion among them. The negatively charged cellulose particles thus had mutual repulsion with each other to form an electrostatically stabilized dispersion in an aqueous suspension. Consequently, the CNC I with the higher absolute value of ζ and more sulfate charges was expected to have a stronger mutual repulsion, while the CNC II with the lower absolute value of ζ should possess a relatively weaker electrostatic repulsion with each other. Typical XPS survey spectra of CNC II and CNC I are shown in Figures 3.6a and 3.6b, respectively. The peaks centered at the 535.0 and 289.0 eV positions were attributed to O 1s and C 1s, respectively.

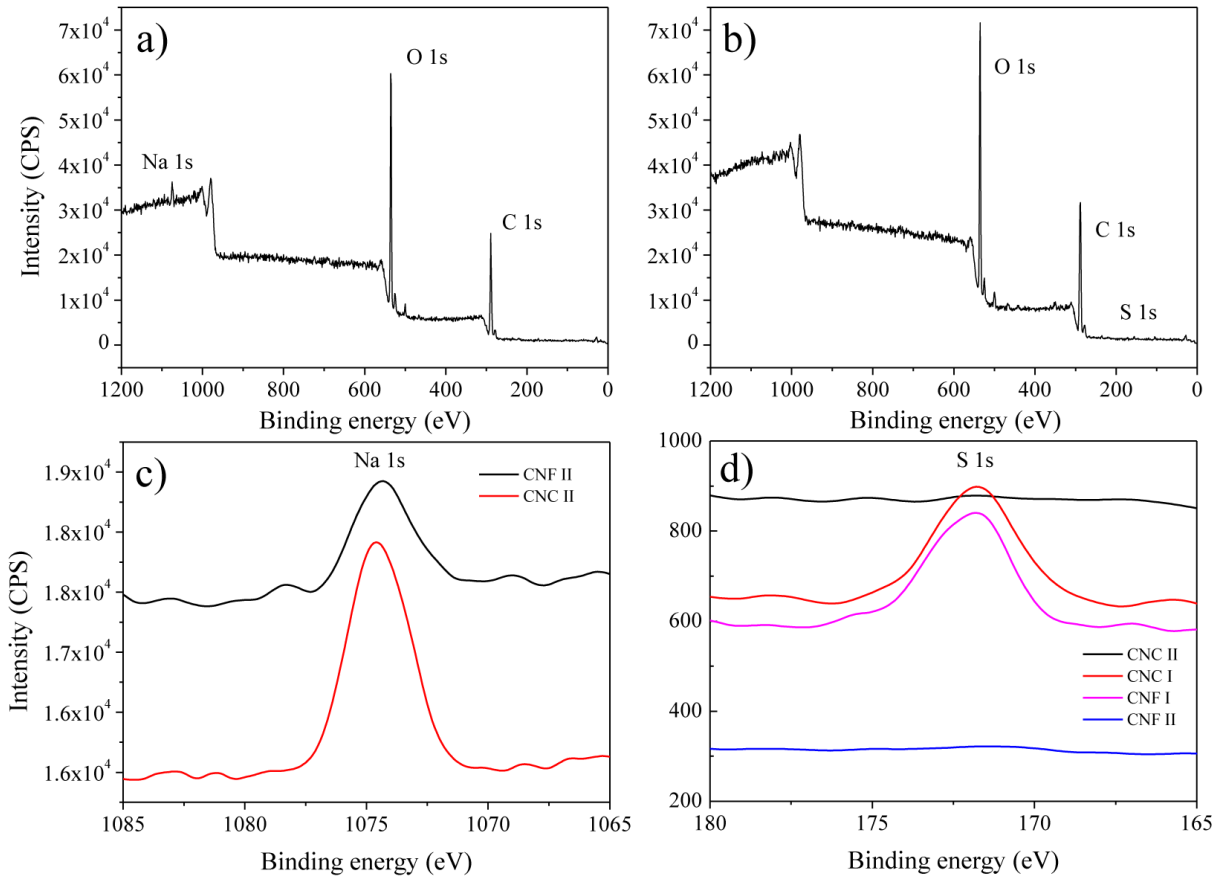

Figure 3.6 Typical XPS survey spectrum of CNC II (a) and CNC I (b), and comparisons of Na 1s (c) and S 2p (d) peaks for various materials.

CNC II and CNF II had the peaks at 1074.5 eV corresponding to Na 1s (Figure 3.6c), indicating the presence of residue Na^+ ions on the surfaces of CNC II and CNF II caused by the NaOH pretreatment. The peaks at 171.0 eV were ascribed to S 2p (Figure 3.6d). To characterize the relative atomic percentage of S 2p for each sample, the atomic ratios of sulfur to oxygen (S/O) were calculated from corresponding peak area based on the high-resolution spectrum of S 2p. The S/O of CNC I and CNF I were 1.112% and 1.051%, respectively. The sulfur charging degrees of CNC II and CNF II were less than 0.1%. Therefore, CNC I carried more sulfate groups than CNF I, while no detectable sulfur element at the surfaces of CNC II and CNF II, confirming the results of FTIR and ζ measurements. Compared with the theoretical peak

positions of S 2p (165.20 eV), O 1s (531.0 eV), C 1s (284.5 eV), and Na 1s (1071.8 eV), the measured binding energy were slightly shifted to higher values. In the present XPS measurements, cellulose samples are subjected to charging effects because of their insulating nature, resulting in the shifting of spectrum on the energy scale.

3.3.6 Morphology and Microstructure of Self-assembled CNC and CNF during Freeze Drying

It is well known that the particle size and concentration in suspension are crucial factors for controlling morphology of freeze-dried foam (Deville and Nalla 2006; Lee and Deng 2011). The freeze–dried CNC I, CNC II, CNF I and CNF II products were white and fluffy, presenting a foam structure. However, some distinctive differences of morphology and microstructure among these samples were observed by FE-SEM at the micrometer scale (Figures 3.7a-3.7l).

For the freeze-dried CNC I at the concentrations of 0.5 and 1.0 wt%, the lamellar structured foam composed of aligned thin membrane layers with width between 0.5 and 3 μm was fabricated (Figure 3.7a and 3.7b). Each layer was created in parallel to each other and presented a smooth surface and homogeneous character throughout the entire layer. It can be clearly seen that these layers actually consisted of oriented micro-sized cellulose fibers with an average diameter of 1~3μm (Insert in Figure 3.7b). This result indicated that nano-sized CNC I (149 ± 40 nm in length, and 9 ± 2 nm in width) were first longitudinally self-assembled into the larger-sized cellulose fibers that were further self-organized in parallel to form a film-like structure during freeze drying. The significant coalescence of cellulose subunits caused by freeze drying process was reported previously (Deng et al. 2009; Jin et al. 2004). Compared with a similar observation reported by Sehaqui et al. (Sehaqui et al. 2010), the layers we obtained had a higher compactness and no visible porosity was seen. Freeze-drying 0.5 and 1.0 wt% CNF I

aqueous suspensions resulted in similar layered structure (Figures 3.7e and 3.7f), indicating that CNF I also showed the self-organizing phenomenon.

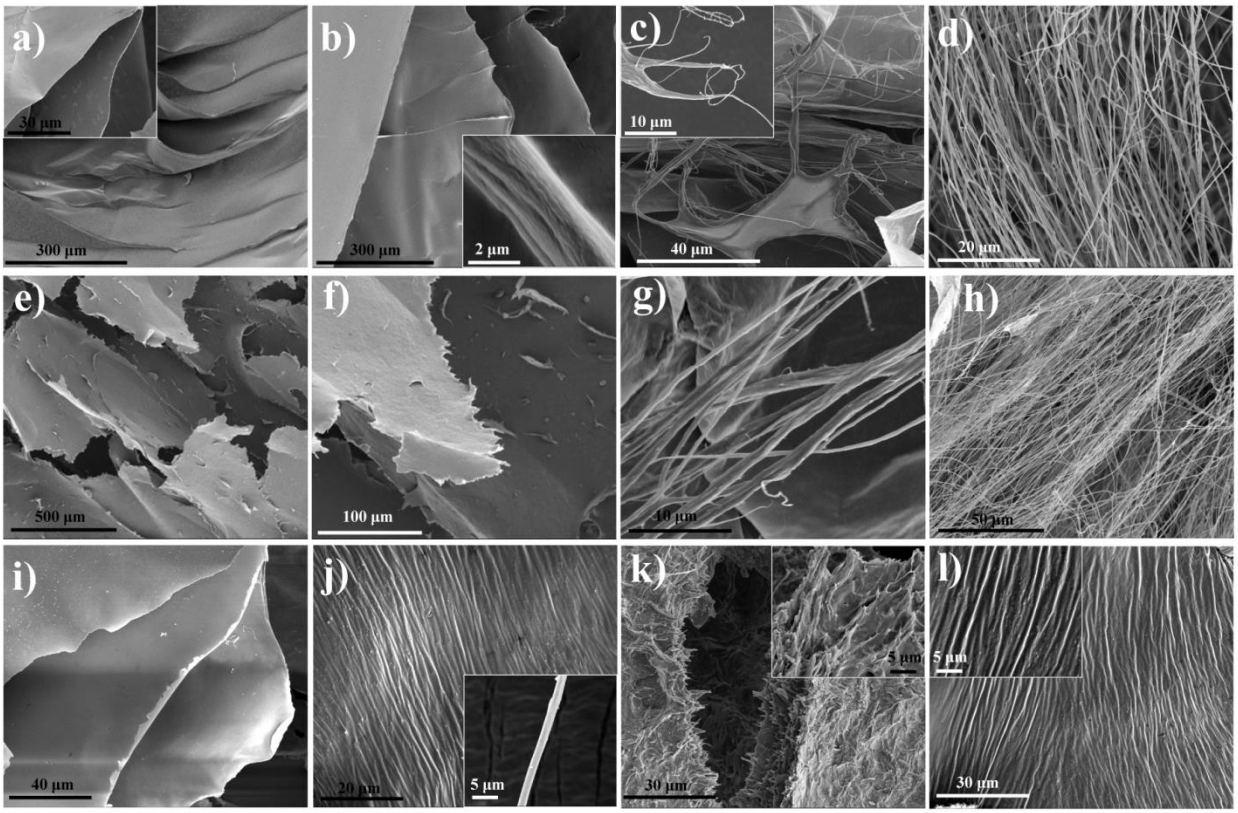

Figure 3.7 FE-SEM photomicrographs of freeze-dried CNC I at the concentration of 1.0 wt% (a), 0.5 wt% (b), 0.1 wt% (c) and 0.05 wt% (d), and freeze-dried CNF I at 1.0 wt% (e), 0.5 wt% (f), 0.1 wt% (g) and 0.05 wt% (h), and freeze-dried CNC II at 1.0 wt% (i), and 0.05 wt% (j), and freeze-dried CNF II at 1.0 wt% (k), and 0.05 wt% (l).

However, the fracture surface of CNF I was not as smooth as that of CNC I and visible dendrites stood out from the fractured surface, presumably due to the lager dimensions of CNF I. This result revealed that the CNC dimensions had an important effect on the lyophilization-induced self-assembly behaviors. At high concentration levels (0.5 to 1.0 wt%), larger size CNF I could hardly form the smooth surface and presented homogeneous character throughout the entire layer. After the concentration was diluted to 0.05 wt%, the CNC I and CNF I aqueous suspensions both self-assembled into oriented ultra-fine fibers with diameters of 0.57 ± 0.17 and

1.02 ± 0.27 μm instead of sheet-like structure by sublimating ice molecules (Figures 3.7d and 3.7h). The mean diameter of ultra-fine fibers formed by CNF I was twice as much as that of CNC I, indicating that the diameter of self-assembled ultra-fine fibers increased with the dimension of cellulose particles at the 0.05 wt% concentration level. In addition, the zeta potential and XPS results all revealed that more sulfate groups were introduced onto the surfaces of CNC I compared with CNF I, resulting in a stronger electrostatic repulsion between CNC I. It is thus inferred that the weaker mutual repulsion of CNF I can promote their self-organization into ultra-fine fibers. Therefore, at the 0.05 wt% concentration level, more surface charges of cellulose nanoparticles led to the smaller diameters of self-assembled ultra-fine fibers. A similar effect of surface charges on the lyophilization-induced self-assembling behavior was further observed between CNC II and CNC I at the 0.05 wt% concentration level. It was also found that the widths of self-assembled ultra-fine fibers were much narrower than those of fiber clusters found in original BWP (Table 3.1). The similar intriguing self-assembling behavior of dilute CNC suspensions prepared from rice straw was reported by Lu and Hsieh (Lu and Hsieh 2012). They obtained the ultra-fine cellulose fibers from acid-hydrolyzed rice straw with a mean width of ~0.386 μm under a different freeze-drying condition. However, the long cellulose fibers they obtained were randomly arranged into a network structure instead of an oriented arrangement in the present research. One reason is the difference of cellulose source, and the other reason is the variation of freezing conditions. They quickly froze the samples by adding liquid nitrogen, whereas the dilute cellulose suspension was frozen in a freezer at -75 ℃ for 2 hours in this study, which allowed the oriented self-organizing behavior of ultra-fine fibers to occur during this time. In this way, the cellulose particles had enough time to adjust and rearrange their position during

the freezing process. The self-assembly mechanism of cellulose during freeze-drying was detailed below.

The hydrogen bonding arrangement plays an important role in the self-assembling properties of cellulose suspension. Therefore, the difference of hydrogen bonding systems between cellulose I and II is thought to affect the self-organizing behavior of cellulose particles in aqueous suspension during freeze-drying process. However, lyophilization-induced self-assembling behavior of cellulose II has not been thoroughly reported in the literature so far. To investigate the effect of cellulose crystal structure on the self-assembling behavior of cellulose nanoparticles, CNC II and CNF II aqueous suspensions at the concentration of 0.05 wt% and 1.0 wt% were freeze-dried. For the freeze-dried CNC II at the concentration of 0.05wt%, many micro-sized cellulose fibers with an average diameter of ~1.5μm were found (Figure 3.7j). When the concentration was increased to 1.0 wt%, a lamellar structured foam composed of thin membrane layers was created (Figure 3.7i). This layered-structure morphology was identical with that of freeze-dried CNC I at the same concentration (Insert in Figure 3.7a), indicating that cellulose crystal structure had insignificant effect on the self-assembling properties of 1.0 wt% CNC suspensions. For the freeze-dried CNF II at the concentration of 0.05 wt%, CNF II aqueous suspensions self-assembled into highly oriented ultra-fine fibers with diameters of ~1μm (Figure 3.7l). This phenomenon was also found in freeze-dried 0.05 wt% CNF I suspension (Figure 3.7h). At the concentration of 1.0 wt%, many aligned macro-sized cellulose fibers stood out from the fractured surface of freeze-dried CNF II (Figure 3.7k). In fact, these layers were composed of oriented macro-sized cellulose fibers when it was observed along the perpendicular to aligned direction (Insert in Figure 3.7k). However, the surface of CNF II was not as homogeneous as that of CNF I, presumably because of different cellulose crystal structure.

3.3.7 Mechanism of lyophilization-induced self-assembling behavior of cellulose particles

A possible mechanism could be inferred from the basic physics of ice crystal growth, the interaction between cellulose particles, and the chiral nematic anisotropic nature of liquid crystalline polymer. Figure 3.8 shows a scheme presenting the formation mechanism of the lamellar geometry and the alignment of ultra-fine fibers in the freeze-drying process. Before steady-state freezing process, CNC and CNF suspensions formed stable and homogenous aqueous suspensions because of the inter-particle electrostatic repulsion provided by the negatively charged sulfate groups on the surfaces of cellulose particles. When a cellulose suspension with suitable granulometry was frozen under steady-state conditions, ice crystals gradually grew in the same direction as the temperature gradient and created a lamellar microstructure oriented in a direction parallel to the movement of the freezing front (Deville and Nalla 2006; Lee and Deng 2011). Simultaneously, the cellulose particles were expelled from the growing ice crystals and squeezed into the space between ice crystals or dendrites. As a result, the concentration of cellulose particles increased in the space among growing ice crystals during the freezing of water. When the critical concentration of sulfated cellulose necessary for the formation of ordered nematic phases was reached (typically 1.0 to 10 wt%), the rod-like cellulose particles spontaneously formed ordered structure in the space between growing ice crystals (Habibi et al. 2010). Once the freezing process was completed, the original homogenous suspension system was destroyed and transformed into an ice-template structure by the lyophilization-induced physical interaction. During the freeze drying process, ice molecules were gradually sublimated from the lamellar ice-template system. As a result, the suspended cellulose particles were concentrated and trapped in the space between these ice crystals, generating a replica of the original ice-template (Lee and Deng 2011). These concentrated cellulose particles

compactly rearranged and well self-assembled along the longitudinal direction into larger-sized cellulose microfibers via strong hydrogen bonds and van der Waals forces (Dash et al. 2012; Lee and Deng 2011). It was reported that the cellulose nanocrystals were well aligned along the axis of each self-assembled fiber (Lu and Hsieh 2012). In addition, the ends of these ultra-fine fibers were not prevalent in the SEM observations (Figures 3.7d, 3.7h, 3.7j, and 3.7l), indicating the lengths of these self-assembled cellulose fibers probably reached millimeter-scale. For highly concentrated suspensions (0.5 to 1.0 wt%), the gap between the self-assembled microfibers was small enough for the formation of hydrogen bonding and tight bonds with neighboring microfibers, and these adjacent microfibers aligned along the freezing direction to form a dense layered structure due to the linking with adsorbed/bound water and the momentum exerted by growing ice crystals (Lee and Deng 2011; Liu et al. 2011). By contrast, the space between self-assembled microfibers became larger when the concentration of suspensions was diluted to the 0.05 wt% level, resulting in the weakening of hydrogen bonding and interfacial attraction between microfibers. In addition, rod-like cellulose particles tended to spontaneously form parallel configuration in diluted aqueous medium since the effective excluded volume is zero (Eichhorn 2011). Therefore, the 0.05 wt% CNC and CNF aqueous suspensions both self-assembled into oriented ultra-fine fibers instead of sheet-like structure during lyophilization (Figures 3.7d, 3.7h, 3.7j, and 3.7l). At the semi-dilute concentration (0.1 wt%), self-assembled layers and oriented ultra-fine fibers coexisted in the foam (Figures 3.7c and 3.7g), presenting an intermediate stage of the structure transition from membrane layers to oriented ultra-fine fibers. The insert in Figure 3.7c showed that the membrane layers obtained were composed of self-assembled ultra-fine cellulose fibers. In addition, at the concentration of 0.05 wt%, the average diameter of ultra-fine fibers assembled from CNC II was larger than that from CNC I. Because

the mean width of CNC I was almost twice as long as CNC II, the estimated quantity of CNC II within the cross section of each ultra-fine fiber was much more than that of CNC I.

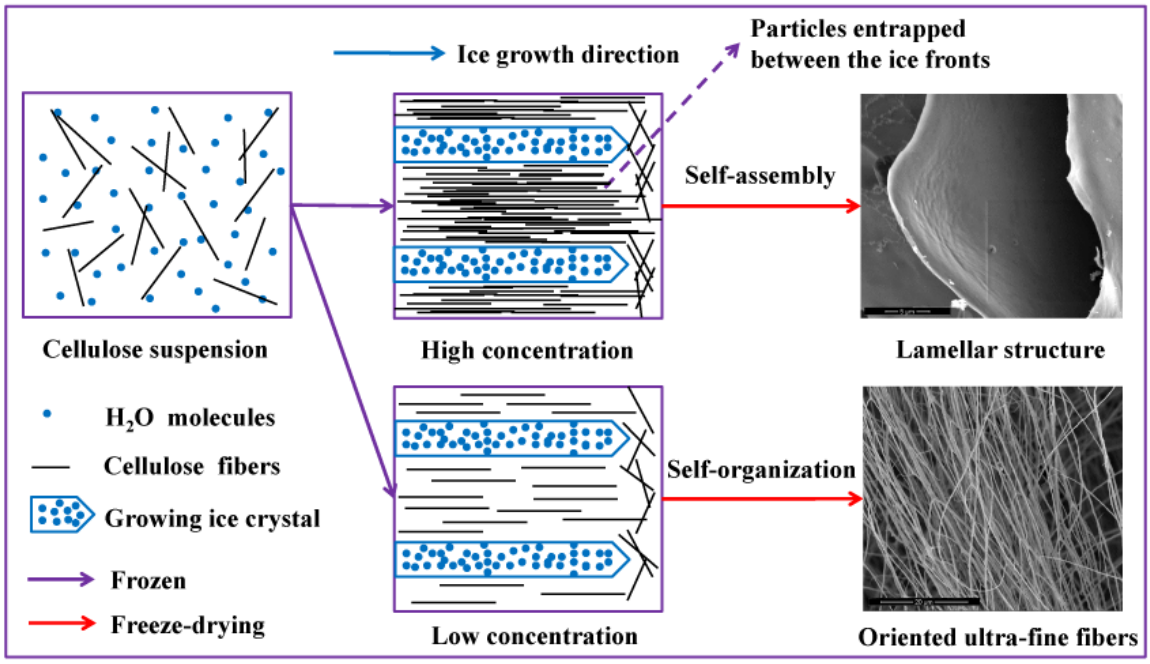

Figure 3.8 Schematic of possible formation mechanism of the lamellar geometry and the alignment of ultra-fine fibers during the freeze-drying process.

This distinction of self-assembling behavior might be induced by the different intra- and inter- hydrogen bonding patterns within cellulose I and II molecular chains. Cellulose I has two intra-molecular hydrogen bonds at (O)6-(OH)2 and (O)5-(OH)3, and an inter-chain hydrogen bond between (O)6-(O)3. When the cellulose fibers are swollen in a NaOH solution, the hydrated hydroxide ions penetrate the internal crystals, and cause the chain rearrangements from parallel cellulose I to anti-parallel cellulose II with a changed inter-/intra-hydrogen bonding networks. Cellulose II possesses an intra-chain hydrogen bonding at (O)5-(OH)3 and two inter molecular hydrogen bond at (O)2-(OH)6 and (O)3-(OH)6. Besides, an inter-sheet interaction between (O)2-(OH)2 that is absent in cellulose I also exists in cellulose II hydrogen bonding system (OSullivan 1997). Furthermore, the hydrogen bonds in cellulose II (average bond length of 0.272 nm) is

shorter and stronger those in cellulose I (average bond length of 0.280 nm) (Jiang et al. 2011). Besides, IR index values showed that CNC II had more hydroxyl groups on the crystal surface. These factors probably promoted the congregating and self-assembly of CNC II (Determined by FTIR results). However, the effect of crystal structure on the self-assembling behavior reduced with the increasing concentration. At the concentration of 1 wt%, the layered-structure morphology self-assembled from cellulose II was almost identical with that of CNC I. As discussed before, in addition to the particle size and crystal structure, less surface charges can promote the lyophilization-induced self-assembling behavior of cellulose nanoparticles. Based on the FTIR, zeta potential and XPS results, less negatively charged CNC II possess a relatively weaker mutual electrostatic repulsion than CNC I. As a consequence, CNC II was easier to self-assemble into wider ultra-fine fibers than CNC I.

3.4 CONCLUSIONS

CNCs and short CNFs with cellulose I and II crystalline allomorphs were extracted from BWP. The particle size, crystal structure and dispersion state were successfully controlled by using different acid concentration, alkaline pretreatment and high-pressure homogenization. Cellulose concentration, particle size, surface charge, and crystal structure significantly influenced the lyophilization-induced self-assembling behavior of the cellulose suspensions. During freeze drying, at higher suspension concentrations, the gap between the self-assembled microfibers was small enough for the formation of hydrogen bonding and tight bonds with neighboring microfibers, and these adjacent microfibers aligned along the freezing direction to form lamellar structured foam composed of aligned thin membrane layers. At diluted concentrations, due to the weakening of hydrogen bonding and interfacial attraction among the fibers, cellulose particles self-assembled into highly oriented ultra-fine fibers with different

diameters, instead of the sheet-like structure. The congregating and self-assembly of cellulose particles were promoted by larger particle size, weaker mutual electrostatic repulsion and more hydroxyl groups on their surface, resulting in a larger size of self-assembled fibers.

By freezing aqueous suspensions containing cellulose particles under suitable conditions, we demonstrated the possibility of building homogeneous scaffolds with aligned membrane layers or forming oriented ultra-fine fibers, opening their use as a template for fine-structure composites. Because of the tight association of the cellulose particles through the abundant inter-crystal hydrogen bonds, self-organized cellulose products induced by lyophilization presented extraordinary structural stability and integrity in aqueous media under mechanical stirring (Lu and Hsieh 2012). For this reason, the morphology and structure of freeze-dried foam can be controlled by adjusting cellulose concentration, crystal structure, surface charges, and particle size to obtain a tailored template, showing great promises for many potential applications, such as tissue engineering scaffolds or new biomaterials for orthopedic applications (Dash et al. 2012; Deville and Nalla 2006; Hench and Polak 2002).

3.5 REFERENCES

Beck-Candanedo S., Roman M. and Gray D. G. 2005. Effect of reaction conditions on the properties and behavior of wood cellulose nanocrystal suspensions. *Biomacromolecules* 6:1048-1054.

Boluk Y., Lahiji R., Zhao L. Y. and McDermott M. T. 2011. Suspension viscosities and shape parameter of cellulose nanocrystals (CNC). *Colloids and Surfaces a-Physicochemical and Engineering Aspects* 377:297-303.

Boluk Y., Zhao L. Y. and Incani V. 2012. Dispersions of Nanocrystalline Cellulose in Aqueous Polymer Solutions: Structure Formation of Colloidal Rods. *Langmuir* 28:6114-6123.

Bondeson D., Mathew A. and Oksman K. 2006. Optimization of the isolation of nanocrystals from microcrystalline cellulose by acid hydrolysis. *Cellulose* 13:171-180.

Dash R., Li Y. and Ragauskas A. J. 2012. Cellulose nanowhisker foams by freeze casting. *Carbohydrate Polymers* 88:789-792.

Deng M. L., Zhou Q., Du A. K., van Kasteren J. and Wang Y. Z. 2009. Preparation of nanoporous cellulose foams from cellulose-ionic liquid solutions. *Materials Letters* 63:1851-1854.

Deville S. and Nalla R. K. 2006. Freezing as a path to build complex composites (vol 312, pg 515, 2006). *Science* 312:1312-1312.

Dinand E., Vignon M., Chanzy H. and Heux L. 2002. Mercerization of primary wall cellulose and its implication for the conversion of cellulose I -> cellulose II. *Cellulose* 9:7-18.

Dong X. M., Revol J. F. and Gray D. G. 1998. Effect of microcrystallite preparation conditions on the formation of colloid crystals of cellulose. *Cellulose* 5:19-32.

Eichhorn S. J. 2011. Cellulose nanowhiskers: promising materials for advanced applications. *Soft Matter* 7:303-315.

Elazzouzi-Hafraoui S., Nishiyama Y., Putaux J. L., Heux L., Dubreuil F. and Rochas C. 2008. The shape and size distribution of crystalline nanoparticles prepared by acid hydrolysis of native cellulose. *Biomacromolecules* 9:57-65.

Gu J., Catchmark J. M., Kaiser E. Q. and Archibald D. D. 2013. Quantification of cellulose nanowhiskers sulfate esterification levels. *Carbohydrate Polymers* 92:1809-1816.

Gwon J. G., Lee S. Y., Doh G. H. and Kim J. H. 2010. Characterization of Chemically Modified Wood Fibers Using FTIR Spectroscopy for Biocomposites. *Journal of Applied Polymer Science* 116:3212-3219.

Habibi Y., Lucia L. A. and Rojas O. J. 2010. Cellulose Nanocrystals: Chemistry, Self-Assembly, and Applications. *Chemical Reviews* 110:3479-3500.

Han J. Q., Zhou C. J., Wu Y. Q., Liu F. Y. and Wu Q. L. 2013. Self-Assembling Behavior of Cellulose Nanoparticles during Freeze-Drying: Effect of Suspension Concentration, Particle Size, Crystal Structure, and Surface Charge. *Biomacromolecules* 14:1529-1540.

Hasani M., Cranston E. D., Westman G. and Gray D. G. 2008. Cationic surface functionalization of cellulose nanocrystals. *Soft Matter* 4:2238-2244.

Hench L. L. and Polak J. M. 2002. Third-generation biomedical materials. *Science* 295:1014-+.

Henriksson M., Berglund L. A., Isaksson P., Lindstrom T. and Nishino T. 2008. Cellulose nanopaper structures of high toughness. *Biomacromolecules* 9:1579-1585.

Iyer S. R. S. and Jayaram R. 1971. Zeta-Potential Studies in Cellulose Fibre-Aqueous Electrolyte Solution Systems. *Journal of the Society of Dyers and Colourists* 87:338-&.

Jiang W., Sun L. F., Hao A. Y. and Chen J. Y. 2011. Regenerated cellulose fibers from waste bagasse using ionic liquid. *Textile Research Journal* 81:1949-1958.

Jin H., Nishiyama Y., Wada M. and Kuga S. 2004. Nanofibrillar cellulose aerogels. *Colloids and Surfaces a-Physicochemical and Engineering Aspects* 240:63-67.

Johar N., Ahmad I. and Dufresne A. 2012. Extraction, preparation and characterization of cellulose fibres and nanocrystals from rice husk. *Industrial Crops and Products* 37:93-99.

Kamphunthong W., Hornsby P. and Sirisinha K. 2012. Isolation of cellulose nanofibers from para rubberwood and their reinforcing effect in poly(vinyl alcohol) composites. *Journal of Applied Polymer Science* 125:1642-1651.

Kvien I., Tanem B. S. and Oksman K. 2005. Characterization of cellulose whiskers and their nanocomposites by atomic force and electron microscopy. *Biomacromolecules* 6:3160-3165.

Lee J. and Deng Y. L. 2011. The morphology and mechanical properties of layer structured cellulose microfibril foams from ice-templating methods. *Soft Matter* 7:6034-6040.

Li R. J., Fei J. M., Cai Y. R., Li Y. F., Feng J. Q. and Yao J. M. 2009. Cellulose whiskers extracted from mulberry: A novel biomass production. *Carbohydrate Polymers* 76:94-99.

Lima M. M. D. and Borsali R. 2004. Rodlike cellulose microcrystals: Structure, properties, and applications. *Macromolecular Rapid Communications* 25:771-787.

Liu D. G., Chen X. Y., Yue Y. Y., Chen M. D. and Wu Q. L. 2011. Structure and rheology of nanocrystalline cellulose. *Carbohydrate Polymers* 84:316-322.

Liu H. Y., Liu D. G., Yao F. and Wu Q. L. 2010. Fabrication and properties of transparent polymethylmethacrylate/cellulose nanocrystals composites. *Bioresource Technology* 101:5685-5692.

Liu Y. P. and Hu H. 2008. X-ray diffraction study of bamboo fibers treated with NaOH. *Fibers and Polymers* 9:735-739.

Lu P. and Hsieh Y. L. 2010. Preparation and properties of cellulose nanocrystals: Rods, spheres, and network. *Carbohydrate Polymers* 82:329-336.

Lu P. and Hsieh Y. L. 2012. Preparation and characterization of cellulose nanocrystals from rice straw. *Carbohydrate Polymers* 87:564-573.

Mahadeva S. K. and Kim J. 2009. Electromechanical Behavior of Room Temperature Ionic Liquid Dispersed Cellulose. *Journal of Physical Chemistry C* 113:12523-12529.

Manley R. S. J. 1964. Fine Structure of Native Cellulose Microfibrils. *Nature* 204:1155-&.

Moran J. I., Alvarez V. A., Cyras V. P. and Vazquez A. 2008. Extraction of cellulose and preparation of nanocellulose from sisal fibers. *Cellulose* 15:149-159.

Oh S. Y., Yoo D. I., Shin Y., Kim H. C., Kim H. Y., Chung Y. S., Park W. H. and Youk J. H. 2005. Crystalline structure analysis of cellulose treated with sodium hydroxide and carbon dioxide by means of X-ray diffraction and FTIR spectroscopy. *Carbohydrate Research* 340:2376-2391.

OSullivan A. C. 1997. Cellulose: the structure slowly unravels. *Cellulose* 4:173-207.

Ouajai S. and Shanks R. A. 2005. Composition, structure and thermal degradation of hemp cellulose after chemical treatments. *Polymer Degradation and Stability* 89:327-335.

Peng Y. C., Gardner D. J. and Han Y. S. 2012. Drying cellulose nanofibrils: in search of a suitable method. *Cellulose* 19:91-102.

Sao K. P., Mathew M. D. and Ray P. K. 1987. Infrared-Spectra of Alkali Treated Degummed Ramie. *Textile Research Journal* 57:407-414.

Sebe G., Ham-Pichavant F., Ibarboure E., Koffi A. L. C. and Tingaut P. 2012. Supramolecular Structure Characterization of Cellulose II Nanowhiskers Produced by Acid Hydrolysis of Cellulose I Substrates. *Biomacromolecules* 13:570-578.

Segal L., Creely J. J., Martin A. E. and Conrad C. M. 1959. An Empirical Method for Estimating the Degree of Crystallinity of Native Cellulose Using the X-Ray Diffractometer. *Textile Research Journal* 29:786-794.

Sehaqui H., Salajkova M., Zhou Q. and Berglund L. A. 2010. Mechanical performance tailoring of tough ultra-high porosity foams prepared from cellulose I nanofiber suspensions. *Soft Matter* 6:1824-1832.

Svagan A. J., Samir M. A. S. A. and Berglund L. A. 2008. Biomimetic foams of high mechanical performance based on nanostructured cell walls reinforced by native cellulose nanofibrils. *Advanced Materials* 20:1263-+.

Tang C. Y. and Liu H. Q. 2008. Cellulose nanofiber reinforced poly(vinyl alcohol) composite film with high visible light transmittance. *Composites Part a-Applied Science and Manufacturing* 39:1638-1643.

Teixeira E. D., Correa A. C., Manzoli A., Leite F. L., de Oliveira C. R. and Mattoso L. H. C. 2010. Cellulose nanofibers from white and naturally colored cotton fibers. *Cellulose* 17:595-606.

Uetani K. and Yano H. 2012. Zeta Potential Time Dependence Reveals the Swelling Dynamics of Wood Cellulose Nanofibrils. *Langmuir* 28:818-827.

Wang B., Sain M. and Oksman K. 2007. Study of structural morphology of hemp fiber from the micro to the nanoscale. *Applied Composite Materials* 14:89-103.

Wang M. J., Xie Y. L., Zheng Q. D. and Yao S. J. 2009. A Novel, Potential Microflora-Activated Carrier for a Colon-Specific Drug Delivery System and Its Characteristics. *Industrial & Engineering Chemistry Research* 48:5276-5284.

Yu Z. J., Jiang Y. Q., Zou W. W., Duan J. J. and Xiong X. P. 2009. Preparation and Characterization of Cellulose and Konjac Glucomannan Blend Film from Ionic Liquid. *Journal of Polymer Science Part B-Polymer Physics* 47:1686-1694.

Yue Y. Y., Zhou C. J., French A. D., Xia G., Han G. P., Wang Q. W. and Wu Q. L. 2012. Comparative properties of cellulose nano-crystals from native and mercerized cotton fibers. *Cellulose* 19:1173-1187.

Zhong L. X., Fu S. Y., Peng X. W., Zhan H. Y. and Sun R. C. 2012. Colloidal stability of negatively charged cellulose nanocrystalline in aqueous systems. *Carbohydrate Polymers* 90:644-649.

Zuluaga R., Putaux J. L., Cruz J., Velez J., Mondragon I. and Ganan P. 2009. Cellulose microfibrils from banana rachis: Effect of alkaline treatments on structural and morphological features. *Carbohydrate Polymers* 76:51-59.

CHAPTER 4 FACILE PREPARATION OF MOULDBALE POLYVINYL ALCOHOL-BORAX HYDROGELS REINFORCED BY WELL-DISPERSED CELLULOSE NANOPARTICLES: PHYSICAL, VISCOELASTIC AND MECHANICAL PROPERTIES[3]

4.1 INTRODUCTION

Polyvinyl alcohol (PVA) is one of the most important synthetic water-soluble polymer produced in the world (Ramaraj 2007). Because of the hydroxyl groups present in each repeating molecular unit, PVA possesses strong hydrophilic and hydrogen bonding characteristics. It can react with many types of functional groups and form chemically and/or physically crosslinked hydrogels. The PVA-based hydrogels are biocompatible, biodegradable, non-toxic and non-carcinogenic (Asher et al. 2008; Kobayashi et al. 2005). Current applications of PVA-based hydrogels include bioactuators, tissue scaffolding, artificial meniscus and cornea, aortic heart valve and wound dressing (Lin et al. 2000; VI et al. 2003). PVA-based hydrogels can be cross-linked using chemical agents, cyclic freeze–thaw processes, and electron beam or γ-irradiation (Asher et al. 2008; Chang et al. 2008). The main disadvantage of PVA hydrogels prepared by irradiation is their poor mechanical strength (Yang et al. 2008). The PVA hydrogels that are cross-linked by cyclic freeze–thaw method exhibit higher mechanical strength than those prepared by irradiation techniques. However, the complex and time-consuming freezing–thawing processes accompany with high energy consumption and the requirement for precision control of the heating and refrigerating rates. Furthermore, the final opaque hydrogels have a very low transparency and a poor long-term stability (Yang et al. 2008). Therefore, it is necessary to explore a more feasible and economic way to produce PVA-based hydrogels with desired properties.

[3] Reprint in part with permission from Cellulose
Han, J., Lei, T., & Wu, Q. 2013. Facile preparation of mouldable polyvinyl alcohol-borax hydrogels reinforced by well-dispersed cellulose nanoparticles: physical, viscoelastic and mechanical properties. *Cellulose*, 1-12.

Borax ($Na_2B_4O_7 \cdot 10H_2O$), known as a non-toxic food additive, has been successfully used as a chemical crosslinking agent for PVA. Addition of a small amount of borax to PVA can lead to a remarkable increase in viscoelasticity of the PVA aqueous solutions. This is attributed to the formation of complexes between borate ions and hydroxyl functional groups of PVA, which act as a temporary cross-linker between PVA molecular chains (Inoue and Osaki 1993). Similar behavior has also been reported for polysaccharide (e.g. between borax and konjac galactomannan) (Gao et al. 2008; Koike et al. 1995). The hydrogels formed by PVA-borax complexation have received much attention because of their attractive physicochemical properties (e.g. inherent water solubility, low toxicity and good biocompatibility) and wide applications, such as easel painting cleaning, artificial cartilage, and drug delivery(Grant et al. 2006; Lin et al. 2005; Manna and Patil 2009). However, most single-phase hydrogels are known to be soft and to have a low strain to failure (Yang et al. 2013a; Yang et al. 2013b). The weak mechanical performance mainly arises from their low resistance to crack propagation and a lack of an efficient energy dissipation mechanism in their polymer network (Yang et al. 2012). Depending on the specific application, designing functional hydrogels requires them to at least possess sufficient mechanical strength, as well as to maintain their intrinsic properties (e.g., low density, water-retaining property, stimuli responsiveness and transparency) if exposed to practical application. The scope of hydrogel applications is often severely hindered by their poor mechanical behavior (Sun et al. 2012). To overcome this limitation, an intense effort is devoted to synthesizing tougher multi-component hydrogels with improved mechanical properties.

In order to enhance the mechanical strength and toughness of hydrogels, composite hydrogels have been prepared by incorporating nanoparticles, including carbon nanotubes, metallic particles, and clay (Shin et al. 2009). Due to their higher specific surface area, smaller

particles afford a better interaction between fillers and polymer matrix, resulting in an enhancement effect in mechanical properties. Compared to most of current nanoparticles, cellulose nanoparticles (CNPs), including cellulose nanocrystals (CNCs) and cellulose nanofibers (CNFs), are more favorable candidates, due to their high ratio of strength to weight, good processability, high water holding capacity, low density, low cost, non-toxicity and high crystallinity (Yang et al. 2013b; Zhang et al. 2011). CNCs and CNFs are isolated from cellulosic microfibrils through acid hydrolysis, where disordered or paracrystalline regions of cellulose are preferentially hydrolyzed over the crystalline regions. Depending on the acid hydrolysis conditions, the long cellulosic microfibrils undergo longitudinal cleavage and become stiff rod-like CNCs or entangled CNFs (Boluk et al. 2012; Yang et al. 2012). CNCs and CNFs with I and II crystalline allomorphs were successfully prepared using alkali pretreatment and/or sulfuric acid hydrolysis in combination with high-pressure homogenization (see TEM images in Fig. 4.1 and Table 1) (Han et al. 2013a). A prerequisite for effective reinforcement of PVA hydrogels using CNCs and CNFs is the uniform dispersion of the CNPs within the PVA aqueous suspension. CNPs do not flocculate and form homogeneous suspension or stable colloid in water because of negatively charged sulfate ester groups introduced onto fibril surfaces during H_2SO_4 hydrolysis (see dispersion photos in Fig. 4.1) (Abitbol et al. 2011). Rod-shaped CNPs can further generate birefringence and ordered liquid phases at sufficiently high concentrations in aqueous mediums due to the liquid crystalline nature and anisotropic alignment of CNC I and CNF I in the aqueous dispersions (Boluk et al. 2012). Similar to PVA, CNPs are hydrophilic and polar in nature. In this regard, they are expected to be well-suited to blend with PVA in aqueous system. On the other hand, high Young's modulus, tensile strength and elastic modulus of 134, 10, and 100 GPa for cellulose crystal region have been reported (Gawryla et al. 2009; Yang et al. 2013a;

Yang et al. 2013b). The combination of high mechanical performance with low density (~1.5 g/cm^3) and high aspect ratio makes CNPs ideal nanofillers for hydrogels. However, a simple incorporation of pristine PVA into CNP suspension cannot lead to a hydrogel with good mechanical properties due to the absence of chemical cross-linker (Zhang et al. 2011). Therefore, Abitbol et al. (2011) lately used cyclic freeze-thaw method to crosslink PVA (15 wt%) and CNPs (1.5-3.0 wt%) at high loading levels to produce composite hydrogels. As mentioned above, this method requires high PVA and cellulose content as well as a series of time-consuming cyclic processes.

In the present study, a method for the reinforcement of PVA hydrogels by incorporating three types of well-dispersed CNPs with the presence of non-toxic borax cross-linker was developed. The objective of this work was to produce high-water-capacity, low density and rubbery hydrogels with enhanced mechanical performance (compared to pure PVA-borax hydrogel) and acceptable optical transmittance. CNPs used in this study could act as the multifunctional crosslinking agent and fillers to physically and chemically bridge the 3D hydrogel network. The UV−vis light transmittance and birefringence behavior of hydrogels were examined to evaluate the hydrogel transparency, the dispersion state of CNPs in PVA-borax aqueous system, the compatibility and interaction among these three components. The effects of particle size, aspect ratio, crystal structure, and crystallinity of different CNPs on the density, water content, optical transmittance and compression property of the hydrogels were investigated. Through compression measurements and dynamic oscillation, the enhancement effect of CNPs on the mechanical properties and viscoelasticity of hydrogels was verified.

4.2 EXPERIMENTAL

4.2.1 Materials

Powdered cellulose, provided by Nippon Paper Chemicals Co., LTD (W-50 grade of KC Flock, Tokyo, Japan) was dried overnight in a vacuum oven at 60 ℃ before use. Three types of CNPs were extracted from powdered cellulose using alkali pretreatment and/or sulfuric acid hydrolysis in combination with a high-pressure homogenization (HPH) as described in our previous work (Han et al. 2013a; Han et al. 2013b). The CNCs with I and II crystalline allomorphs as well as the cellulose I nanofibers were designated as CNC I, CNC II and CNF I, respectively, and they were collectively referred to as CNPs. Their corresponding preparation conditions and relevant dimensions are summarized in Table 4.1.

Table 4.1 Preparation conditions and relevant dimensions of CNPs.

Parameters[a]	Sample		
	CNC I	CNF I	CNC II
Preparation conditions	64 % H_2SO_4+HPH	48 % H_2SO_4+HPH	20 % NaOH+ 64 % H_2SO_4+HPH
Length (nm)	149 ±40	732 ±208	46 ±18
Width (nm)	9 ±2	21 ±7	5 ±1
Aspect ratio	16.6	36.6	9.4
Crystallinity (%)	66.4	57.6	73.6

[a] Determined from our previous study (Han et al. 2013a).

The obtained aqueous suspensions of CNPs (1.0 wt%) were sealed in glass containers and stored at 5^{o}C in a refrigerator before testing. Poly (vinyl alcohol) (PVA) (M_w=146.000-186.000 g mol^{-1}, 99.0+% hydrolyzed) was purchased from Aldrich Chemical Co. (St. Louis, MO, USA) and used as received. Borax (sodium tetraborate decahydrate, over 99.5% purity, $Na_2B_4O_7 \cdot 10H_2O$, M_w=381.37 g mol^{-1}) was obtained from Aldrich Chemical Co. and dried at 120^{o} under vacuum for 12h before sample preparation. Sulfuric acid (95–98 wt%, VMR, West

Chester, PA, USA) was of analytical grade and was diluted to concentrations of 64 and 48 wt%. Sodium hydroxide (NaOH over 97.0% purity, ACS, MS, USA) was dissolved in distilled water to prepare a 20 wt% aqueous solution. All reagents and solvents used were of analytical grade. Deionized water was used in the preparation of all solutions.

4.2.2 Preparation of PVA-borax-water Solution and CNP-PVA-borax Hydrogels

Cellulose-PVA-borax hydrogels with 2.0 wt% of PVA, 0.4 wt% of borax and 1.0 wt% of CNPs were prepared as follows (Figure 4.1). 0.1 g of borax powder was dissolved in 1.0 wt% CNP aqueous suspensions with continuous stirring at 25^{o}C for 20 min. Subsequently, 0.5 g of PVA powder was then slowly sprinkled onto the surface of the stirred aqueous solutions. To avoid the formation of PVA lumps, the solutions were mechanically stirred for 30 min at room temperature. After a complete swelling of PVA powder, the solutions were heated to 90^{o}C and stirred for 2 h. To prevent the evaporation of water and film formation on the surface of the mixture, the heating process was conducted in hermetically sealed vials. As the temperature rose, the PVA powder began to dissolve and the mixture gradually became homogeneous and viscous. After the PVA was completely dissolved, homogeneous translucent solutions with well-dispersed CNPs were formed. In order to remove the bubbles, the solutions were placed in an ultrasonic water bath at 35^{o}C for 10 min. As the temperature decreased, the solutions started to present viscoelastic properties. The solutions were further cooled slowly to room temperature to form the final hydrogels. The PVA-borax-water complex solution with a PVA concentration of 3.0 wt% and a borax concentration of 0.4 wt% (designated as PB) was prepared by directly dissolving PVA powder into borax aqueous solutions. All other processing conditions were the same as those used for the cellulose-PVA-borax hydrogels. Overall, all the composite hydrogel samples contain 2.0 wt% of PVA and 0.4 wt% of borax. The hydrogels with 1.0 wt% of CNC I, CNF I

and CNC II were designated as PB-CNC I, PB-CNF I and PB-CNC II, respectively, and they were collectively referred to as CNP-reinforced PB hydrogels. For comparison, a series of reference variant hydrogels that are composed of only 2.0 wt% PVA and 1.0 wt% CNPs (without borax) were designated as P-CNC I, P-CNC II and P-CNF I, respectively, and they were collectively referred to as CNP-reinforced PVA hydrogels.

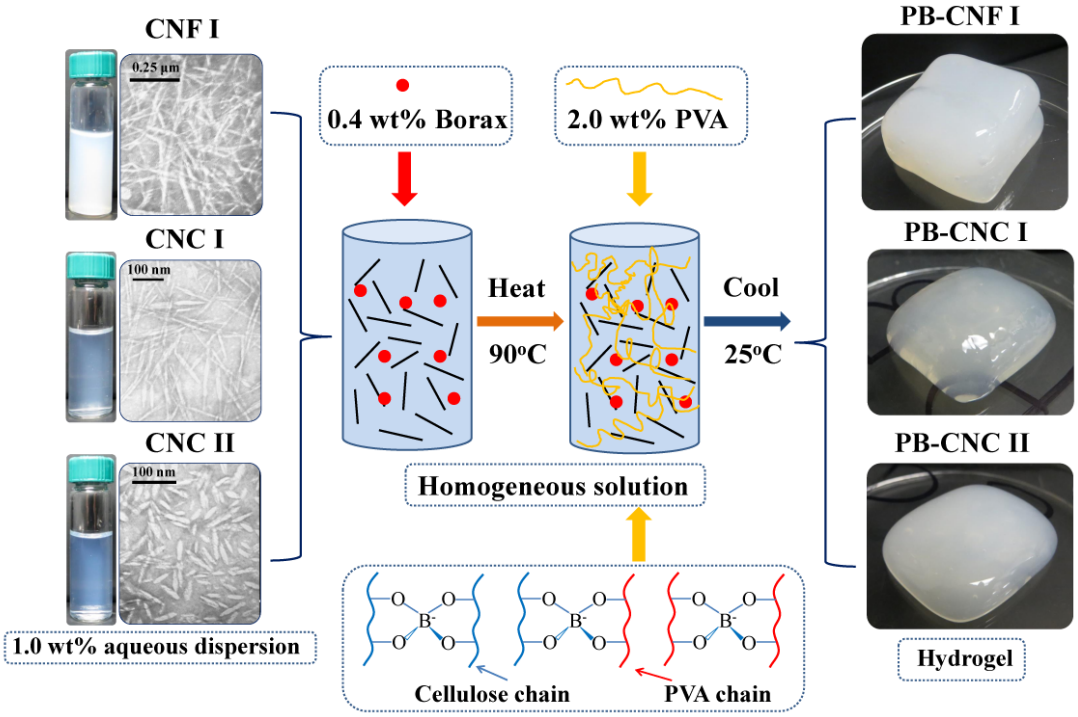

Figure 4.1 Schematic illustration of the preparation and synthesis process of the hydrogels.

4.2.3 Density and Water Content of Hydrogels

The densities (ρ, g/cm^3) of the hydrogels were determined from the dimensions and weights of the samples. Each sample (initial weight = W_h) was dried in a vacuum oven at 50 ℃ until a constant weight (W_d) was reached. The water contents (W_c) of the hydrogels were calculated from eq. 4.1:

$$W_c = \frac{W_h - W_d}{W_h} \times 100\% \qquad (4.1)$$

4.2.4 Optical Transmittance

The hydrogel samples were introduced into a UV quartz cuvette with PTFE cover (dimension of 45 ×12.5 × 12.5-mm, and layer thickness of 10 mm). The optical transmittance of each sample was measured at wavelength from 300 to 800 nm using a UV-Vis spectrophotometer (Evolution 600 PC, Thermo Electron Corp., USA). The data were collected at a scan speed of 240 nm min^{-1} and a band width of 2 nm using deionized water as a reference. All tests were carried out at room temperature. The mean transmittance of each sample was calculated by averaging the transmittances over the whole wavelength range. All the 1.0 wt% CNP dispersions were prepared by a 2 h stirring after preparation, and photographs were taken after 48 h.

4.2.5 Polarized Light Microscopy Observations

The hydrogels were transferred into a paired slide glass cell with a 0.5 mm thick spacer and observed using an Olympus BH-2 polarization light microscope (Olympus Optical Co., LTD, Tokyo, Japan) equipped with a 530-nm retardation plate at room temperature. After loading, each sample was allowed to equilibrate for 2h at 30^{o}C for complete recovery of hydrogel structure. The texture of the liquid crystal phase was examined between a pair of crossed polarizers and the pictures were taken with a digital camera.

4.2.6 Dynamic Oscillation Measurements

The dynamic rheological behaviors of hydrogels were investigated with an AR2000EX controlled-stress Rheometer (TA Instruments Inc., New Castle, DE) using plate-and-plate geometry (diameter: 40 mm, gap: 500 μm). The viscoelastic parameters (log mode), including shear storage modulus (G′) and complex viscosity (η*) as functions of angular frequency (ω) were measured over the ω range of 0.1-100 rad/s at 25^{o}C. A strain (γ) of 1.0% was selected in the

oscillation tests to ensure that the dynamic oscillatory deformation of each sample was within the linear viscoelastic region. For steady state flow test, steady shear viscosity (η) as a function of shear rate (γ) was measured over the γ range of 0.1-100 s^{-1} at 25 ℃ using cone-and-plate geometry (diameter: 40 mm, cone angle: 1°59′42″, truncation: 56 μm). To avoid water evaporation, the gap between two plates was sealed with a solvent trap cover and silicon oil.

4.2.7 Compression Strength Test of Hydrogels

Uniaxial compression stress–strain measurements were performed with an AR2000ex Rheometer (TA Instruments Inc., New Castle, DE, USA) using cylindrical hydrogel samples (20mm in diameter and 5mm in height). Because of the slightly uneven top surfaces, a preload of approximately 0.05 N was vertically applied to the cylindrical hydrogel samples before compression testing (Kohnke et al. 2012). Each sample was compressed in the direction parallel to the cylinder axis by an upper moveable plate (40mm diameter) against a stationary peltier plate at a cross-head speed of 20 μm/s at 25 ^{o}C in air. The compression for all samples ended when the normal force reached the maximum loading capacity (50 N). Compression stress (σ) and strain (ε) values were calculated from measured force and specimen displacement based on the initial dimensions of hydrogels. The compression results were averaged over three specimens per group.

4.3 RESULTS AND DISCUSSION

4.3.1 UV Optical Transmittance and Dispersion State of Hydrogels

Figure 4.2a shows UV−vis light transmittance spectra of PB, PB-CNC I, PB-CNF I and PB-CNC II at a visible wavelength range of 300 to 800 nm. The pure PVA-borax-water system was almost transparent with a mean light transmittance of 80.2%. However, PB hydrogel was not as stiff as PB-CNP hydrogel as determined by compression and rheology measurements. The

refractive index of cellulose (1.54) is greater than that of PVA (1.51). Therefore, after the incorporation of CNPs, the transmittance values of CNP-reinforced hydrogels decreased to different extents, but they remained translucent due to their high water content ($W_C \approx 96\%$, Table 4.2) and the homogeneous network structure. The CNPs were well-dispersed in PVA-borax-water system without any visible aggregation, suggesting an excellent compatibility of cellulose fillers with polymer matrix and thus a homogeneous dispersion state of translucent hydrogels. Homogeneous dispersion of CNPs in the PVA-borax-water system was a key for achieving their reinforcement effect. Dispersion containing 1.0 wt% CNC I or CNF I formed stable colloids due to their liquid crystalline property and the mutually repulsive negative electrostatic charge caused by -O-SO_3- groups on their surfaces, while CNC II formed homogeneous aqueous suspension. Dissolving PVA and borax in CNP dispersions assured the interpenetration, tangling and crosslinking of PVA chains and borax molecules with the CNPs, leading to a three-dimensional network structure. For all the hydrogel samples, the absorption band around 330 nm was probably due to the presence of carbonyl functional groups in hydrogels (Jayasekara et al. 2004).

The transparency for hydrogels was in the order of PB-CNC II > PB-CNC I > PB-CNF I, which was in accordance with the transparency trend of 1.0 wt% aqueous suspension of CNPs (Figure 4.2b). This phenomenon was further confirmed by Figure 4.2c where the visibility of the black regions observed through these cellulose dispersions also followed the same order of CNC II > CNC I > CNF I. The visible light transmittance of CNP-reinforced PB hydrogels largely depended on particle size and the dispersion quality of particles in the polymer system. The mean length of CNF I (~732 nm) was nearly five times longer than that of CNC I (~149 nm; Table 4.1). When the hydrogels were exposed to visible light, the light scattering on the cellulose surface

might theoretically happen if the particle size is larger than 400 nm, leading to a loss of light transmittance (Han et al. 2013a).

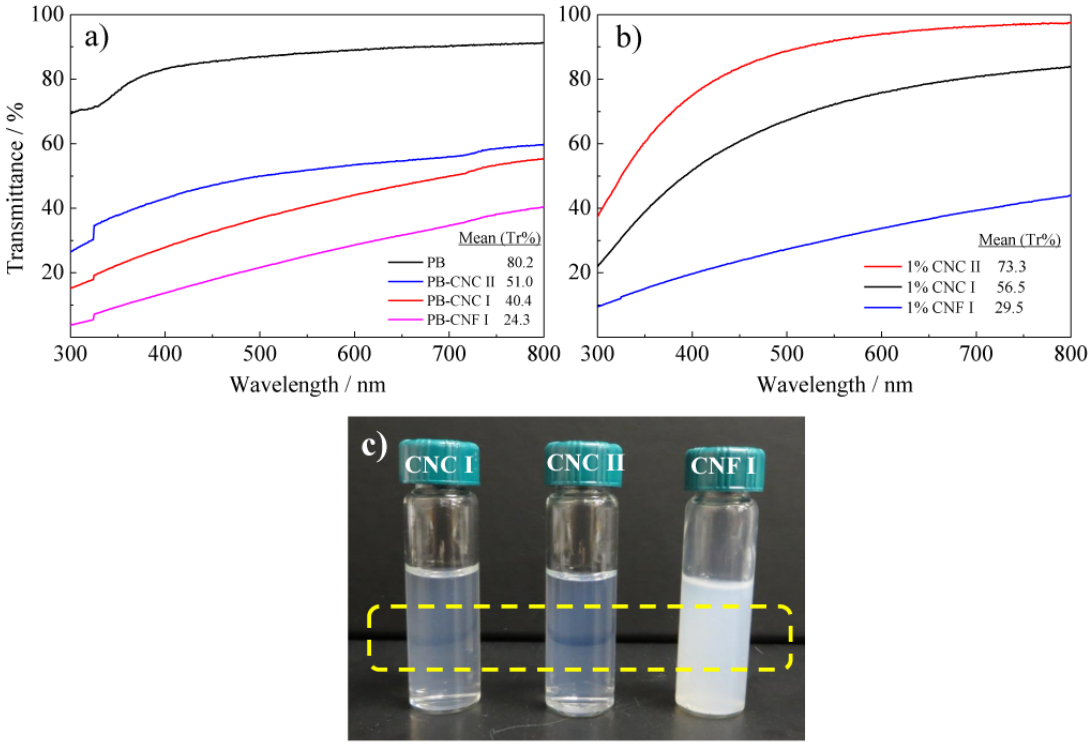

Figure 4.2 UV−vis transmittance spectra of hydrogels (a) and 1.0 wt% aqueous suspension of cellulose nanoparticles (b); 1.0 wt% aqueous suspension of cellulose nanoparticles (c).

In addition, the high aspect ratio of CNF I (~36.6) promoted the entanglement of polymeric chains and increased the probability that PVA chains and borate ions contacted with the surface of each single CNP (Table 1). Consequently, numerous physical junctions formed via polymer chain tangling established a compacter structure of PB-CNF I, resulting in a translucent, however, much stronger hydrogel as determined by compression tests. On the other hand, the aspect ratio (~9.4) and length (~46 nm) of CNC II were smallest among the three types of CNPs (Table 4.1). If the particle size is less than one tenth of the visible light wavelength, the light scattering is effectively restrained despite of the difference in the refractive index of cellulose and PVA (Yano et al. 2005). Therefore, PB-CNC II achieved the best transparency because of

nanoeffect, however, moderate mechanical strength due to a relative lack of chain entanglement within hydrogel.

4.3.2 Birefringence Behavior and Well-Dispersed Cellulose Nanoparticles in PB-CNC I and PB-CNC I Hydrogels by Polarized Light Microscopy

After cooled down to room temperature, CNP-PVA-borax aqueous dispersions gradually lost their fluidity and formed freestanding hydrogels. These translucent hydrogels had a rubbery consistency and possessed a relatively high rigidness enabling them to be picked up and easily handled, whereas the pure PB hydrogel was not as rigid as them.

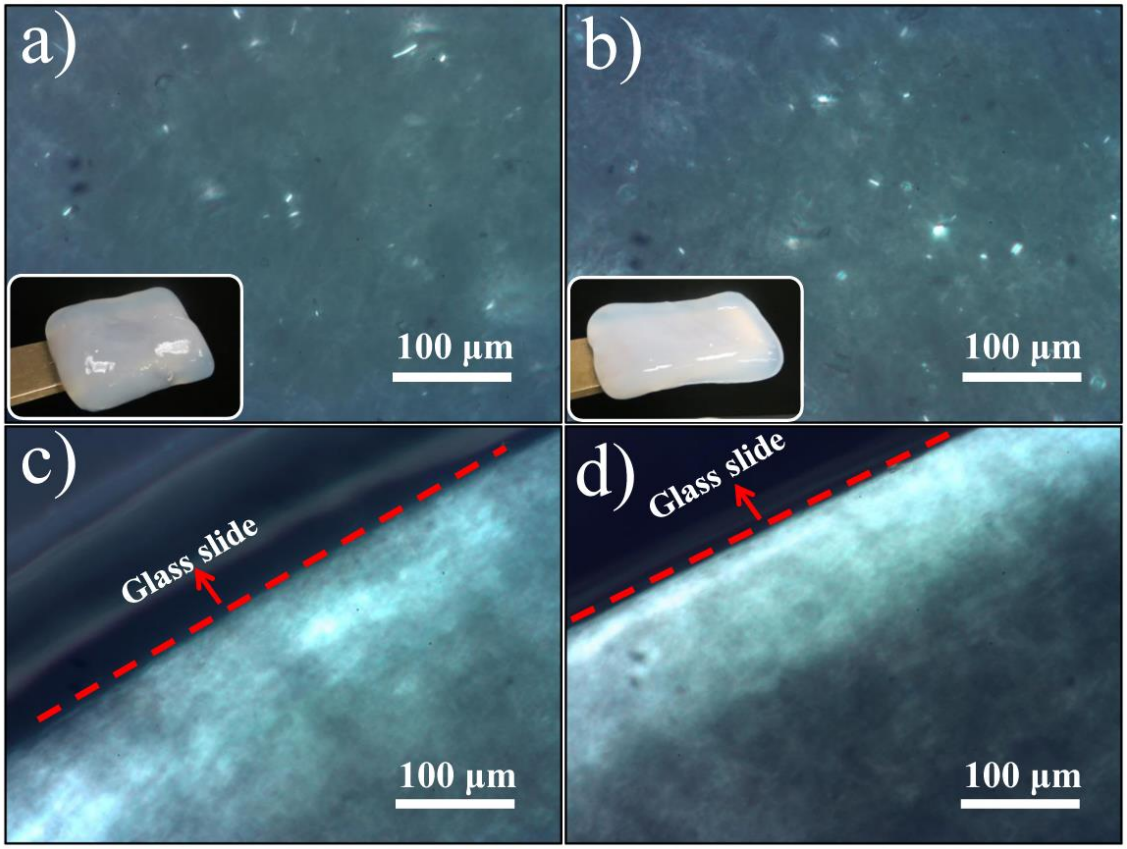

Figure 4.3 Polarized optical micrographs of PB-CNC I (a, c) and PB-CNF I (b, d) viewed through crossed polarizers showing the distinct macroscopic birefringence texture, especially the iridescent pattern on the sample edge (c, d). The insets were their appearances.

It is well-known that because of the mutually repulsive negative charge of sulfate ester groups on their surfaces, the rigid rod-like cellulose I nanoparticles have a strong tendency to

align along a vector director in water, creating a birefringent pattern that can be observed under polarized light microscopy (Lima and Borsali 2004). Interestingly, with the addition of 2.0 wt% PVA and 0.4 wt% borax into CNP dispersions, PB-CNC I and PB-CNF I both still exhibited birefringence behavior and liquid crystalline morphology when observed between crossed polarizers (Figure 4.3c, d), indicating that the anisotropic alignment of CNC I and CNF I in the aqueous dispersions was preserved in the stiff hydrogels. It was clearly seen that CNC I and CNF I were well-dispersed in hydrogels (Figure 4.3a, b), which was in an agreement with the results of optical transmittance measurements. Therefore, the presence of PVA and borax not only maintained the homogeneous dispersion state of CNPs, but gave rise to the formation of 3D network structure within hydrogels as well, thus providing strength and elasticity for hydrogels (confirmed by the following compression tests). On the other hand, the PB and PB-CNC II remained isotropic without any obvious signs of birefringence behavior.

4.3.3 Dynamic Viscoelasticity of Hydrogels

To understand the influence of various CNPs and borax on the viscoelastic properties of hydrogels, oscillatory measurements were carried out at 25^{o}C. The G′ (elasticity) and η* (complex viscosity) as a function of angular frequency (ω) for hydrogels within linear deformation range are illustrated in Fig. 4.4 a and b. For all the CNP-reinforced PB hydrogels, as ω proceeded, the G′ gradually increased to reach a plateau region (high-frequency plateau, G'_p), indicating the polymer entanglements and the gelation character of CNPs (Lin et al. 2005). The G'_p values of PB-CNF I, PB-CNC I, PB-CNC II, and PB were 2354, 650, 230, and 122 Pa, respectively. With the addition of 1.0 wt% CNF I, an increase of almost 19-fold in G'_p was generated for PB-CNF I compared with pure PB hydrogel, suggesting the crosslinking role and enhancement effect of CNF I. On the other hand, the G′ and η* of PB-CNF I were much higher

than those of P-CNF I at each ω (Fig. 4.4a,b), respectively, indicating an important role of borax in the 3D network structure. Figure 4.4c shows the viscosity (η) of all hydrogel samples as a function of shear rate (γ). Without borax, CNP-reinforced PVA hydrogels exhibited a typical shear-thinning behavior through the whole γ range. After 0.4 wt% of borax was added into the system, the η values of all hydrogels were significantly increased. On the other hand, the incorporation of 1.0 wt% CNPs also significantly increased the η values of pure PB system. Overall, the viscoelasticity of these hydrogels followed the order of PB-CNF I > PB-CNC I > PB-CNC II > PB > CNP-reinforced PVA hydrogels.

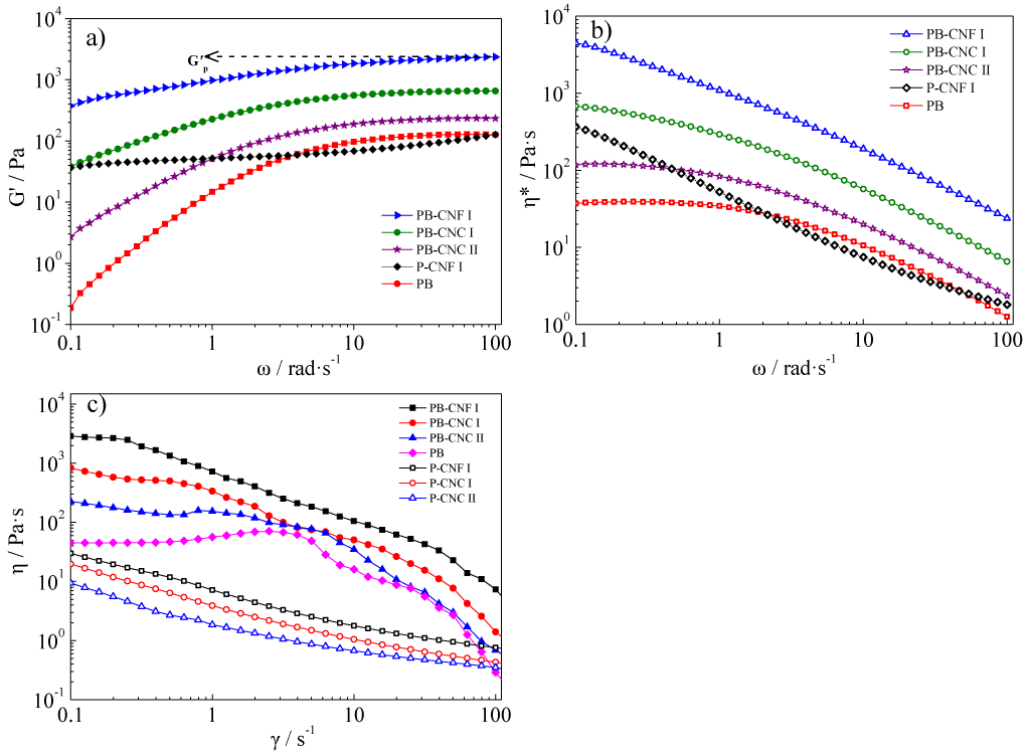

Figure 4.4 Dynamic viscoelasticity performance of hydrogels at 25 °C: (a) angular frequency (ω) dependence of shear storage modulus (G′), (b) ω dependence of complex viscosity (η*), and (c) steady shear viscosity (η) versus shear rate (γ).

4.3.4 Uniaxial Compression Stress–Strain Behavior of Hydrogels

The preparation of high-performance CNP-reinforced hydrogels requires the control of the nature of cellulose nanofillers and interactions between fillers and polymer matrix (Das et al.

2012; Yang et al. 2013b). The response of hydrogels towards compressive stress plays an important role for many hydrogel applications, thus evaluation of mechanical properties of the hydrogels was focused on their compression properties. A series of compression measurements were performed on PB, PB-CNC I, PB-CNC II and PB-CNF I hydrogels to examine the degree of mechanical enhancement led by the incorporation of various CNPs into the PVA-borax-water system. The energy absorption by each sample under uniaxial compression was defined as the area below the stress–strain curve (Cervin et al. 2013). All hydrogels presented a gradual transition from linear to non-linear stress–strain behavior without obvious horizontal plateau, making it challenging to determine the yield point. Consequently, the mechanical properties were additionally compared by the compressive stress at the 70% strain level and the energy absorption at the 90% strain level. To further characterize the stiffness of hydrogels, the compressive elastic modulus (E_e) was determined from the slopes of the linear portions ($\varepsilon < 20\%$) of the stress–strain curves (Gawryla et al. 2009).

The compression stress–strain curves and the corresponding energy absorption-strain curves are shown in Figure 4.5a, b, respectively. The trend in compressive parameters (energy absorption and σ at a certain ε level, E_e determined from initial linear portions) was as follows, PB-CNF I > PB-CNC I > PB-CNC II > PB. As expected, the addition of a small amount (1.0 wt%) of CNPs significantly increased the compressive strength of PB hydrogel (Figure 4.5a). Specifically, the σ of PB-CNF I, PB-CNC I and PB-CNC II at ε=70% were almost 21, 9 and 6-fold higher than that of PB (Table 4.2), respectively. This phenomenon indicated that, compared with other nanofillers, such as carbon nanotube and nanoclay (Wu et al. 2009), well-dispersed CNPs in PVA matrix have a similar reinforcing effect on the composite hydrogel. The mechanical reinforcement of CNP-filled hydrogels is largely affected by cross-linking next to a

result of some combined effects, such as the dimension, concentration and dispersion of fillers, as well as the interactions between fillers and polymer matrix.

As demonstrated by the results of UV-vis and polarized light microscopy measurements, CNPs were well-dispersed in PVA-borax aqueous system without formation of visible aggregates, which helped transfer the compressive stress from polymer chains to CNPs and restrain the growing of microcracks (Zhou and Wu 2011). Because the overlap concentration of PVA (C*) is 1.54 wt% at ambient temperatures, the higher concentration of PVA (2.0 wt%) is chosen to achieve the entanglements of PVA chains, which is essential for formation of the 3D-networks that immobilize the liquid phase (Carretti et al. 2010; Chen and Yu 1997). The CNP concentration in each hydrogel (1.0 wt%) is just above the dilute concentration range where particles barely contacted with each other (Boluk et al. 2012). On one hand, CNPs carry numerous hydroxyl groups on their surfaces and thus formed plenty of hydrogen bonds with PVA-borax matrix, resulting in the chain entanglement and the formation of physically crosslinked hydrogel network (Wang and Chen 2011). On the other hand, borax ($Na_2B_4O_7 \cdot 10H_2O$) dissociated completely into equal quantities of trigonal planar [$B(OH)_3$] (boric acid) and tetrahedral [$B(OH)_4^-$] (monoborate ions) that interchanged rapidly when dissolved in water. The $B(OH)_4^-$ ion was shaped like a tetrahedron (four sides, each side is an equilateral triangle) with the boron in the center and the four OH groups at each corner. [$B(OH)_4^-$] could form complexes with PVA chains and/or CNPs (Gao et al. 2008; Gouvea et al. 2009). In this case, borax acts as an ionic cross-linker between the CNPs and PVA chains, leading to strong interactions between them as well as chemically crosslinked hydrogel network. In addition, by incorporating CNPs, all the composite hydrogels exhibited increased compressive E_e as compared with that of the neat PB. Considering the highly crystalline nature of rigid CNPs, our

previous study confirmed that the crystallinities of CNC I, CNF I and CNC II were 66.4, 57.6 and 73.6% (Table 4.1) (Han et al. 2013a), respectively, which were higher than that of PVA (30-50%) (Peresin et al. 2010). Therefore, it was not surprising to observe a hardening effect after CNPs were incorporated into a softer chain PVA matrix with a lower degree of crystallinity. Due to the direct proportionality relationship between E_e and crosslink density (Wang and Chen 2011), the increased E_e leads to an increase in crosslink density. This phenomenon was advantageous for CNPs to form the load-bearing percolating networks within the host polymer matrix (Yang et al. 2013b). By homogeneous distribution of CNPs within the polymer matrix, the chemical and physical cross-links coexisted in the complex network, leading to the significant increase in the mechanical properties of CNP-reinforced hydrogels (Yang et al. 2013b). Consequently, CNPs in this study acted as multifunctional crosslinking agent and fillers to bridge the hydrogel network.

Table 4.2 Physical and compression properties of hydrogels

hydrogels	M_C (%)	ρ (g/cm^3)	σ (KPa) at ε=70%	energy absorption (J/m^3) at ε=90%	E_e (KPa)
PB-CNF I	95.6 ± 0.13	1.14 ± 0.11	7.36 ± 0.16	489.6 ± 10.3	22.5 ± 0.6
PB-CNC I	96.1 ± 0.24	1.11 ± 0.08	2.99 ± 0.04	201.9 ± 8.0	4.8 ± 0.4
PB-CNC II	96.3 ± 0.18	1.08 ± 0.07	1.95 ± 0.06	162.5 ± 4.9	3.8 ± 0.2
PB	97.1 ± 0.22	1.09 ± 0.10	0.40 ± 0.05	48.1 ± 2.5	0.9 ± 0.1

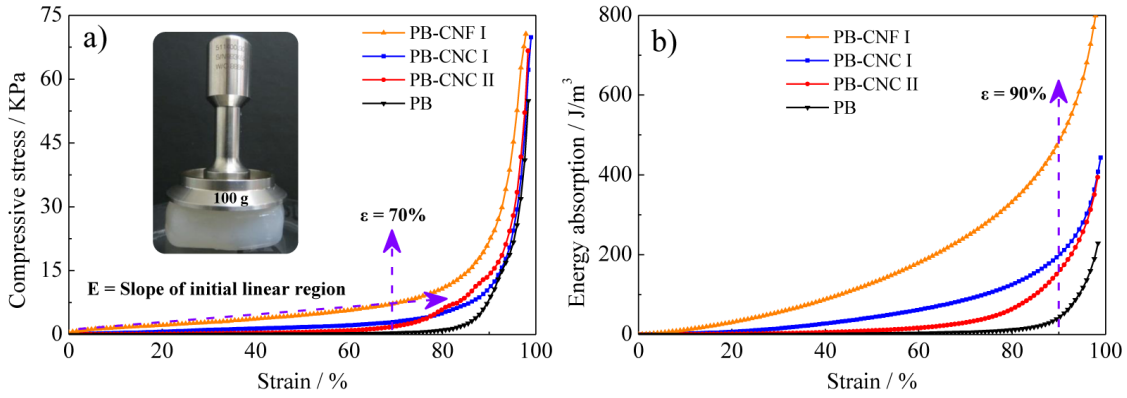

Figure 4.5 Compression stress–strain curves (a) and energy absorption- strain curves (b) of hydrogels; Rigid PB-CNF I hydrogel loaded with 100g weight (c).

Not surprisingly, it was observed that among all hydrogels, rubbery-like PB-CNF I showed the highest σ and energy absorption throughout the whole ε range, especially at high ε levels. Its E_e is one order of magnitude greater than those of PB-CNC I and PB CNC II, indicating that PB-CNF I was the stiffest and strongest hydrogel. As shown in the insert of Figure 4.4a, the free-standing PB-CNF I did not display any distortion under a static loading of ~100 g (supporting more than 10 times of its own weight), exhibiting a high strength and the potential applications (Chang et al. 2008). The improved hydrogel strength was mainly attributed to the larger particle size and aspect ratio as well as ease of tangling with PVA chains (Zhang et al. 2011). The hydrogel PB-CNF I ($W_C \approx 96\%$) prepared in this work exhibited higher compression strength (σ ≈ 70.6 KPa at ε= 95%) than that of polyacrylamide-chitosan nanofiber hydrogel (σ ≈ 50.2 KPa at ε = 95%) with a lower water content ($W_C \approx 90\%$) prepared via in situ free-radical polymerization (Zhou and Wu 2011). Moreover, the compressive modulus of PB-CNF I (~22.5 KPa) was 4 times greater than that of oxidized xylan–cellulose nanocrystal hydrogel (~5.4 KPa) (Köhnke et al.). More importantly, at ε = 25%, the obtained hydrogels were comparable in compressive strength (σ ≈ 2.6 KPa with 1.0 wt% of CNF I and 2.0 wt% of PVA) to those CNP-reinforced PVA hydrogels (σ ≈ 1.5 KPa with 3.0 wt% of CNC and 15 wt% of PVA)

prepared by cyclic freeze–thaw processes (Abitbol et al. 2011). Additionally, the dosage of PVA (2.0 wt%) and CNPs (1.0 wt%) used for the present method were lower than that of cyclic freeze–thaw prepared hydrogels (PVA=15.0 wt%, CNPs=1.5-3.0 wt%) (Abitbol et al. 2011). Thus, these low density hydrogels ($\rho \approx 1.1$ g/cm^3, Table 4.2) prepared using less raw polymers through a simpler method had a potential to be used as biomedical materials (Wang and Chen 2011).

It was also noticed that the energy absorption of PB-CNC I (~201.9 J/m^3) was lower than that of PB-CNF I (~489.6 J/m^3) at 90% strain level (Table 4.2), indicating that CNF I was more effective on increasing the mechanical strength than CNC I. The difference of enhancement effect was mainly due to the larger size and aspect ratio of CNF I than CNC I. Accordingly, smaller-sized PB-CNC II absorbed less energy (~162.5 J/m^3) than PB-CNC I at the 90% strain level. Additionally, it was reported that the elastic modulus of the crystalline regions of cellulose I (138.0 GPa) was larger than that of cellulose II (88.0 GPa) in the direction parallel to the chain axis (Nishino et al. 1995), which promoted cellulose I reinforced hydrogels to absorb more energy under stress than cellulose II reinforced hydrogels. Therefore, PB-CNF I and PB-CNC I systems were both tougher and stiffer than PB-CNC II under compression.

4.4 CONCLUSIONS

CNP-reinforced PVA-borax hydrogels were successfully produced through a facile synthesis in an aqueous medium. By respectively incorporating three kinds of well-dispersed CNPs (i.e., CNC I, CNC II and CNF I) to PB aqueous system, the compressive strength and viscoelasticity of the hybrid hydrogels were pronouncedly increased, clearly demonstrating the synergy between natural CNPs and synthetic polymer matrix. Highly-crystalline CNPs acted as multifunctional crosslinking agent and fillers for physically and chemically bridging the 3D

network structure within PB system, resulting in low-density (~1.1g/cm^3), translucent and stiff hydrogels. The mechanical property of the hydrogels were in the order of PB-CNF I > PB-CNC I >PB-CNC II> PB, while their transparency was sequenced in a reverse order. PB-CNF I is the strongest hydrogel (σ at ε=70% was 21 times higher than the neat PB) due to the entanglement of longer chains, while PB-CNC II achieved the best transparency (mean transparency =51.0%) because of nanoeffect. These polymeric hydrogel materials are readily processed, and their preparation simplicity, availability from inexpensive renewable resources and performance tenability (e.g., through adjusting CNPs) are distinguishing features for many potential water-based applications (Appel et al. 2012). Being distinguished by high water content and diverse potential physical properties, they can be engineered to resemble the extracellular environment of the human body's tissues in ways that enable their application in biosensors, medical implants, and even drug-delivery devices (Seliktar 2012).

Since the dynamic bonds formed between the $B(OH)_4^-$ and the OH groups on the sides of the PVA (and/or CNPs) are reversible and exchangeable, the self-healing ability and thermo-reversibility of as-prepared composite hydrogels were expected. Therefore, our further work is to characterize the dynamic rheological behavior of obtained hydrogels, and to explore the plausible mechanism for the multi-complexation among CNPs, PVA and borax for a better understanding of the relationship between 3D network structure and hydrogel properties.

4.5 REFERENCES

Abitbol T., Johnstone T., Quinn T. M. and Gray D. G. 2011. Reinforcement with cellulose nanocrystals of poly(vinyl alcohol) hydrogels prepared by cyclic freezing and thawing. *Soft Matter* 7:2373-2379.

Appel E. A., Loh X. J., Jones S. T., Biedermann F., Dreiss C. A. and Scherman O. A. 2012. Ultrahigh-Water-Content Supramolecular Hydrogels Exhibiting Multistimuli Responsiveness. *Journal of the American Chemical Society* 134:11767-11773.

Asher S. A., Kimble K. W. and Walker J. P. 2008. Enabling Thermoreversible Physically Cross-Linked Polymerized Colloidal Array Photonic Crystals. *Chemistry of Materials* 20:7501-7509.

Boluk Y., Zhao L. Y. and Incani V. 2012. Dispersions of Nanocrystalline Cellulose in Aqueous Polymer Solutions: Structure Formation of Colloidal Rods. *Langmuir* 28:6114-6123.

Carretti E., Natali I., Matarrese C., Bracco P., Weiss R. G., Baglioni P., Salvini A. and Dei L. 2010. A new family of high viscosity polymeric dispersions for cleaning easel paintings. *Journal of Cultural Heritage* 11:373-380.

Cervin N. T., Andersson L., Ng J. B. S., Olin P., Bergstrom L. and Wagberg L. 2013. Lightweight and Strong Cellulose Materials Made from Aqueous Foams Stabilized by Nanofibrillated Cellulose. *Biomacromolecules* 14:503-511.

Chang C. Y., Lue A. and Zhang L. 2008. Effects of crosslinking methods on structure and properties of cellulose/PVA hydrogels. *Macromolecular Chemistry and Physics* 209:1266-1273.

Chen C. Y. and Yu T.-L. 1997. Dynamic light scattering of poly(vinyl alcohol)-borax aqueous solution near overlap concentration. *Polymer* 38:2019-2025.

Das D., Kar T. and Das P. K. 2012. Gel-nanocomposites: materials with promising applications. *Soft Matter* 8:2348-2365.

Gao S. J., Guo J. M. and Nishinari K. 2008. Thermoreversible konjac glucomannan gel crosslinked by borax. *Carbohydrate Polymers* 72:315-325.

Gawryla M. D., van den Berg O., Weder C. and Schiraldi D. A. 2009. Clay aerogel/cellulose whisker nanocomposites: a nanoscale wattle and daub. *Journal of Materials Chemistry* 19:2118-2124.

Gouvea M. R., Ribeiro C., de Souza C. F., Marvila-Oliveira I., Lucyszyn N. and Sierakowski M. R. 2009. Rheological behavior of borate complex and polysaccharides. *Materials Science & Engineering C-Biomimetic and Supramolecular Systems* 29:607-612.

Han J., Zhou C., Wu Y., Liu F. and Wu Q. 2013a. Self-Assembling Behavior of Cellulose Nanoparticles during Freeze-Drying: Effect of Suspension Concentration, Particle Size, Crystal Structure, and Surface Charge. *Biomacromolecules* 14:1529-1540.

Han J. Q., Zhou C. J., Wu Y. Q., Liu F. Y. and Wu Q. L. 2013b. Self-Assembling Behavior of Cellulose Nanoparticles during Freeze-Drying: Effect of Suspension Concentration, Particle Size, Crystal Structure, and Surface Charge. *Biomacromolecules* 14:1529-1540.

Inoue T. and Osaki K. 1993. Rheological Properties of Poly(Vinyl Alcohol)/Sodium Borate Aqueous-Solutions. *Rheologica Acta* 32:550-555.

Jayasekara R., Harding I., Bowater I., Christie G. B. Y. and Lonergan G. T. 2004. Preparation, surface modification and characterisation of solution cast starch PVA blended films. *Polymer Testing* 23:17-27.

Köhnke T., Elder T., Theliander H. and Ragauskas A. J. Ice templated and cross-linked xylan/nanocrystalline cellulose hydrogels. *Carbohydrate Polymers*.

Kobayashi M., Chang Y. S. and Oka M. 2005. A two year in vivo study of polyvinyl alcohol-hydrogel (PVA-H) artificial meniscus. *Biomaterials* 26:3243-3248.

Kohnke T., Lin A., Elder T., Theliander H. and Ragauskas A. J. 2012. Nanoreinforced xylan-cellulose composite foams by freeze-casting. *Green Chemistry* 14:1864-1869.

Koike A., Nemoto N., Inoue T. and Osaki K. 1995. Dynamic Light-Scattering and Dynamic Viscoelasticity of Poly(Vinyl Alcohol) in Aqueous Borax Solutions .1. Concentration-Effect. *Macromolecules* 28:2339-2344.

Lima M. M. D. and Borsali R. 2004. Rodlike cellulose microcrystals: Structure, properties, and applications. *Macromolecular Rapid Communications* 25:771-787.

Lin H. L., Liu Y. F., Yu T. L., Liu W. H. and Rwei S. P. 2005. Light scattering and viscoelasticity study of poly(vinyl alcohol)-borax aqueous solutions and gels. *Polymer* 46:5541-5549.

Lin H. L., Yu T. L. and Cheng C. H. 2000. Reentrant behavior of poly(vinyl alcohol)-borax semidilute aqueous solutions. *Colloid and Polymer Science* 278:187-194.

Nishino T., Takano K. and Nakamae K. 1995. Elastic-Modulus of the Crystalline Regions of Cellulose Polymorphs. *Journal of Polymer Science Part B-Polymer Physics* 33:1647-1651.

Peresin M. S., Habibi Y., Zoppe J. O., Pawlak J. J. and Rojas O. J. 2010. Nanofiber Composites of Polyvinyl Alcohol and Cellulose Nanocrystals: Manufacture and Characterization. *Biomacromolecules* 11:674-681.

Ramaraj B. 2007. Crosslinked poly(vinyl alcohol) and starch composite films. II. Physicomechanical, thermal properties and swelling studies. *Journal of Applied Polymer Science* 103:909-916.

Seliktar D. 2012. Designing Cell-Compatible Hydrogels for Biomedical Applications. *Science* 336:1124-1128.

Shin M. K., Spinks G. M., Shin S. R., Kim S. I. and Kim S. J. 2009. Nanocomposite Hydrogel with High Toughness for Bioactuators. *Advanced Materials* 21:1712-+.

Sun J. Y., Zhao X. H., Illeperuma W. R. K., Chaudhuri O., Oh K. H., Mooney D. J., Vlassak J. J. and Suo Z. G. 2012. Highly stretchable and tough hydrogels. *Nature* 489:133-136.

VI L., Galaev I. Y., Plieva F. M., Savinal I. N., Jungvid H. and Mattiasson B. 2003. Polymeric cryogels as promising materials of biotechnological interest. *Trends in Biotechnology* 21:445-451.

Wang Y. X. and Chen L. Y. 2011. Impacts of nanowhisker on formation kinetics and properties of all-cellulose composite gels. *Carbohydrate Polymers* 83:1937-1946.

Wu Y. T., Zhou Z., Fan Q. Q., Chen L. and Zhu M. F. 2009. Facile in-situ fabrication of novel organic nanoparticle hydrogels with excellent mechanical properties. *Journal of Materials Chemistry* 19:7340-7346.

Yang J., Han C. R., Duan J. F., Ma M. G., Zhang X. M., Xu F. and Sun R. C. 2013a. Synthesis and characterization of mechanically flexible and tough cellulose nanocrystals-polyacrylamide nanocomposite hydrogels. *Cellulose* 20:227-237.

Yang J., Han C. R., Duan J. F., Ma M. G., Zhang X. M., Xu F., Sun R. C. and Xie X. M. 2012. Studies on the properties and formation mechanism of flexible nanocomposite hydrogels from cellulose nanocrystals and poly(acrylic acid). *Journal of Materials Chemistry* 22:22467-22480.

Yang J., Han C. R., Duan J. F., Xu F. and Sun R. C. 2013b. Mechanical and Viscoelastic Properties of Cellulose Nanocrystals Reinforced Poly(ethylene glycol) Nanocomposite Hydrogels. *Acs Applied Materials & Interfaces* 5:3199-3207.

Yang X., Liu Q., Chen X., Yu F. and Zhu Z. 2008. Investigation of PVA/ws-chitosan hydrogels prepared by combined γ-irradiation and freeze-thawing. *Carbohydrate Polymers* 73:401-408.

Yano H., Sugiyama J., Nakagaito A. N., Nogi M., Matsuura T., Hikita M. and Handa K. 2005. Optically transparent composites reinforced with networks of bacterial nanofibers. *Advanced Materials* 17:153-+.

Zhang W., Yang X. L., Li C. Y., Liang M., Lu C. H. and Deng Y. L. 2011. Mechanochemical activation of cellulose and its thermoplastic polyvinyl alcohol ecocomposites with enhanced physicochemical properties. *Carbohydrate Polymers* 83:257-263.

Zhou C. J. and Wu Q. L. 2011. A novel polyacrylamide nanocomposite hydrogel reinforced with natural chitosan nanofibers. *Colloids and Surfaces B-Biointerfaces* 84:155-162.

CHAPTER 5 HIGH-WATER-CONTENT MOULDABLE POLYVINYL ALCOHOL-BORAX HYDROGELS REINFORCED BY WELL-DISPERSED CELLULOSE NANOPARTICLES: DYNAMIC RHEOLOGICAL PROPERTIES AND HYDROGEL FORMATION MECHANISM

5.1 INTRODUCTION

Hydrogels are soft, viscoelastic and cross-linked (physically and/or chemically) three-dimensional networks of hydrophilic polymer that can hold large amounts of water and/or biological solution, while maintaining their structural integrity during deformation (Yang et al. 2012; Yang et al. 2008). Due to their excellent hydrophilicity, permeability, ability to mimic human tissues, hydrogels are particularly attractive in biological, pharmaceutical, and health-care applications, such as real-time immunoassay, contact lenses, vehicles for drug delivery, cell encapsulation, implantable artificial muscles and organs, and biosensors (Sun et al. 2012; Yang et al. 2013). The growing environmental awareness recently has triggered interests in more environmentally friendly and biodegradable hydrogels (Zhang et al. 2011). Due to the hydroxyl groups of each repeating molecular unit, hydrophilic polyvinyl alcohol (PVA) can form chemically and/or physically crosslinked hydrogels. Most PVA hydrogels are biodegradable, highly crystalline, non-toxic, inexpensive, biocompatible, and non-carcinogenic (Asher et al. 2008; Kobayashi et al. 2005). For example, a type of PVA-based hydrogel known as Salubria TM (Salumedic, Atlanta, GA) is marketed in Canada and Europe for articular cartilage replacement (Slaughter et al. 2009). However, there are many applications requiring stronger hydrogels (e.g., electrochemical devices and medical implants). To enhance the mechanical strength and toughness of hydrogels, composite hydrogels have been synthesized by incorporating nanoparticles, including carbon nanotubes, metallic particles, and inorganic clay (Shin et al. 2009). These reinforcing nanofillers generally act as decelerators of propagating

cracks and contribute to delaying the collapse of the composite hydrogels (Shin et al. 2009). Inspired by the recent environmental concerns, eco-friendly composite hydrogels based on renewable natural resources (e.g., cellulose, most abundant renewable natural biopolymer in nature) have assumed great significance for reinforcing various polymers. More importantly, cellulose exhibits a low immune response and cannot be degraded and digested in the body due to the fact that human and animal cells do not synthesize the enzymes capable of degrading cellulose (cellulases), thus cellulose reinforced hydrogels are particularly suitable for certain biomedical fields.

In our previous study (Han et al. 2013c), we successfully synthesized PVA-borax hydrogels that were reinforced by well-dispersed cellulose nanoparticles (CNPs). The obtained tough, high-water-capacity (~96%), low-density (~1.1g/cm^3), translucence hydrogels exhibited birefringence textures and a higher transparency than the cyclic freeze-thaw prepared opaque hydrogels. Highly-crystalline CNPs acted as a multifunctional crosslinking agent to physically and chemically bridge the 3D network hydrogels. By respectively incorporating three types of uniform-dispersed CNPs to the PVA-borax aqueous system, mechanical strength, energy absorption and stiffness of the composite hydrogels were significantly enhanced.

Application of the hydrogels in many fields requires a fundamental understanding of their viscoelastic properties. Among those techniques that have been used to investigate the gelation kinetics of PB aqueous system, dynamic rheological techniques have attracted strong interest as a powerful and effective approach to study the supramolecular structure of hydrogels since in situ experiments are relatively facile to perform during the gelation process (Shi et al. 2012). The network structure and the cross-linking density are key factors derived from the rheological characteristics of the hydrogels (Kjøniksen and Nyström 1996). The linear viscoelastic behavior

in dynamic experiments of miscible gelling polymer systems can continuously monitor the development of cross-links (chemical and/or physical) and supramolecular complexes in hydrogel without disrupting gel structure, and they can further reflect the miscibility of polymer blends, supramolecular structure and cross-linking density of hydrogels in stages. As a result, effort has been devoted to the rheology study of PVA-borate complex aqueous systems over the past several decades (Angelova et al. 2011; Carretti et al. 2009). The effects of polymer concentration, molecular weight and temperature on the dynamic viscoelasticity of PVA in aqueous borax solutions were discussed (Koike et al. 1995). The thermo-dynamic, structural, and dynamic features of cross-linked PVA hydrogels and the corresponding semidilute polymer solutions were also reported (Kjøniksen and Nyström 1996). The crosslinking mechanism of borate ion with PVA chains was known to be a "di-diol" complexation, which was formed between one borate ion and two diol units. PB aqueous system rheologically behaved like elastic solids at high frequencies and like viscous liquids at low frequencies. The short relaxation time and small amount of energy required to break and reform the cross-links accounted for the "slime" consistency of these materials (Angelova et al. 2011). Above-mentioned studies indicate that dynamic rheology techniques can distinguish appropriate gelation conditions for the fabrication of PB hydrogels with desired properties. Regarding the industrial potential in the processing of related materials, the knowledge of the dynamic rheological behavior of PB-based system is very useful in equipment selection and quality control (Gouvea et al. 2009).

However, to the best of our knowledge, we are unaware of any reports on the gelation mechanism and viscoelasticity of PVA-borax-CNP complexes in an aqueous system. For instance, the effects of different CNPs on the rheological features of PB aqueous systems have not been addressed. It is possible that the physically and chemically crosslinked hydrogels can

exhibit some unique viscoelastic properties. The objectives of this study were to characterize the dynamic rheological behavior of the obtained hydrogels, and to explore the plausible mechanism for the multi-complexation among CNPs, PVA and borax for a better understanding of the relationship between 3D network structure and hydrogel properties, which could further deepen the fundamental knowledge of how hydrogels were strengthened by CNPs in the presence of borax. Insights into the structural and viscoelastic changes that occurred when the nature of CNPs were changed were obtained from analyses of rheology data. In the work, the effects of particle size, aspect ratio, crystal structure, surface charge and minimum overlap concentration of different CNPs on the dynamic rheological properties and performance of the hydrogels were investigated. Through dynamic oscillation measurements, the enhancement effect of CNPs on the composite hydrogels was verified. Since dynamic bonds formed between the $B(OH)_4^-$ and the OH groups on the sides of the PVA (and/or CNPs) are reversible and exchangeable, the self-healing ability and thermo-reversibility of as-prepared composite hydrogels were also demonstrated. In addition to providing fundamental insight into factors controlling the efficiency of the cross-links and the interactions among these network components of the composite hydrogels, this work described a new type of soft matter with some unique properties that can be tuned by the incorporation of different CNPs to meet the requirements of specific applications.

5.2 EXPERIMENTAL

5.2.1 Materials and Hydrogel Preparation

Three kinds of CNPs were isolated from bleached wood pulp using alkali pretreatment and/or sulfuric acid hydrolysis followed by a high-pressure homogenization process as previously described in our work (Han et al. 2013). The cellulose nanocrystals with I and II crystalline allomorphs as well as the cellulose nanofibers with crystal I structure were designated

as CNC I, CNC II and CNF I, respectively. Their corresponding length, width and aspect ratio were 149 ± 40, 46 ± 18 and 732 ± 208 nm; 9 ± 2, 5 ± 1 and 21 ± 7 nm; 16.6, 9.4 and 36.6, respectively (Han et al. 2013). The obtained CNP aqueous suspensions (1.0 wt%) were stored at 5^{o}C in a refrigerator before use. As previously described (see manuscript 1), dried borax powder (sodium tetraborate decahydrate, over 99.5% purity, $Na_2B_4O_7 \cdot 10H_2O$, M_w=381.37 g mol^{-1}, Aldrich Chemical Co.) was dissolved in 1.0 wt% CNP aqueous suspensions at room temperature to obtain the aqueous solutions with 0.4 wt% of borax. A weighed amount of PVA powder (M_w=146.000-186.000 g mol^{-1}, 99.0+% hydrolyzed, Aldrich Chemical Co.) was then slowly sprinkled onto the surface of the stirred aqueous solutions. After a complete swelling of PVA powder, the solutions were heated to 90^{o}C and stirred for 2 h. After the PVA was completely dissolved, homogeneous translucent solutions with well-dispersed CNPs were formed. As the temperature decreased, the mixture started to present viscoelastic properties. The solutions were further cooled slowly to room temperature to in-situ form the final hydrogels. All the hydrogels were homogeneous and stable even after they were allowed to stand for more than 8 months at room temperature. Accordingly, the PVA-borax hydrogel was prepared by directly dissolving PVA powder (2.0 wt%) into borax aqueous solutions (0.4 wt%). All other processing conditions were the same as those used for the CNP-PVA-borax hydrogels. On the whole, all the hydrogel samples contained 2.0 wt% of PVA and 0.4 wt% of borax. The hydrogels with 1.0 wt% of CNC I, CNF I and CNC II were designated as PB-CNC I, PB-CNF I and PB-CNC II, respectively, and they were collectively referred to as CNP-reinforced PB hydrogels. The PVA-borax-water complex solution was designated as PB. Deionized water was used for the solution preparation. All solvents and reagents were of analytical grade.

5.2.2 Dynamic Oscillation Measurement

The hydrogels (PB, PB-CNC I, PB-CNF I and PB-CNC II) and suspensions (CNCI, CNF I and CNC II at 1.0 wt%) were transferred to airtight vials to prevent the evaporation of water. They were then allowed to equilibrate for three days for complete structure formation prior to testing. The dynamic rheological behaviors, including dynamic strain sweep, dynamic frequency sweep, continuous step strain and dynamic temperature sweep, were investigated with an AR2000EX controlled-stress Rheometer (TA Instruments Inc., New Castle, DE) using plate-and-plate geometry (diameter 40 mm, gap 500 μm). The upper plate was made of stainless steel, and the lower plate was a Peltier device with a specially designed temperature control system. For each measurement, to minimize shearing during sample loading, approximately 0.6 ml of each sample was carefully loaded onto the Peltier plate using a tablespoon. After their loading, the upper plate was set at a desired distance above the Peltier plate, and then, all samples were equilibrated without pre-shearing or oscillating for 10 min at 25^{o}C prior to conducting the experiments. To avoid the evaporation of water and the oxygen contamination during measurements, the gap between two plates was sealed with the solvent trap cover, and the moat on the top of the cover was filled with the low viscosity silicon oil.

5.2.3 Dynamic Strain Sweep

Before the dynamic viscoelastic measurements, the dynamic strain sweep from 0.01 to 100% at ω=1.0 Hz was first performed, and the storage modulus was recorded to define the linear viscoelastic region (LVR), in which the storage modulus is independent to the strain amplitude. A strain (γ) of 1.0% was selected in the subsequent oscillation tests to ensure that the dynamic oscillatory deformation of each sample was within the LVR.

5.2.4 Dynamic Frequency Sweep

The viscoelastic parameters (log mode), including shear storage modulus (G′) and loss modulus (G″) as functions of angular frequency (ω) were measured over the ω range of 0.1-100 rad/s at γ=1% at 25°C. The complex modulus (G*), complex viscosity (η*), and loss tangent (tan δ) were calculated by eq. 5.1, 5.2 and 5.3, respectively:

$$G^* = \sqrt{G'^2 + G''^2} \tag{5.1}$$

$$\eta^* = G^*/\omega \tag{5.2}$$

$$\text{Tan}\,\delta = G''/G' \tag{5.3}$$

5.2.5 Continuous Step Strain

To investigate the recovery properties of the hydrogels in response to applied shear forces (expressed in terms of strain), two different 1h-programmed procedures were used as follows (strain% and duration in parentheses): for PB-CNF I, 1.0% (700 s) → 100% (700 s) → 1.0% (700 s) → 100% (700 s) → 1.0% (800 s); for PB-CNC I, 10% (700 s) → 100% (700 s) → 10% (700 s) → 100% (700 s) → 10% (800 s), and the G′ and G″ dependence of time was recorded in continuous step strain measurements at ω=1.0 Hz and at 25°C.

5.2.6 Dynamic Temperature Sweep

To test the thermo-reversibility by the dynamic temperature sweep, the hydrogel samples were measured through a heating-cooling-heating process (10-70-10-70°C) at ω=1.0 Hz and γ=1.0%. The heating and cooling rates were 2.0 and 1.0 °C/min, respectively (Li et al. 2001). Each measurement was repeated three times.

5.3 RESULTS AND DISCUSSION

5.3.1 LVR Determined by Dynamic Strain Sweep

Figure 5.1a shows the G′ as a function of γ for each sample based on the results from dynamic strain sweep tests, demonstrating a typical elastic response of hydrogels. In the dynamic oscillation approach, increasing cyclic levels of γ (from 0.01 to 100%) were applied at ω=1.0 Hz. Within LVR, the G′ values of these hydrogels were basically independent of the applied γ, behaving like a viscoelastic solid. The points at which the G′ values deviated by more than 5% from the plateau values indicated departure from linear viscoelastic behavior and therefore were defined as the critical strains (γ_c) for each sample (Gao et al. 2008). The G′ values then gradually decreased above the γ_c, indicating a transition of the hydrogel samples from the quasi-solid state to a quasi-liquid state. As shown in Table 5.1, the γ_c values of PB-CNF I, PB-CNC I and PB-CNC II were 2.0, 3.2 and 31.7%, respectively. Consequently, the γ=1.0% was selected in the subsequent oscillation tests to ensure that the following dynamic oscillatory deformation of each sample was within LVR. The corresponding G'_{max} values were 1715, 1223 and 206 Pa, respectively. As noted from the graph, the three types of CNP-reinforced hydrogels exhibited significantly higher G` values than PB or 1.0 wt% CNP colloids. For example, the G'_{max} value of PB-CNF I was two order of magnitude greater than that of PB, and it was also 20 times larger than that of 1.0 wt% CNF I colloid. As expected, the addition of a small amount (1.0 wt%) of CNPs pronouncedly increased the viscoelasticity and stiffness of PB hydrogel. In general, the LVR is shortest when the sample is in its most solid form. Compared with PB-CNC I and PB-CNC II, PB-CNF I presented a relatively higher G'_{max}, a shorter LVR and therefore a lower γ_c. This phenomenon indicated that PB-CNF I was the strongest hydrogel.

5.3.2 Dynamic Viscoelasticity of Hydrogels

To understand the influence of various CNPs on the viscoelastic properties of hydrogels, oscillatory measurements were carried out at 25^{o}C in PB-CNC I, PB-CNF I, PB-CNC II and PB hydrogels, as well as the 1.0 wt% cellulose colloidal suspensions (Figure 5.1). The G′ (elasticity) and G″ (viscosity) as a function of ω for hydrogels within the linear deformation range are illustrated in Figure 5.1b. It was clearly observed that the G′ (ω) or G″ (ω) values of these hydrogels essentially followed a similar trend, thus the moduli curves of PB-CNC I were taken as an example to interpret the viscoelastic behavior of hydrogels. At low frequencies where G″ (ω) > G′ (ω) (tanδ > 1.0 in Figure 5.1e), quasi-liquid behavior was dominating. As ω proceeded, there was a regional monotonic increase in moduli. Simultaneously, G′ (ω) was gradually getting closer to G″ (ω) until a crossover point of G′ (ω) and G″ (ω) curves appeared, suggesting the entanglement of polymer chains and the formation of an elastic gel network (Wang and Chen 2011). After the crossover point where G′ (ω) = G″ (ω), G′ (ω) continued to increase to reach a plateau region (indicative of polymer entanglements) (Lin et al. 2005), and it exceeded the G″ (ω) at high frequency range, whereas the curve of G″ (ω) reached its peak and then started to decrease. At high frequencies where G′ (ω) > G″ (ω) (tanδ < 1.0 in Figure 5.1e), the elastic character became the dominant factor, exhibiting a typical solid-like character. These features corresponded to the typical viscoelastic material with a narrow distribution of relaxation times (Inoue and Osaki 1993). It was noticed that the moduli curves of PB-CNF I only showed the rubbery zone within the accessible frequency window (ω=0.1-100 rad/s), indicating that their intersection located out of ω window and the gelation occurred at a lower ω, earlier than other samples. According to its viscoelastic properties and the trend of moduli curves of the other gelatinous samples, the crossover point of PB-CNF I was roughly estimated to be at ω < 0.1,

where G′ (ω) = G″ (ω) ≈ 246 Pa. It was generally considered that the presence of crossover between the G′ (ω) and G″ (ω) curves was the sign of gelation (Boluk et al. 2012), suggesting the formation of the elastic three-dimensional network of both entangled chains and reversible or transient cross-links (Carretti et al. 2009).

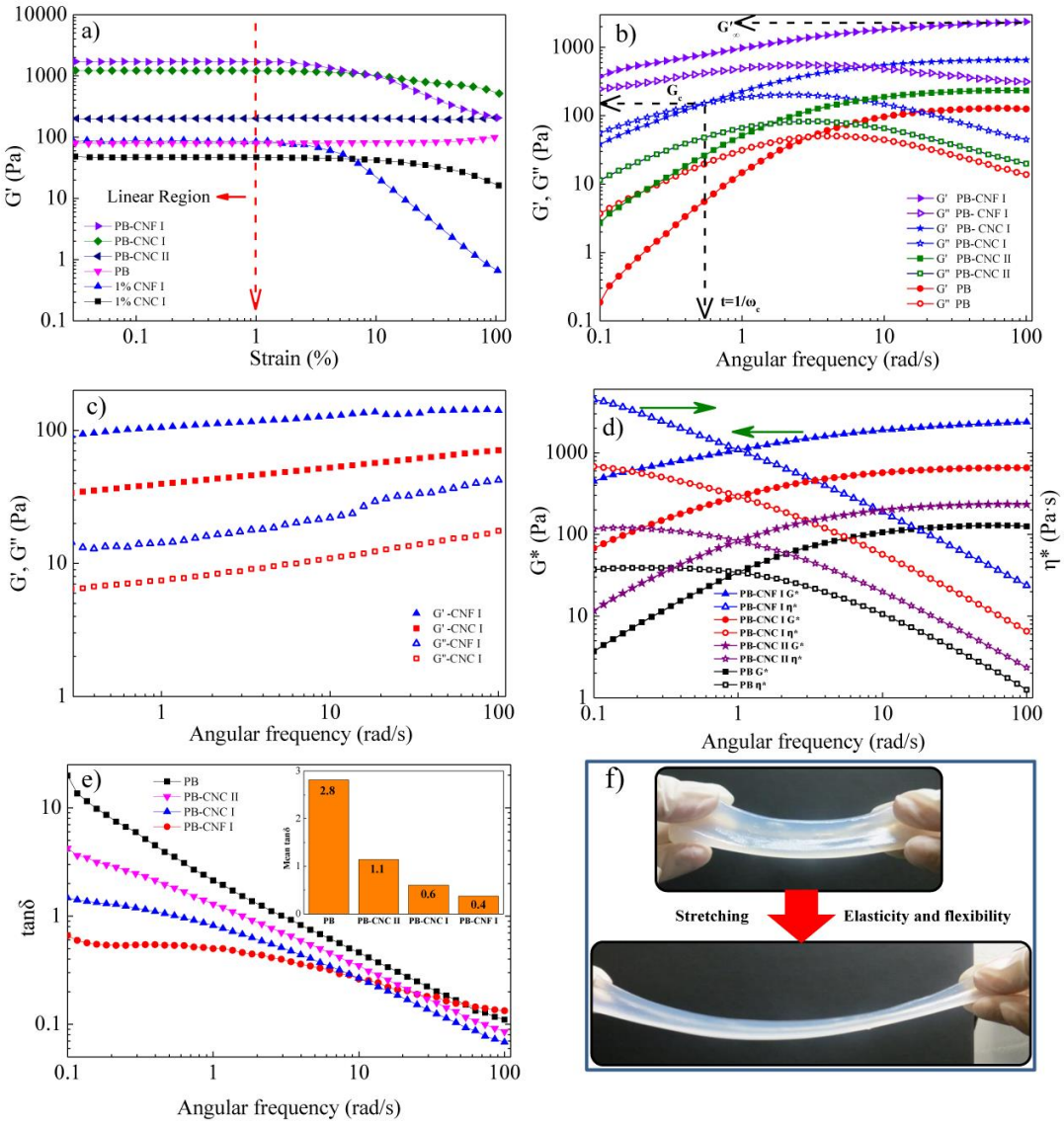

Figure 5.1 Dynamic viscoelasticity performance of hydrogels at 25 ^{o}C: (a) strain dependence of G′ for hydrogels and cellulose colloidal suspensions, measured at ω=1.0 Hz; (b) frequency dependence of G′ and G″ for hydrogels and (c) 1.0 wt% cellulose colloids measured at γ = 1.0%; (d) frequency dependence of G* and η* for hydrogels; (e) frequency dependence of tanδ for hydrogels; (f) Stretching ability of PB-CNF I.

Before the incorporation of PVA and borax, G′ and G″ curves of 1.0% CNF I colloid and CNC I suspension were relatively independent of ω throughout the whole ω range (Figure 5.1c), evidencing the formation of a gel-like transient network structure of entangled nanofibers (Rezayati Charani et al. 2013). The slight increase for moduli indicated that the pure cellulose network structure was gradually disequilibrated as shear stress increased, because CNPs were allowed to rearrange and to form an ordered network structure again. G′ and G″ curves were almost parallel and G′ was one order of magnitude higher than that of G″ at ω=0.1-100 rad/s, indicating a rather stable and strong networking of the colloid (Wang and Chen 2011). The G′ values of CNF I was nearly one order of magnitude greater than those of CNC I throughout the measured ω window (0.1-100 rad/s), indicating a more gel-like behavior of CNF I colloid due to the inherent entangled 3D networks that were constructed by the higher aspect ratio CNF I (Agoda-Tandjawa et al. 2010; Liu et al. 2011). The other reason was that the critical concentration of CNF I was smaller than that of CNC I, which was detailed in the following mechanism discussion.

Table 5.1 Rheological characteristics of hydrogels derived from moduli curves.

Parameters	Hydrogels			
	PB	PB-CNC II	PB-CNC I	PB-CNF I
Crossover frequency, ω_c (rad/s)	2.93	1.59	0.54	< 0.10
Crossover modulus, G_c (Pa)	48	76	151	~246
Dynamic relaxation time, t (s)	0.34	0.63	1.85	> 10.0
High-frequency plateau of G′, G'_∞ (Pa)	125	233	652	2356
Maximum G″, G_m'' (Pa)	50	83	202	552
Correlated frequency at G_m'', ω_m (rad/s)	3.98	3.42	2.15	2.93
Longest relaxation time, t_L (s)	0.25	0.29	0.47	0.34
Critical strains, γ_c (%)	n.a.	31.7	3.2	2.0
Maximum G′ within LVR, G'_{max} (Pa)	80	206	1223	1715

Because of the non-Newtonian behavior of the CNP-reinforced PB hydrogels, the combination of fluid-like and solid-like properties made them a Maxwell material. Due to a rough approximation to a model with a single Maxwell element (Ivanov et al. 2004), the hydrogels could be characterized by the following parameters around the crossover coordinates, crossover modulus (G_c), crossover frequency (ω_c), and dynamic relaxation time (t) of the system (defined as $t=1/\omega_c$) (Angelova et al. 2011). It was previously reported that the variations in G_c and t represented the changes in the degree and the lifetime of the cross-linking within the hydrogels, respectively (Piculell et al. 2003). On the other hand, as noted in Figure 5.1b and Table 5.1, the intersection point (G_c) did not correspond to the maximum value of $G''(\omega)$ for each hydrogel sample, revealing that the viscoelastic properties of the hydrogels should not be described only by one t or by one Maxwell element model (Gao et al. 2008; Koike et al. 1995; Piculell et al. 2003). In other words, even though the single Maxwell element together with the single relaxation time (t) clearly outlined the great differences between different hydrogels, it seemed that a single Maxwell element was no longer enough to describe the behavior of the hydrogels, especially for the PVA-borate-based system (Carretti et al. 2009; Ivanov et al. 2004). Based on Chompff-Duiser theory and modified Rouse theory (Chompff and Prins 1968), the relaxation spectrum was predicted to illustrate the maximum of characteristic entanglement slipping mechanism. Accordingly, the curve of $G''(\omega)$ should possess a maximum value (G_m''), and that of $G'(\omega)$ should have a flat plateau (G'_∞). For this reason, some other characteristic parameters derived from moduli curves could also be used to evaluate the hydrogels in the study: plateau value of G' at high frequencies (G'_∞), the maximum value of G'' (G_m''), correlated frequency ω_m at G_m'' and the longest relaxation time t_L (defined as $t_L = 1/\omega_m$). The t_L was described as the time for a given macromolecules to disengage by a snake-like motion from a

tube consisted of neighboring polymer chains (Gao et al. 2008). The estimated values of these parameters for the hydrogels in Figure 5.1b were given in Table 5.1.

The most striking difference was observed in G'_∞, which was in the order of PB-CNF I > PB-CNC I >PB-CNC II > PB. For example, with the addition of CNF I, an increase of almost 19-fold in G'_∞ was observed for PB-CNF I compared with that of pure PB hydrogel, suggesting the cross-link role and enhancement effect of CNPs. On the other hand, the G'_∞ values of PB-CNF I (2356 Pa) and PB-CNC I (652 Pa) were much higher than the G' values of CNF I (141 Pa) and CNC I (70 Pa) colloids at the same cellulose concentration of 1.0 wt% (Figure 5.1c), respectively, indicating a strong interaction and entanglement between CNPs and polymer chains. The presence of G'_∞ also indicated that some internal structures might exist, showing the gelation character of the CNPs (Boluk et al. 2012). On the basis of the correlation between entanglement density (ρ_e) and G'_∞ ($G'_\infty=\rho_e k_B T$) (Schubert et al. 2003), the G'_∞ value (a solid-like characteristic) could be used with rubber elasticity theories to estimate the crosslink density. Therefore, the degree of cross-linking by polymer junctions in the cellulose reinforced hydrogels should follow the similar order: PB-CNF I > PB-CNC I > PB-CNC II. Additionally, the crossover modulus (G_c) of these hydrogels, which also provided information about the degree of cross-linking (Carretti et al. 2009), had the same sequence as G'_∞, further confirming the increase in entanglement density from PB to PB-CNF I. This result was further explained by the minimum overlap concentration of CNPs in the mechanism discussion. In addition to the increase in the quantity of cross-links, the increased G'_∞ might also originate in the anionic charges carried by monodiols in the PVA-borax network, thus resulting in a stronger repellence of the polymeric chains (Ivanov et al. 2004).

Being consistent with the increase in G'_{∞}, the relaxation time (t) of the cellulose reinforced hydrogels was considerably extended in the order of PB-CNF I > PB-CNC I >PB-CNC II > PB. Specifically, the t of PB-CNC I was almost 6 times longer than that of neat PB hydrogel, revealing a much slower shear-induced rearrangement of the 3D network and dissociation of cross-links of PB-CNC I under oscillatory shear (Carretti et al. 2009). The relaxation time (t) represented the shape stability of hydrogel. As shown in Figure 5.1c, PB-CNF I with longer relaxation time (t > 10) could be moulded into a more regular cube compared to PB-CNC I (t = 1.85) and PB-CNC II (t = 0.63), while pure PB hydrogel with a much smaller relaxation time (t = 0.34) was not even mouldable. It was generally considered that an increase in t was probably ascribed to a longer lifetime of the cross-links under physical forces, denser polymer entanglements or a higher cross-link density, and the existence of two types of interacting polymer chains slowed down the relaxation process in the hydrogel due to entanglements and different strength of cross-links (Ivanov et al. 2004). It was previously reported that neither borate nor PVA concentration affected the distribution of relaxation times (Robb and Smeulders 1997). Therefore, different nature of these three kinds of CNPs and their interaction with PVA-borax system were mainly responsible for the different hydrogel properties.

It was also found that the G_m'' values of hydrogels were in the same order of PB-CNF I > PB-CNC I >PB-CNC II > PB, which was in an agreement with the results of t and G'_{∞}. This phenomenon showed the gradual increase in effective degree of crosslinking and chain entanglement from PB (G_m'' = 50 Pa) to PB-CNF I (G_m'' = 552 Pa) (Fang et al. 2004). The plots of complex modulus (G*), complex viscosity (η*) and loss tangent (tan δ) as a function of ω provided a sharper contrast of these hydrogels (Figure 5.1d, e), where PB-CNF I possessed the highest G* and η* as well as the smallest tan δ within the whole ω range, further confirming that

PB-CNF I was the strongest and most elastic hydrogel among these samples. As shown in Figure 5.1f, rubbery PB-CNF I could be stretched into a thin film without damage, exhibiting its high elasticity and flexibility. This observation suggested that the hydrogel possessed outstanding damage-tolerant ability and efficient energy dissipation behavior. It is well-known that tan δ represents the ratio of dissipated energy to stored energy during the stress deformation. The tan δ values of PB-CNF I were lower than 1 throughout the whole ω range (Figure 5.1e) and the corresponding mean tan δ was 0.4 (Insert in Figure 5.1e). Because polymer chains physical entanglements were disentangled and then reconstituted during dynamic strains, the dynamic entanglement–disentanglement equilibrium process provided the network with the energy release capacity (Yang et al. 2012). Their elastomeric nature was probably due to the entanglements of long CNF I and flexible PVA chains via hydrogen bonds and physical junctions with the presence of borax. The homogeneously dispersed CNPs in PVA-borax system were thus regarded as multifunctional cross-links and enhancement fillers.

However, the longest relaxation times (t_L) of hydrogels were in a different order of PB-CNC I > PB-CNF I >PB-CNC II, which was coincident with the sequence of the corresponding Zeta potential (absolute value) of CNC I, CNF I and CNC II (i.e., $\left|-57.07 \pm 1.06\right| > \left|-32.61 \pm 1.12\right| > \left|-0.63 \pm 0.08\right|$ mV) (Han et al. 2013). In our previous work, we mentioned that the negatively charged CNPs electrostatically repulsed each other. Therefore, the highly charged CNC I (Zeta potential = -57.07 ± 1.06 mV) increased the organization and the stability of the hydrogel, leading to a longer t_L of PB-CNC I. In the CNP-PVA-borax system, various polymer chains might be reversibly linked to a neighboring chain through crosslinks. During the polymer reptation caused by external oscillatory shear, the exchange rate for the formation of temporarily intermolecular crosslinks was reduced due to a more stable network formed by highly negatively

charged fibers.[26] To sum up, these results showed that the incorporation of CNPs significantly increased t, t_L, G'_∞, G_m'' and G_c. It was thus concluded that the CNPs strengthened the 3D entangled networks of the PB hydrogels.

5.3.3 Self-recovery of the Hydrogels under Continuous Step Strain

Interestingly, it was noted that these high-water-content hydrogels exhibited particular recovery of their mechanical characteristics after a large-amplitude oscillatory collapse, indicating a thixotropic nature (Wang et al. 2010). As shown in Figure 5.2a, beginning to be deformed at small-amplitude oscillatory force (γ=1.0%), PB-CNF I first present a solid nature with a G′ of 12.0 KPa and a G″ of 5.1 KPa ($\tan\delta = G''/G' \approx 0.4$). Under the application of a large-amplitude one (γ=100%), the G′ and G″ values of PB-CNF I subsequently decreased to 0.23 and 0.7 KPa, respectively, leading to a quasi-liquid state of hydrogel ($\tan\delta \approx 3.0$). However, more importantly, when the γ is reduced once again to 10%, G′ and G″ immediately recovers their initial values and the hydrogel returned to the original quasi-solid state ($\tan\delta$ = 4.5 KPa / 12.2 KPa ≈ 0.4). Accordingly, PB-CNC I showed similar recovery properties in response to applied shear forces, which also experienced the state transition between quasi-liquid (G″ > G′ at γ=100%) and quasi-solid (G″< G′ at γ=10%) under oscillatory collapse (Figure 5.2b). Nonetheless, under the same oscillatory force (for example, γ=100%), the G′ and G″ of PB-CNF I were greater than those of PB-CNC I (G′ ≈ 0.14 KPa, G″ ≈ 0.41 KPa), confirming that PB-CNF I were more elastic and stronger, which was consistent with the results of compression and dynamic rheology testing.

Because of the reversible cross-links between PVA (or CNPs) and borax, these high-water-content and translucent hydrogels could be manually moulded into various 3D shapes (Figure 5.2c), suggesting their high malleability and flexibility.

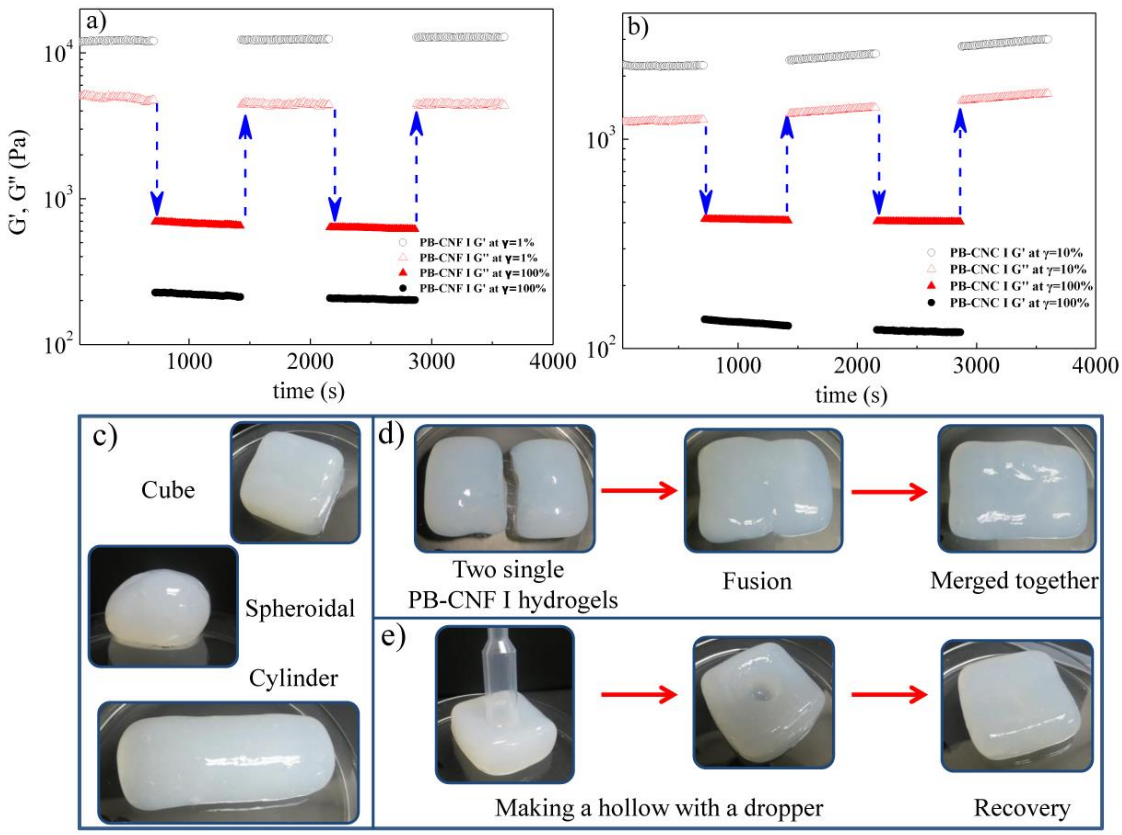

Figure 5.2 The G′ and G″ dependence of time in continuous step strain measurements for PB-CNF I (a) and PB-CNC I (b); Shape-persistent, free-standing macroscopic objects moulded from a PB-CNF I hydrogel (c); Process of merging two single PB-CNF I hydrogels together (d); The demonstration of shape recovery for PB-CNF I (e).

In addition, when two blocks of PB-CNF I were pushed together, their surfaces came into adhere to each other, resulting in a fusion phenomenon (Figure 5.2d). After readily handling by hand, they could be totally merged together, which was a sign of apparent self-healing property (Schultz and Myers 1969). This external force–induced coalescence of rubbery hydrogels was probably attributed to their high water content and the hydrophilic nature of polymer chains. To further demonstrate their self-recovery ability, a plastic transfer pipette was inserted into a block of PB-CNF I to create a hollow on the surface of hydrogel (Figure 5.2e). As expected, the hollow gradually disappeared under external force, revealing that the flexible hydrogel network could

bear strong force and dissipate a large amount of energy without permanent change in 3D-network structure.

5.3.4 Thermo-reversibility of the Hydrogels Characterized by Temperature Sweep

To understand the behavior of hydrogels at different energy states, the CNP reinforced hydrogels were subjected to a temperature sweep study. The junctions of PVA-borate were thermoreversible cross-links with a finite lifetime (determined by oscillation measurement and mechanism section), and some cellulose-based gels also exhibited thermo-reversible characteristic, thus the thermo-reversibility (referred to the reversibility responding to temperature) of these mouldable hydrogels was expected. To test this hypothesis, the hydrogels were developed via a first heating process beginning from a low temperature of 10 ℃ to 70 ℃ at a heating rate of 2 ℃/min, and were then cooled slowly to 10 ℃ at a cooling rate of 1.0 ℃, and eventually went through a second heating process that was identical to the first one. Figure 5.3 shows temperature dependence of moduli (G′ and G″) for cellulose reinforced hydrogels under the heating-cooling-heating process (10-70-10-70 ℃) at ω=1.0 Hz and γ=1.0%. It appeared that PB-CNF I, PB-CNC I and PB-CNC II exhibited a similar thermo-behavior, therefore PB-CNF I was taken as an example to demonstrate the thermal-induced transition of hydrogels (Figure 5.3a). During the entire heating-cooling-heating circle, G′ was throughout higher than G″, indicating the completion of gelation and an elastic hydrogel network.

Starting from 10 to 45 ° C in the first heating process, the moduli were roughly independent of temperature, and yet G′ decreased very slightly with elevation of temperature, suggesting the stable cross-linking structure and more entanglements between CNPs and polymer chains around room temperature (Shi et al. 2012; Yang et al. 2008). The moduli increased gradually with further increase of temperature from 45 to 70 ℃, which might be caused

by the formation of a denser network at higher temperatures. Due to the high-water-content nature of the hydrogels ($M_C \approx 96\%$), this phenomenon might be better understood by taking into account the thermal-induced water evaporation inside the hydrogels (Figure 5.3d).

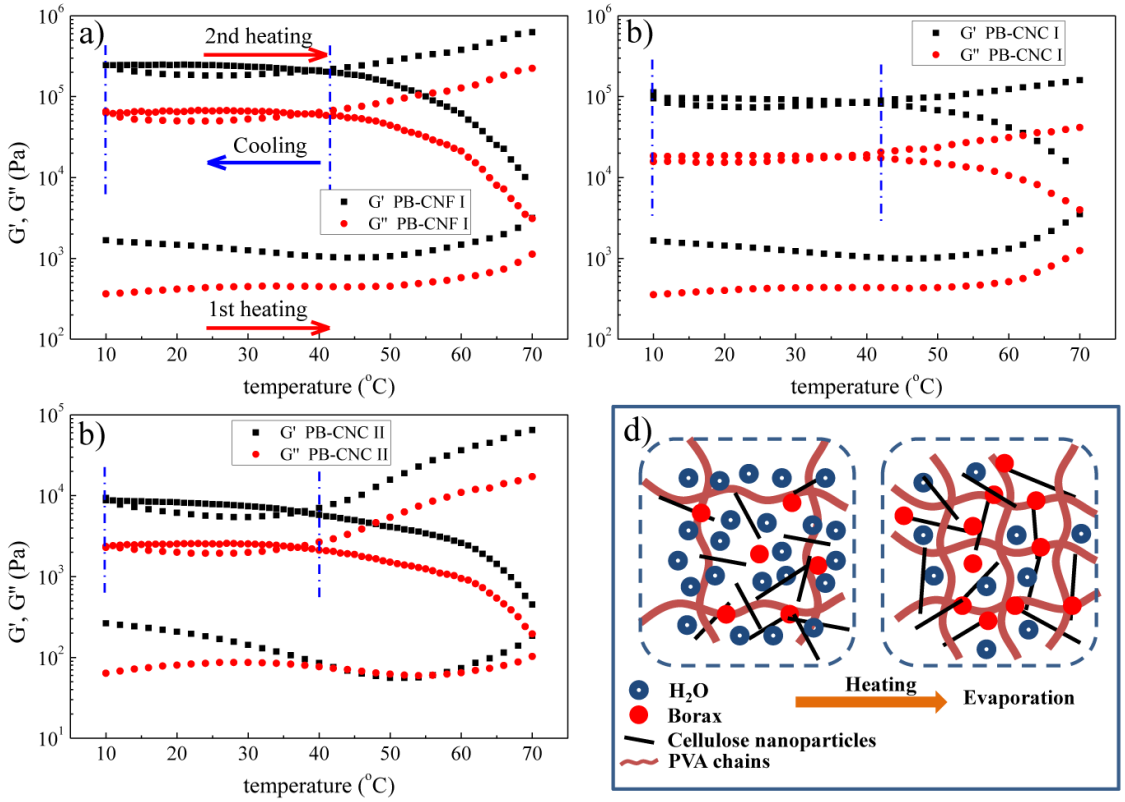

Figure 5.3 Temperature dependence of G′ and G″ for PB-CNF I (a), PB-CNC I (b) and PB-CNC II (c) during a heating-cooling-heating circle (10-70-10-70 ℃) at ω=1.0 Hz and γ=1.0%, and mechanism of thermo-reversibility (d).

At higher temperature range from 45 to 70 ℃, the concentrations of cellulose and polymer increased due to the inevitable water evaporation of hydrogels, leading to shorter distances among CNPs and/or polymer chains and accordingly a higher cross-linking density of hydrogel structure. In addition to the water evaporation factor, the increased physical cross-linking and more chain entanglements at elevated temperature also contributed to the positive dependence of moduli on the temperature ranging from 45 to 70 ℃ (known as thermal-induced hardening of hydrogels) (Shi et al. 2012). A similar comportment was previously reported for

pure cellulose solution. The cellulose solution exhibited more elastic behavior at high temperature because of the junctions between cellulose chains and the formation of networks (Cai and Zhang 2006). Consequently, the thermal-induced rheological properties of the CNP reinforced hydrogels were similar to that of the cellulose solution, indicating the homogeneous nature of the hydrogels (Shi et al. 2012). Furthermore, better solubilization of borate ions around 60 ℃ contributed towards better interaction and complexation (compacter network) inside the hydrogel structure during heating (Gouvea et al. 2009).

At the lower temperature range from 10 to 45 ℃, the thermal-induced water evaporation was quit slow and even negligible, so the moduli showed almost no dependence on temperature in this range. For the following cooling process, the moduli increased rapidly from 70 to 45 ℃, and the ascent rate of moduli was much greater compared to the descent rate of moduli within the same temperature range in the first heating process, which was probably due to the continuous and intense evaporation at higher temperature. Subsequently, at lower temperature range from 45 to 10 ℃, the moduli reached a temperature-independent plateau, suggesting that the temperature region between 10 and 45 ℃ was indeed suitable to test the thermo-reversibility. Because the thermo-reversibility of a hydrogel is an important characteristic that is directly related to the energy involved in the hydrogel network structure (Gao et al. 2008; Li et al. 2001), the thermal-induced water evaporation will affect the thermal-induced behavior, especially for a high-water-content hydrogel. For this reason, the thermo-reversibility of a hydrogel makes sense only when the water evaporation can be practically ignored. To verify the thermo-reversibility, the hydrogels experienced the second heating process. At lower temperature range from 10 to 45 ℃ where water evaporation of hydrogels was almost negligible (confirmed by first heating process), the moduli curve of the second heating process basically overlapped the cooling curve,

revealing that hydrogels stiffening during cooling was almost completely thermo-reversible (Renkema and van Vliet 2002). While at higher temperature range from 45 to 70 ℃ where water evaporation of hydrogels became more intensified (determined by first heating process), the moduli curve rose again with the same ascent rate as the first heating process. Similar thermo-reversibility of the hydrogels prepared by related polymers was proposed previously, such as glucomannan/borax gel (Gao et al. 2008), short-chain O-(2,3-dihydroxypropyl) cellulose/borax hydrogel (Ide et al. 1998), and crystalline colloidal array embedded PVA hydrogel (Asher et al. 2008).

5.3.5 Possible Mechanism for Hydrogel Formation and CNP Enhancement

In order to improve the existing models of PVA-borax gelation to the field of CNP-containing PB hydrogels, it was necessary to consider the fundamentals of PVA-borate complex formation in water. Previous studies elucidated that, in dilute solution (borax concentration less than 25mM≈0.95 wt%), borax ($Na_2B_4O_7 \cdot 10H_2O$) dissociated completely into equal quantities of trigonal planar [$B(OH)_3$] (boric acid) and tetrahedral [$B(OH)_4^-$] (monoborate ions) that interchanged rapidly in water system (see eq.5.4) (Cui et al. 2009; Lin et al. 2000; Pezron et al. 1988; Sinton 1987), thus the authentic concentration of $B(OH)_4^-$ in the system was almost twice the initial borax concentration (Gao et al. 2008).

$$Na_2B_4O_7 + 7H_2O \rightarrow 2B(OH)_3 + 2B(OH)_4^- \qquad (5.4)$$

Cellulose, $(C_6H_{10}O_5)_n$, was a polyhydroxy polysaccharide consisting of a linear chain of thousands of β(1→4) linked D-glucose units. PVA was a long chain polymer that had a backbone of carbon molecules with numerous 1,3-cis-diol groups attached. In general, the mechanism of the crosslinking reaction of $B(OH)_4^-$ with polyhydroxy polymers (i.e., PVA and cellulose in this study) was considered to be a so-called monodiol and didiol complexation

(crosslink reaction) formed between vicinal diol units of polymer chains and $B(OH)_4^-$ (see eq. 5.5 and 5.6) (Angelova et al. 2011).

$$P + B(OH)_4^- \leftrightarrow PB(OH)_4^- + 2H_2O \quad (5.5)$$

$$2P + B(OH)_4^- \leftrightarrow P_2B(OH)_4^- + 4H_2O \quad (5.6)$$

where P referred to the cis-diol unit of the polymer (cellulose or PVA). $PB(OH)^-_4$ (complex I) and $P_2B(OH)^-_4$ (complex II) represented the free monodiol (1:1 stoichiometry) and didiol (2:1 stoichiometry) complex structures, respectively.

These complexes played the role of tie points for the physical network. Once a $B(OH)^-_4$ was attached to a PVA or cellulose chain (complex I), the anionic polymer chain behaved as a polyelectrolyte unless the $B(OH)^-_4$ was removed from it. In this case, a contribution of electrostatic repulsion between monodiol units was expected, leading to an expansion of the individual polymer chains (Lin et al. 2005). Since the PVA concentration (2.0 wt%) in each hydrogel was higher than the overlap concentration C* (1.54 wt%), both intra- and inter-molecular crosslink of (complex II) happened, and a gelation of these complexes was expected.

Based on the above-mentioned analysis, we first realized the multi-complexation between CNPs, PVA and borax in aqueous system in the present study. A plausible mechanism for the multi-complexation between cis-diol groups on the CNPs (or PVA) and $B(OH)^-_4$ is presented in Figure 5.4. PVA-borax aqueous system had a strong extended H-bonding network, which could further interact with active hydroxyl groups of cellulose through H-bonding. This was the first hierarchy of the hydrogel 3D-network via polymer-chain physical entanglement. It was reported that borax ions preferred to complex with glucose rather than physical cross-linking with the PVA polymer via hydrogen bonding (Manna and Patil 2010). However, because the chain excluded volume of CNPs was much greater than that of glucose molecules, thus considering the

presence of stereo-hindrance effect of the larger CNPs in the medium, the competitive binding equilibrium between PVA and CNPs was mitigated, which meant that the partial PVA-borax complexes would probably still exist with the addition of CNPs.

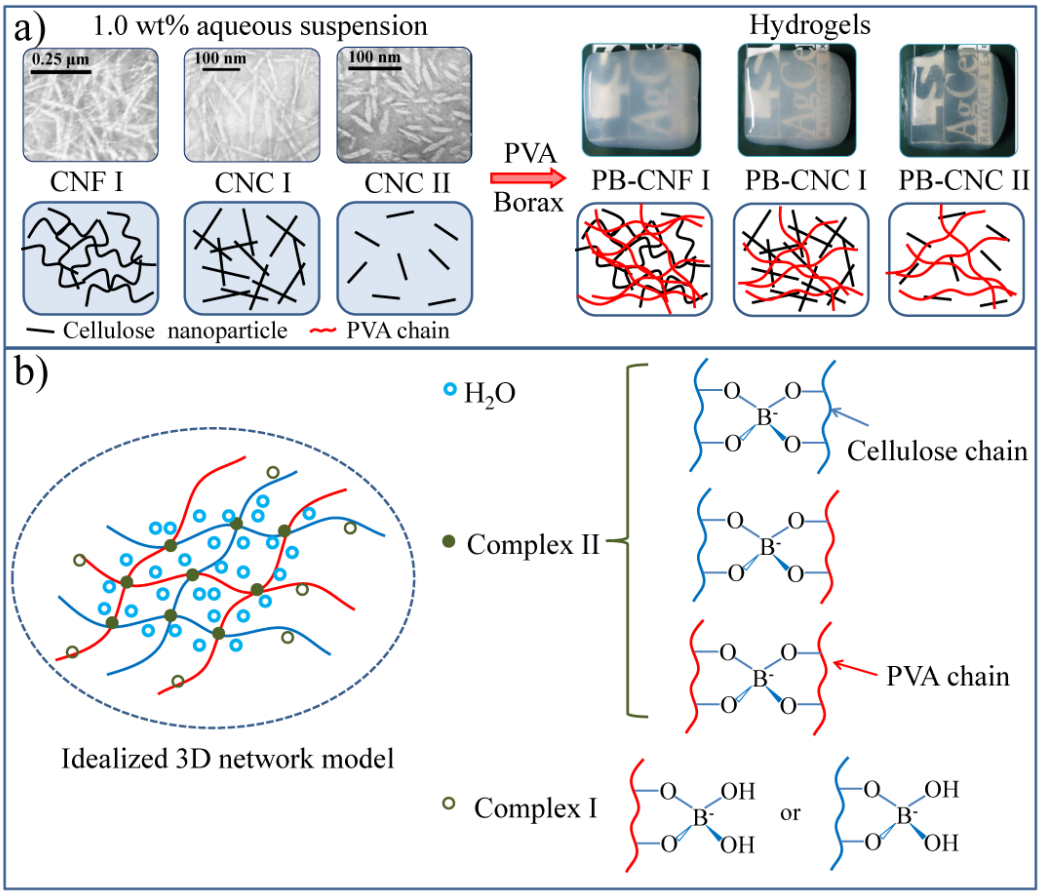

Figure 5.4 Schematic illustration of the three-dimensional network formation of hydrogel. (a) The first physical hierarchy of physical entanglement of polymer chains through H-bond, and the comparison of the dispersion state of CNPs with different minimum overlap concentration in the hydrogels, and (b) The second chemical hierarchy of the idealized 3D network structure formed by the ionic crosslinks among the five types of complexes and adjacent water molecules (hydrogen bonding system was not shown).

Therefore, two cis-diol pairs of different cellulose molecules or PVA chains were connected by a $B(OH)^-_4$ to form an reversible inter-chain crosslink. The coexistence of the three types of reversible crosslinks (PVA-$B(OH)^-_4$-CNP, PVA-$B(OH)^-_4$-PVA and CNP-$B(OH)^-_4$-CNP) gave rise to five types of complexes, namely complex I (PVA-$B(OH)^-_4$ and CNP-$B(OH)^-_4$) and

complex II (PVA-$B(OH)^-_4$-CNP, PVA-$B(OH)^-_4$-PVA and CNP-$B(OH)^-_4$-CNP), leading to the creation of a tridimensional network and solid-like performance of hydrogels (Scheme 1b). This was the second chemical hierarchy of the hydrogel 3D-network via plenty of reversible ionic crosslinks.

The formation of cross-links between pairs of vicinal hydroxyl groups from two polymer chains (PVA or CNP) and one $B(OH)^-_4$ (eq.6) was an exothermic process, and the cross-linking caused by formation of anionic complexes II with 2:l stoichiometry was cited as the chemical basis of enhanced viscosification in the system (Robb and Smeulders 1997; Sinton 1987). These negatively charged complexes and CNPs as well as free $B(OH)^-_4$ provided the electro-static repulsion for the system (Manna and Patil 2009), resulting in the homogeneous dispersion state of these components in hydrogels. In addition to the ionic bonding by borax, polyhydroxy PVA chains and CNPs could be cross-linked through hydrogen bonding and van der Waals type of interaction with the presence of water molecules, leading to the intra- and intermolecular cross-linking reactions and thus a physical entanglement (the first physical hierarchy). Consequently, the high-water-content mouldable hydrogel introduced by the present study was defined as the system formed when natural macromolecule (i.e., CNPs) and synthetic polymer (i.e., PVA) were physically entangled and chemically cross-linked with each other via the comprehensive cooperation of ionic bonding (offered by borax), hydrogen bonding and physical entanglement, which could entrap a big volume of water (Gao et al. 2008; Li et al. 2001). In other words, the conformation of the 3D-network polymer chains in these hydrogels was a consequence of a balance among physical entanglement via hydrogen bonding, intra- and intermolecular cross-linking effects, electrostatic repulsions among the complex units, the polymer-chain excluded volume and the electrostatic shielding effect of free Na^+ ions on the negatively charged

complexes (Angelova et al. 2011). In addition, it was reported that $B(OH)_3$ had a similar tendency to form diol complexes in the presence of PVA and cellulose. Nonetheless, $B(OH)_3$ hardly contributed to the formation of polyol gels, because the complexation reaction happened through the attachment of $B(OH)_3$ to adjacent alcohol groups of the same polymeric chain, which prevented cross-linking from taking place.

As described in dynamic oscillation measurements, the well-dispersed CNPs played an important multifunctional role on the 3D-network formation within the hydrogels, leading to a significant enhancement in toughness and viscoelasticity of the hydrogels. Before the combination, the PVA-borax-water system was not free-standing; and the 1.0 wt% CNP suspension or colloid was free-flowing. While after the incorporation of rigid CNPs, the crosslinking and entanglement restricted the segmental motions of PVA chains and CNPs, thus the system gradually solidified as temperature decreased and eventually formed a rubbery semisolid hydrogel that was easy to handle and mould at room temperature (Figure 5.1f and Figure 5.2c). Our previous study determined that the crystallinities of CNC I, CNF I and CNC II (66.4, 57.6 and 73.6%, respectively) were greater than that of PVA (30-50%) (Han et al. 2013; Peresin et al. 2010). Therefore, the incorporation of highly-crystallined CNPs into a softer chain PVA matrix with a lower degree of crystallinity led to a significant hardening effect. Additionally, the elastic modulus of the crystalline regions of cellulose I (138.0 GPa) was larger than that of cellulose II (88.0 GPa) in the direction parallel to the chain axis (Nishino et al. 1995), making cellulose I reinforced hydrogel absorb more energy under deformation than cellulose II reinforced hydrogel. Overall, the viscoelasticity and mechanical property of the hydrogels were in the order of PB-CNF I > PB-CNC I >PB-CNC II> PB, while their transparency was sequenced in a reverse order (Han et al. 2013c). As shown by UV-transmittance, rheology and

compression data (Han et al. 2013c), the differences in the enhancement effect and transparency originated in different nature of CNPs, such as aspect ratio, particle size, crystal structure, degree of crystallinity and surface charge. More importantly, for the three types of CNPs, this phenomenon could be further explained based on the understanding of the minimum overlap concentration and the supramolecular structures of these hydrogels.

The minimum overlap concentration (ϕ_c) for dispersions of rod-like CNPs can be approximated by the equation: $\phi_c = (D/L)^2$, where ϕ_c is the minimum overlap concentration in terms of volume fraction, L is the length and D is the diameter of cellulose rods (Bercea and Navard 2000). The ϕ_c values of CNF I, CNC I and CNC II were estimated to be 0.075, 0.363, 1.130 vol%, respectively. Based on the densities of CNPs (~1.59 g/cm^3) and deionized water (~1.00 g/cm^3) (OSullivan 1997), their corresponding mass concentrations were calculated. For CNC I suspension and CNF I colloid, the concentration of 1.00 wt% was above their corresponding ϕ_c values, 0.58 and 0.12 wt%, respectively, whereas the ϕ_c value of CNC II suspension was 1.80 wt%, higher than the concentration of 1.00 wt% used in this experiment. Accordingly, as demonstrated in the TEM images (Figure 5.4a), at the 1.00 wt% concentration level, long-curved CNF I chains achieved the entanglement, and needle-like CNC I possessed overlap junctions, while rod-like CNC II hardly contacted with each other and thus its inter-particle interactions were almost negligible. In particular, the pronounced entanglement of CNF I chains increased the probability that PVA chains contacted and tangled with CNF I chains, i.e., leading to the formation of physical junctions via polymer chain entanglements (Figure 5.4a). On the contrary, the quantity of junction zones of CNC II was much less than those of CNF I and CNC I, especially for the physical junctions formed by its self-entanglement (Figure 5.4a). For this reason, the cross-linking (entanglement) densities of hydrogels should be theoretically in the

order of PB-CNF I > PB-CNC I >PB-CNC II, which was in agreement with the G'_{∞}, G_c and t (relaxation time) results of oscillation test. After the cross-linking density was increased by the embedding of CNPs in PB system, plenty of water molecules became trapped inside the 3D network through hydrogen bond due to the hydrophilic nature of PVA and cellulose chains, thus producing a high-water-content hydrogel.

Once prepared, the hydrogels displayed some intriguing properties due to their supermolecular structure. The spaghetti-strand polymer chains gave the hydrogels a non-Newtonian fluid behavior. Under low stress, they could be stretched to form a thin film (Figure 5.1f). When a block of hydrogel was thrown onto a hard surface, it bounced slightly. The $B(OH)_4^-$ ion was shaped like a tetrahedron (four sides, each side is an equilateral triangle) with the boron in the center and the four OH groups at each corner. The temporary bonds formed between the $B(OH)_4^-$ and the OH groups on the sides of the PVA were reversible and exchangeable, which was previously confirmed by ^{11}B NMR investigations (Sinton 1987). The breaking and reformation of these bonds allowed the hydrogel to stretch under stress. The most abundant material in the hydrogels was water ($M_c \approx 96$ wt%), providing the liquid consistency of hydrogels. Therefore, two blocks of hydrogels could be completely merged into a single piece (Figure 5.2d). The uncommon fusion behavior of two separated PB-CNF I samples also suggested that the networks were in dynamic equilibrium and that the cross-linkages were not covalent. The ease of bonds break and reform resulted in the hydrogel rebuilt. Because all of the interactions were non-covalent, the constantly forming and dissociating of hydrogen bonds endowed the crosslinks with a dynamic nature, which allowed the PVA chains and CNPs to move relative to each other under external force. Hence these hydrogels could be manually moulded into various 3D shapes (Figure 5.2c). It was proposed that the activation energy for

breaking the four bonds constituting individual cross-links was 25 kJ/mol, while the heat of cross-link formation was 35 kJ/mol (Angelova et al. 2011). Responding accordingly to the external stimuli such as external force and temperature, the hydrogel exhibited self-healing ability and thermo-reversibility (determined by continuous step strain and temperature sweep tests). The PB-CNF I distorted under external force and then gradually wriggled back to its original shape (Figure 5.2e). This meant that the tangled PVA chains and CNPs were straighten out and then wriggled to become shorter again.

5.4 CONCLUSIONS

A new class of CNP-reinforced PVA-borax hydrogels was successfully fabricated through a facile approach in an aqueous medium. By respectively incorporating three types of well-dispersed CNPs (i.e., CNC I, CNC II and CNF I) to the PB aqueous system, the viscoelasticity, strength and stiffness of the hybrid hydrogels were pronouncedly enhanced. Highly-crystalline CNPs acted as multifunctional crosslinking agents and nanofillers to physically and chemically bridge the double-hierarchy 3D network of the hydrogels, clearly demonstrating the synergy between natural CNPs and synthetic polymer matrix. The nature of the CNPs (i.e., particle size, aspect ratio, crystal structure, and surface charge) affected the dynamic rheological properties of the composite hydrogels. The crosslinking density, viscoelasticity, stiffness of the obtained hydrogels were in the order of PB-CNF I > PB-CNC I >PB-CNC II > PB. Due to the reversible and exchangeable bonds dynamically formed between the $B(OH)_4^-$ and the OH groups on the sides of the PVA (and/or CNPs), the as-prepared free-standing, high elasticity and mouldable hydrogels exhibited self-recovery under continuous step strain and thermo-reversibility under temperature sweep. This novel material is not only environmentally friendly, but is mouldable into various free-standing 3D shapes as well because

of its high mechanical strength. In addition, the architectures and properties of hydrogels can be easily tailored by selecting different CNPs and crosslinking density. Our hydrogel contradicts the preconception that materials held together by supramolecular forces and mostly composed of water are weak (Wang et al. 2010), opening the door for many interesting applications, including artificial muscles, bioactuators, soft machines, tissue scaffolds and drug-delivery devices (Calvert 2009; Hu et al. 2000; Seliktar 2012; Van Vlierberghe et al. 2011).

5.5 REFERENCES

Agoda-Tandjawa G., Durand S., Berot S., Blassel C., Gaillard C., Garnier C. and Doublier J. L. 2010. Rheological characterization of microfibrillated cellulose suspensions after freezing. *Carbohydrate Polymers* 80:677-686.

Angelova L. V., Terech P., Natali I., Dei L., Carretti E. and Weiss R. G. 2011. Cosolvent Gel-like Materials from Partially Hydrolyzed Poly(vinyl acetate)s and Borax. *Langmuir* 27:11671-11682.

Asher S. A., Kimble K. W. and Walker J. P. 2008. Enabling Thermoreversible Physically Cross-Linked Polymerized Colloidal Array Photonic Crystals. *Chemistry of Materials* 20:7501-7509.

Bercea M. and Navard P. 2000. Shear Dynamics of Aqueous Suspensions of Cellulose Whiskers. *Macromolecules* 33:6011-6016.

Boluk Y., Zhao L. Y. and Incani V. 2012. Dispersions of Nanocrystalline Cellulose in Aqueous Polymer Solutions: Structure Formation of Colloidal Rods. *Langmuir* 28:6114-6123.

Cai J. and Zhang L. 2006. Unique gelation behavior of cellulose in NaOH/Urea aqueous solution. *Biomacromolecules* 7:183-189.

Calvert P. 2009. Hydrogels for Soft Machines. *Advanced Materials* 21:743-756.

Carretti E., Grassi S., Cossalter M., Natali I., Caminati G., Weiss R. G., Baglioni P. and Dei L. G. 2009. Poly(vinyl alcohol)-Borate Hydro/Cosolvent Gels: Viscoelastic Properties, Solubilizing Power, and Application to Art Conservation. *Langmuir* 25:8656-8662.

Chompff A. J. and Prins W. 1968. Viscoelasticity of Networks Consisting of Crosslinked or Entangled Macromolecules .2. Verification of Theory for Entanglement Networks. *Journal of Chemical Physics* 48:235-&.

Cui Q., Muscatello M. M. W. and Asher S. A. 2009. Photonic crystal borax competitive binding carbohydrate sensing motif. *Analyst* 134:875-880.

Fang Y. P., Takahashi R. and Nishinari K. 2004. A gel network constituted by rigid schizophyllan chains and nonpermanent cross-links. *Biomacromolecules* 5:126-136.

Gao S. J., Guo J. M. and Nishinari K. 2008. Thermoreversible konjac glucomannan gel crosslinked by borax. *Carbohydrate Polymers* 72:315-325.

Gouvea M. R., Ribeiro C., de Souza C. F., Marvila-Oliveira I., Lucyszyn N. and Sierakowski M. R. 2009. Rheological behavior of borate complex and polysaccharides. *Materials Science & Engineering C-Biomimetic and Supramolecular Systems* 29:607-612.

Han J. Q., Zhou C. J., Wu Y. Q., Liu F. Y. and Wu Q. L. 2013. Self-Assembling Behavior of Cellulose Nanoparticles during Freeze-Drying: Effect of Suspension Concentration, Particle Size, Crystal Structure, and Surface Charge. *Biomacromolecules* 14:1529-1540.

Hu Z. B., Lu X. H., Gao J. and Wang C. J. 2000. Polymer gel nanoparticle networks. *Advanced Materials* 12:1173-1176.

Ide N., Sato T., Miyamoto T. and Fukuda T. 1998. Thermoreversible hydrogel of short-chain O-(2,3-dihydroxypropyl)cellulose/borax aqueous solution. Microscopic versus macroscopic properties. *Macromolecules* 31:8878-8885.

Inoue T. and Osaki K. 1993. Rheological Properties of Poly(Vinyl Alcohol)/Sodium Borate Aqueous-Solutions. *Rheologica Acta* 32:550-555.

Ivanov A. E., Larsson H., Galaev I. Y. and Mattiasson B. 2004. Synthesis of boronate-containing copolymers of N,N-dimethylacrylamide, their interaction with poly(vinyl alcohol) and rheological behaviour of the gels. *Polymer* 45:2495-2505.

Kjøniksen A.-L. and Nyström B. 1996. Effects of Polymer Concentration and Cross-Linking Density on Rheology of Chemically Cross-Linked Poly(vinyl alcohol) near the Gelation Threshold. *Macromolecules* 29:5215-5222.

Kobayashi M., Chang Y. S. and Oka M. 2005. A two year in vivo study of polyvinyl alcohol-hydrogel (PVA-H) artificial meniscus. *Biomaterials* 26:3243-3248.

Koike A., Nemoto N., Inoue T. and Osaki K. 1995. Dynamic Light-Scattering and Dynamic Viscoelasticity of Poly(Vinyl Alcohol) in Aqueous Borax Solutions .1. Concentration-Effect. *Macromolecules* 28:2339-2344.

Li L., Thangamathesvaran P. M., Yue C. Y., Tam K. C., Hu X. and Lam Y. C. 2001. Gel network structure of methylcellulose in water. *Langmuir* 17:8062-8068.

Lin H. L., Liu Y. F., Yu T. L., Liu W. H. and Rwei S. P. 2005. Light scattering and viscoelasticity study of poly(vinyl alcohol)-borax aqueous solutions and gels. *Polymer* 46:5541-5549.

Lin H. L., Yu T. L. and Cheng C. H. 2000. Reentrant behavior of poly(vinyl alcohol)-borax semidilute aqueous solutions. *Colloid and Polymer Science* 278:187-194.

Liu D. G., Chen X. Y., Yue Y. Y., Chen M. D. and Wu Q. L. 2011. Structure and rheology of nanocrystalline cellulose. *Carbohydrate Polymers* 84:316-322.

Manna U. and Patil S. 2009. Borax Mediated Layer-by-Layer Self-Assembly of Neutral Poly(vinyl alcohol) and Chitosan. *Journal of Physical Chemistry B* 113:9137-9142.

Manna U. and Patil S. 2010. Glucose-Triggered Drug Delivery from Borate Mediated Layer-by-Layer Self-Assembly. *Acs Applied Materials & Interfaces* 2:1521-1527.

Nishino T., Takano K. and Nakamae K. 1995. Elastic-Modulus of the Crystalline Regions of Cellulose Polymorphs. *Journal of Polymer Science Part B-Polymer Physics* 33:1647-1651.

OSullivan A. C. 1997. Cellulose: the structure slowly unravels. *Cellulose* 4:173-207.

Peresin M. S., Habibi Y., Zoppe J. O., Pawlak J. J. and Rojas O. J. 2010. Nanofiber Composites of Polyvinyl Alcohol and Cellulose Nanocrystals: Manufacture and Characterization. *Biomacromolecules* 11:674-681.

Pezron E., Ricard A., Lafuma F. and Audebert R. 1988. Reversible Gel Formation Induced by Ion Complexation .1. Borax Galactomannan Interactions. *Macromolecules* 21:1121-1125.

Piculell L., Egermayer M. and Sjöström J. 2003. Rheology of Mixed Solutions of an Associating Polymer with a Surfactant. Why Are Different Surfactants Different? *Langmuir* 19:3643-3649.

Renkema J. M. S. and van Vliet T. 2002. Heat-induced gel formation by soy proteins at neutral pH. *Journal of Agricultural and Food Chemistry* 50:1569-1573.

Rezayati Charani P., Dehghani-Firouzabadi M., Afra E. and Shakeri A. 2013. Rheological characterization of high concentrated MFC gel from kenaf unbleached pulp. *Cellulose* 20:727-740.

Robb I. D. and Smeulders J. B. A. F. 1997. The rheological properties of weak gels of poly(vinyl alcohol) and sodium borate. *Polymer* 38:2165-2169.

Schubert B. A., Kaler E. W. and Wagner N. J. 2003. The microstructure and rheology of mixed cationic/anionic wormlike micelles. *Langmuir* 19:4079-4089.

Schultz R. K. and Myers R. R. 1969. The Chemorheology of Poly(vinyl alcohol)-Borate Gels. *Macromolecules* 2:281-285.

Seliktar D. 2012. Designing Cell-Compatible Hydrogels for Biomedical Applications. *Science* 336:1124-1128.

Shi X. W., Lu A., Cai J., Zhang L. N., Zhang H. M., Li J. and Wang X. H. 2012. Rheological Behaviors and Miscibility of Mixture Solution of Polyaniline and Cellulose Dissolved in an Aqueous System. *Biomacromolecules* 13:2370-2378.

Shin M. K., Spinks G. M., Shin S. R., Kim S. I. and Kim S. J. 2009. Nanocomposite Hydrogel with High Toughness for Bioactuators. *Advanced Materials* 21:1712-+.

Sinton S. W. 1987. Complexation chemistry of sodium borate with poly(vinyl alcohol) and small diols: a boron-11 NMR study. *Macromolecules* 20:2430-2441.

Slaughter B. V., Khurshid S. S., Fisher O. Z., Khademhosseini A. and Peppas N. A. 2009. Hydrogels in Regenerative Medicine. *Advanced Materials* 21:3307-3329.

Sun J. Y., Zhao X. H., Illeperuma W. R. K., Chaudhuri O., Oh K. H., Mooney D. J., Vlassak J. J. and Suo Z. G. 2012. Highly stretchable and tough hydrogels. *Nature* 489:133-136.

Van Vlierberghe S., Dubruel P. and Schacht E. 2011. Biopolymer-Based Hydrogels As Scaffolds for Tissue Engineering Applications: A Review. *Biomacromolecules* 12:1387-1408.

Wang Q., Mynar J. L., Yoshida M., Lee E., Lee M., Okuro K., Kinbara K. and Aida T. 2010. High-water-content mouldable hydrogels by mixing clay and a dendritic molecular binder. *Nature* 463:339-343.

Wang Y. X. and Chen L. Y. 2011. Impacts of nanowhisker on formation kinetics and properties of all-cellulose composite gels. *Carbohydrate Polymers* 83:1937-1946.

Yang J., Han C. R., Duan J. F., Ma M. G., Zhang X. M., Xu F., Sun R. C. and Xie X. M. 2012. Studies on the properties and formation mechanism of flexible nanocomposite hydrogels from cellulose nanocrystals and poly(acrylic acid). *Journal of Materials Chemistry* 22:22467-22480.

Yang J., Han C. R., Duan J. F., Xu F. and Sun R. C. 2013. Mechanical and Viscoelastic Properties of Cellulose Nanocrystals Reinforced Poly(ethylene glycol) Nanocomposite Hydrogels. *Acs Applied Materials & Interfaces* 5:3199-3207.

Yang X., Liu Q., Chen X., Yu F. and Zhu Z. 2008. Investigation of PVA/ws-chitosan hydrogels prepared by combined γ-irradiation and freeze-thawing. *Carbohydrate Polymers* 73:401-408.

Zhang W., Yang X. L., Li C. Y., Liang M., Lu C. H. and Deng Y. L. 2011. Mechanochemical activation of cellulose and its thermoplastic polyvinyl alcohol ecocomposites with enhanced physicochemical properties. *Carbohydrate Polymers* 83:257-263.

CHAPTER 6 OVERALL CONCLUSIONS

In the research described in this dissertation, various cellulose nanoparticles with diverse morphology, size, crystallinity and crystal structure were produced through different methods (i.e., ionic liquid treatment, alkaline pretreatment and/or acid hydrolysis, high-pressure homogenization). Some important physicochemical properties of the obtained cellulose nanoparticles, including pyrolysis behavior, size distribution, crystallinity index, dispersion state, crystal structure, surface charge, lyophilization-induced self-assembling behavior and transparency, were investigated and compared. The application of these cellulose nanoparticles was further realized in multifunctional cellulose-PVA-borax hydrogels. The conclusions of this study are as follows:

1) Regenerated cellulose nanoparticles (RCNs) including both elongated fiber and spherical structures were successfully prepared from microcrystalline cellulose and cotton using 1-butyl-3-methylimidazolium chloride followed by a high-pressure homogenization treatment. The crystalline structure of RCNs was cellulose II in contrast to the cellulose I form of the starting materials. Also, the RCNs have decreased crystallinity and crystallite size. The elongated RCNs produced from cotton and MCC had average lengths of 123 ± 34 and 112 ± 42 nm, and mean widths of 12 ± 5 and 12 ± 3 nm, respectively. The average diameter of spherical RCNs from MCC was 118 ± 32 nm. The dimensions of the various RCNs were all well fitted with an asymmetrical log-normal distribution function. The RCN has a two-step pyrolysis, different from raw MCC and cotton that have a one-step process. The properties of RCNs characterized in this study provided some fundamental information for the potential application of RCNs in biomedicine field such as tablet excipients.

2) Cellulose nanocrystals and cellulose nanofibers with I and II crystalline allomorphs were isolated from bleached wood fibers by alkaline pretreatment and acid

hydrolysis. The particle size, crystal structure and dispersion state were successfully controlled by using different acid concentration, alkaline pretreatment and high-pressure homogenization. Cellulose concentration, particle size, surface charge, and crystal structure significantly influenced the lyophilization-induced self-assembling behavior of the cellulose suspensions. During freeze drying, within the concentration range of 0.5 to 1.0 wt%, the gap between the self-assembled microfibers was small enough for the formation of hydrogen bonding and tight bonds with neighboring microfibers, thus cellulose particles self-organized into lamellar structured foam composed of aligned membrane layers with widths between 0.5 and 3 μm. At 0.05 wt%, due to the weakening of hydrogen bonding and interfacial attraction among the fibers, CNC I, CNF I, CNC II, and CNF II self-assembled into oriented ultrafine fibers with mean diameters of 0.57, 1.02, 1.50, and 1.00 μm, respectively, instead of the sheet-like structure. The size of self-assembled fibers became larger when more hydroxyl groups and fewer sulfates (weaker electrostatic repulsion) were on cellulose surfaces. Possible formation mechanism was inferred from ice growth and interaction between cellulose nanoparticles in liquid-crystalline suspensions. By freezing aqueous suspensions containing cellulose particles under suitable conditions, we demonstrated the possibility of building homogeneous scaffolds with aligned membrane layers or forming oriented ultra-fine fibers, opening their use as a template for fine-structure composites. Because of the tight association of the cellulose particles through the abundant inter-crystal hydrogen bonds, self-organized cellulose products induced by lyophilization presented extraordinary structural stability and integrity in aqueous media under mechanical stirring. For this reason, the morphology and structure of freeze-dried foam can be controlled by adjusting cellulose concentration, crystal structure, surface charges, and particle size to obtain a tailored template, showing great promises for many potential applications.

3) Cellulose nanoparticle (CNP) reinforced polyvinyl alcohol-borax (PB) hydrogels were successfully prepared through a facile approach in an aqueous medium. By respectively incorporating three kinds of well-dispersed CNPs (i.e., CNC I, CNC II and CNF I) to PB aqueous system, the compressive strength and toughness of the hybrid hydrogels were pronouncedly increased, clearly demonstrating the synergy between natural CNPs and synthetic polymer matrix. The obtained stiff, high-water-capacity (~96%), low-density (~1.1g/cm^3), translucence hydrogels exhibited birefringence textures and a higher transparency than the cyclic freeze-thawing prepared opaque hydrogels. Highly-crystalline CNPs not only tangled with PVA chains though numerous hydrogen bonds, but formed chemically crosslinked complexes with borax ions as well, thus acting as multifunctional crosslinking agents and nanofillers to physically and chemically bridge the 3D network of the hydrogels. These polymeric hydrogel materials are readily processed, and their preparation simplicity, availability from inexpensive renewable resources and performance tenability (e.g., through adjusting CNPs) are distinguishing features for many potential water-based applications. Being distinguished by high water content and diverse potential physical properties, they can be engineered to resemble the extracellular environment of the human tissues in ways that enable their application in biosensors, medical implants, and even drug-delivery devices.

4) A new class of cellulose nanoparticle (CNP) reinforced polyvinyl alcohol-borax (PB) hydrogels was successfully produced via a facile in-situ approach in an aqueous system. the Incorporation of well-dispersed CNPs to PB system significantly enhanced the viscoelasticity and stiffness of hydrogels. The obtained free-standing, high elasticity and mouldable hydrogels exhibited self-recovery under continuous step strain and thermo-reversibility under temperature sweep. The plausible mechanism for the multi-complexation among CNPs, polyvinyl alcohol

and borax was proposed to understand the relationship between the 3D network and hydrogel properties. Highly-crystalline CNPs acted as multifunctional crosslinking agents and nanofillers to physically and chemically bridge the double-hierarchy 3D network of the hydrogels, clearly demonstrating the synergy between natural CNPs and synthetic polymer matrix. The nature of the CNPs (i.e., particle size, aspect ratio, crystal structure, and surface charge) affected the dynamic rheological properties of the composite hydrogels. The crosslinking density, viscoelasticity, and stiffness of the obtained hydrogels were in the order of PB-CNF I > PB-CNC I >PB-CNC II > PB. This novel material is not only environmentally friendly, but is mouldable into various free-standing 3D shapes as well because of its high mechanical strength. In addition, the architectures and properties of hydrogels can be easily tailored by selecting different CNPs and crosslinking densities. Our hydrogel contradicts the preconception that materials held together by supramolecular forces and mostly composed of water are weak, opening the door for many interesting applications, including artificial muscles, bioactuators, soft machines, tissue scaffolds and drug-delivery devices.

APPENDIX: PERMISSION LETTER

For chapter 2:

ELSEVIER LICENSE
TERMS AND CONDITIONS

Aug 08, 2013

This is a License Agreement between jingquan han ("You") and Elsevier ("Elsevier") provided by Copyright Clearance Center ("CCC"). The license consists of your order details, the terms and conditions provided by Elsevier, and the payment terms and conditions.

All payments must be made in full to CCC. For payment instructions, please see information listed at the bottom of this form.

Supplier	Elsevier Limited The Boulevard,Langford Lane Kidlington,Oxford,OX5 1GB,UK
Registered Company Number	1982084
Customer name	jingquan han
Customer address	2000 brightside Dr. Apt 1521 BATON ROUGE, LA 70820
License number	3204311169017
License date	Aug 08, 2013
Licensed content publisher	Elsevier
Licensed content publication	Carbohydrate Polymers
Licensed content title	Characterization of cellulose II nanoparticles regenerated from 1-butyl-3-methylimidazolium chloride
Licensed content author	Jingquan Han,Chengjun Zhou,Alfred D. French,Guangping Han,Qinglin Wu
Licensed content date	15 May 2013
Licensed content volume number	94
Licensed content issue number	2
Number of pages	9

Start Page	773
End Page	781
Type of Use	reuse in a thesis/dissertation
Portion	full article
Format	electronic
Are you the author of this Elsevier article?	Yes
Will you be translating?	No
Order reference number	
Title of your thesis/dissertation	PREPARATION AND CHARACTERIZATION OF CELLULOSE NANOPARTICLES AND THEIR APPLICATION IN BIOPOLYMERIC NANOCOMPOSITES
Expected completion date	Oct 2013
Estimated size (number of pages)	150
Elsevier VAT number	GB 494 6272 12
Permissions price	0.00 USD
VAT/Local Sales Tax	0.0 USD / 0.0 GBP
Total	0.00 USD
Terms and Conditions	

INTRODUCTION

1. The publisher for this copyrighted material is Elsevier. By clicking "accept" in connection with completing this licensing transaction, you agree that the following terms and conditions apply to this transaction (along with the Billing and Payment terms and conditions established by Copyright Clearance Center, Inc. ("CCC"), at the time that you opened your Rightslink account and that are available at any time athttp://myaccount.copyright.com).

GENERAL TERMS

2. Elsevier hereby grants you permission to reproduce the aforementioned material subject to the terms and conditions indicated.

3. Acknowledgement: If any part of the material to be used (for example, figures) has appeared in our publication with credit or acknowledgement to another source, permission must also be sought from that source. If such permission is not obtained then that material may not be

included in your publication/copies. Suitable acknowledgement to the source must be made, either as a footnote or in a reference list at the end of your publication, as follows:

"Reprinted from Publication title, Vol /edition number, Author(s), Title of article / title of chapter, Pages No., Copyright (Year), with permission from Elsevier [OR APPLICABLE SOCIETY COPYRIGHT OWNER]." Also Lancet special credit - "Reprinted from The Lancet, Vol. number, Author(s), Title of article, Pages No., Copyright (Year), with permission from Elsevier."

4. Reproduction of this material is confined to the purpose and/or media for which permission is hereby given.

5. Altering/Modifying Material: Not Permitted. However figures and illustrations may be altered/adapted minimally to serve your work. Any other abbreviations, additions, deletions and/or any other alterations shall be made only with prior written authorization of Elsevier Ltd. (Please contact Elsevier at permissions@elsevier.com)

6. If the permission fee for the requested use of our material is waived in this instance, please be advised that your future requests for Elsevier materials may attract a fee.

7. Reservation of Rights: Publisher reserves all rights not specifically granted in the combination of (i) the license details provided by you and accepted in the course of this licensing transaction, (ii) these terms and conditions and (iii) CCC's Billing and Payment terms and conditions.

8. License Contingent Upon Payment: While you may exercise the rights licensed immediately upon issuance of the license at the end of the licensing process for the transaction, provided that you have disclosed complete and accurate details of your proposed use, no license is finally effective unless and until full payment is received from you (either by publisher or by CCC) as provided in CCC's Billing and Payment terms and conditions. If full payment is not received on a timely basis, then any license preliminarily granted shall be deemed automatically revoked and shall be void as if never granted. Further, in the event that you breach any of these terms and conditions or any of CCC's Billing and Payment terms and conditions, the license is automatically revoked and shall be void as if never granted. Use of materials as described in a revoked license, as well as any use of the materials beyond the scope of an unrevoked license, may constitute copyright infringement and publisher reserves the right to take any and all action to protect its copyright in the materials.

9. Warranties: Publisher makes no representations or warranties with respect to the licensed material.

10. Indemnity: You hereby indemnify and agree to hold harmless publisher and CCC, and their respective officers, directors, employees and agents, from and against any and all claims arising out of your use of the licensed material other than as specifically authorized pursuant to this license.

11. No Transfer of License: This license is personal to you and may not be sublicensed,

assigned, or transferred by you to any other person without publisher's written permission.

12. No Amendment Except in Writing: This license may not be amended except in a writing signed by both parties (or, in the case of publisher, by CCC on publisher's behalf).

13. Objection to Contrary Terms: Publisher hereby objects to any terms contained in any purchase order, acknowledgment, check endorsement or other writing prepared by you, which terms are inconsistent with these terms and conditions or CCC's Billing and Payment terms and conditions. These terms and conditions, together with CCC's Billing and Payment terms and conditions (which are incorporated herein), comprise the entire agreement between you and publisher (and CCC) concerning this licensing transaction. In the event of any conflict between your obligations established by these terms and conditions and those established by CCC's Billing and Payment terms and conditions, these terms and conditions shall control.

14. Revocation: Elsevier or Copyright Clearance Center may deny the permissions described in this License at their sole discretion, for any reason or no reason, with a full refund payable to you. Notice of such denial will be made using the contact information provided by you. Failure to receive such notice will not alter or invalidate the denial. In no event will Elsevier or Copyright Clearance Center be responsible or liable for any costs, expenses or damage incurred by you as a result of a denial of your permission request, other than a refund of the amount(s) paid by you to Elsevier and/or Copyright Clearance Center for denied permissions.

LIMITED LICENSE

The following terms and conditions apply only to specific license types:

15. **Translation**: This permission is granted for non-exclusive world**English** rights only unless your license was granted for translation rights. If you licensed translation rights you may only translate this content into the languages you requested. A professional translator must perform all translations and reproduce the content word for word preserving the integrity of the article. If this license is to re-use 1 or 2 figures then permission is granted for non-exclusive world rights in all languages.

16. **Website**: The following terms and conditions apply to electronic reserve and author websites:
Electronic reserve: If licensed material is to be posted to website, the web site is to be password-protected and made available only to bona fide students registered on a relevant course if:

This license was made in connection with a course, This permission is granted for 1 year only. You may obtain a license for future website posting, All content posted to the web site must maintain the copyright information line on the bottom of each image, A hyper-text must be included to the Homepage of the journal from which you are licensing at http://www.sciencedirect.com/science/journal/xxxxx or the Elsevier homepage for books at http://www.elsevier.com , and Central Storage: This license does not include permission for a scanned version of the material to be stored in a central repository such as that provided by

Heron/XanEdu.

17. **Author website** for journals with the following additional clauses:

All content posted to the web site must maintain the copyright information line on the bottom of each image, and the permission granted is limited to the personal version of your paper. You are not allowed to download and post the published electronic version of your article (whether PDF or HTML, proof or final version), nor may you scan the printed edition to create an electronic version. A hyper-text must be included to the Homepage of the journal from which you are licensing athttp://www.sciencedirect.com/science/journal/xxxxx . As part of our normal production process, you will receive an e-mail notice when your article appears on Elsevier's online service ScienceDirect (www.sciencedirect.com). That e-mail will include the article's Digital Object Identifier (DOI). This number provides the electronic link to the published article and should be included in the posting of your personal version. We ask that you wait until you receive this e-mail and have the DOI to do any posting.

Central Storage: This license does not include permission for a scanned version of the material to be stored in a central repository such as that provided by Heron/XanEdu.

18. **Author website** for books with the following additional clauses: Authors are permitted to place a brief summary of their work online only. A hyper-text must be included to the Elsevier homepage athttp://www.elsevier.com . All content posted to the web site must maintain the copyright information line on the bottom of each image. You are not allowed to download and post the published electronic version of your chapter, nor may you scan the printed edition to create an electronic version.

Central Storage: This license does not include permission for a scanned version of the material to be stored in a central repository such as that provided by Heron/XanEdu.

19. **Website** (regular and for author): A hyper-text must be included to the Homepage of the journal from which you are licensing athttp://www.sciencedirect.com/science/journal/xxxxx. or for books to the Elsevier homepage at http://www.elsevier.com

20. **Thesis/Dissertation**: If your license is for use in a thesis/dissertation your thesis may be submitted to your institution in either print or electronic form. Should your thesis be published commercially, please reapply for permission. These requirements include permission for the Library and Archives of Canada to supply single copies, on demand, of the complete thesis and include permission for UMI to supply single copies, on demand, of the complete thesis. Should your thesis be published commercially, please reapply for permission.

21. **Other Conditions**:

v1.6

Make Payment To:
Copyright Clearance Center

For chapter 3:

Title: **Self-Assembling Behavior of Cellulose Nanoparticles during Freeze-Drying: Effect of Suspension Concentration, Particle Size, Crystal Structure, and Surface Charge**

Author: Jingquan Han, Chengjun Zhou, Yiqiang Wu, Fangyang Liu, and Qinglin Wu

Publication: Biomacromolecules

Publisher: American Chemical Society

Date: May 1, 2013

American Chemical Society." Insert appropriate information in place of the capitalized words.

One-time permission is granted only for the use specified in your request. No additional uses are granted (such as derivative works or other editions). For any other uses, please submit a new request.

For chapter 4:

SPRINGER LICENSE
TERMS AND CONDITIONS

Oct 23, 2013

This is a License Agreement between jingquan han ("You") and Springer ("Springer") provided by Copyright Clearance Center ("CCC"). The license consists of your order details, the terms and conditions provided by Springer, and the payment terms and conditions.

All payments must be made in full to CCC. For payment instructions, please see information listed at the bottom of this form.

License Number	3254890146585
License date	Oct 23, 2013
Licensed content publisher	Springer
Licensed content publication	Cellulose
Licensed content title	Facile preparation of mouldable polyvinyl alcohol-borax hydrogels reinforced by well-dispersed cellulose nanoparticles: physical, viscoelastic and mechanical properties
Licensed content author	Jingquan Han
Licensed content date	Jan 1, 2013
Type of Use	Thesis/Dissertation
Portion	Full text
Number of copies	1
Author of this Springer article	Yes and you are the sole author of the new work
Order reference number	
Title of your thesis / dissertation	PREPARATION AND CHARACTERIZATION OF CELLULOSE NANOPARTICLES AND THEIR APPLICATION IN BIOPOLYMERIC NANOCOMPOSITES
Expected completion date	Oct 2013

Estimated size(pages)	150
Total	0.00 USD

Terms and Conditions

Introduction
The publisher for this copyrighted material is Springer Science + Business Media. By clicking "accept" in connection with completing this licensing transaction, you agree that the following terms and conditions apply to this transaction (along with the Billing and Payment terms and conditions established by Copyright Clearance Center, Inc. ("CCC"), at the time that you opened your Rightslink account and that are available at any time athttp://myaccount.copyright.com).

Limited License
With reference to your request to reprint in your thesis material on which Springer Science and Business Media control the copyright, permission is granted, free of charge, for the use indicated in your enquiry.

Licenses are for one-time use only with a maximum distribution equal to the number that you identified in the licensing process.

This License includes use in an electronic form, provided its password protected or on the university's intranet or repository, including UMI (according to the definition at the Sherpa website: http://www.sherpa.ac.uk/romeo/). For any other electronic use, please contact Springer at (permissions.dordrecht@springer.com or permissions.heidelberg@springer.com).

The material can only be used for the purpose of defending your thesis, and with a maximum of 100 extra copies in paper.

Although Springer holds copyright to the material and is entitled to negotiate on rights, this license is only valid, subject to a courtesy information to the author (address is given with the article/chapter) and provided it concerns original material which does not carry references to other sources (if material in question appears with credit to another source, authorization from that source is required as well).

Permission free of charge on this occasion does not prejudice any rights we might have to charge for reproduction of our copyrighted material in the future.

Altering/Modifying Material: Not Permitted
You may not alter or modify the material in any manner. Abbreviations, additions, deletions and/or any other alterations shall be made only with prior written authorization of the author(s) and/or Springer Science + Business Media. (Please contact Springer at (permissions.dordrecht@springer.com or permissions.heidelberg@springer.com)

Reservation of Rights
Springer Science + Business Media reserves all rights not specifically granted in the

combination of (i) the license details provided by you and accepted in the course of this licensing transaction, (ii) these terms and conditions and (iii) CCC's Billing and Payment terms and conditions.

Copyright Notice:Disclaimer
You must include the following copyright and permission notice in connection with any reproduction of the licensed material: "Springer and the original publisher /journal title, volume, year of publication, page, chapter/article title, name(s) of author(s), figure number(s), original copyright notice) is given to the publication in which the material was originally published, by adding; with kind permission from Springer Science and Business Media"

Warranties: None

Example 1: Springer Science + Business Media makes no representations or warranties with respect to the licensed material.

Example 2: Springer Science + Business Media makes no representations or warranties with respect to the licensed material and adopts on its own behalf the limitations and disclaimers established by CCC on its behalf in its Billing and Payment terms and conditions for this licensing transaction.

Indemnity
You hereby indemnify and agree to hold harmless Springer Science + Business Media and CCC, and their respective officers, directors, employees and agents, from and against any and all claims arising out of your use of the licensed material other than as specifically authorized pursuant to this license.

No Transfer of License
This license is personal to you and may not be sublicensed, assigned, or transferred by you to any other person without Springer Science + Business Media's written permission.

No Amendment Except in Writing
This license may not be amended except in a writing signed by both parties (or, in the case of Springer Science + Business Media, by CCC on Springer Science + Business Media's behalf).

Objection to Contrary Terms
Springer Science + Business Media hereby objects to any terms contained in any purchase order, acknowledgment, check endorsement or other writing prepared by you, which terms are inconsistent with these terms and conditions or CCC's Billing and Payment terms and conditions. These terms and conditions, together with CCC's Billing and Payment terms and conditions (which are incorporated herein), comprise the entire agreement between you and Springer Science + Business Media (and CCC) concerning this licensing transaction. In the event of any conflict between your obligations established by these terms and conditions and those established by CCC's Billing and Payment terms and conditions, these

terms and conditions shall control.

Jurisdiction
All disputes that may arise in connection with this present License, or the breach thereof, shall be settled exclusively by arbitration, to be held in The Netherlands, in accordance with Dutch law, and to be conducted under the Rules of the 'Netherlands Arbitrage Instituut' (Netherlands Institute of Arbitration).***OR:***

All disputes that may arise in connection with this present License, or the breach thereof, shall be settled exclusively by arbitration, to be held in the Federal Republic of Germany, in accordance with German law.

Other terms and conditions:

v1.3

If you would like to pay for this license now, please remit this license along with your payment made payable to "COPYRIGHT CLEARANCE CENTER" otherwise you will be invoiced within 48 hours of the license date. Payment should be in the form of a check or money order referencing your account number and this invoice number RLNK501142356.
Once you receive your invoice for this order, you may pay your invoice by credit card. Please follow instructions provided at that time.

Make Payment To:
Copyright Clearance Center
Dept 001
P.O. Box 843006
Boston, MA 02284-3006

For suggestions or comments regarding this order, contact RightsLink Customer Support:customercare@copyright.com or +1-877-622-5543 (toll free in the US) or +1-978-646-2777.

Gratis licenses (referencing $0 in the Total field) are free. Please retain this printable license for your reference. No payment is required.

VITA

Jingquan Han is currently a Ph.D candidate at Louisiana State University. He grew up in Harbin, Heilongjiang Province, China. After receiving his Bachelor's degree and Master's degree in wood science and technology at Northeast Forestry University, he came to the United States to pursue his Ph.D at Mississippi State University, working with Dr. Sheldon Shi. In 2010, he joined the Ph.D program in forest products in Louisiana State University, advised by Dr. Qinglin Wu. His research project deals with cellulose-based nanocomposites. So far, he has published more than ten journal articles. His research focuses on the preparation, characterization and application of cellulose nanocrystals and cellulose nanofibers, as well as cellulose-based biocomposites. The first part of the research is on characterization of cellulose II nanoparticles regenerated from ionic liquid, 1-butyl-3-methylimidazolium chloride, which has been published on *Carbohydrate Polymers* in 2013. The second part of the research is focused on the self-assembling behavior of cellulose nanoparticles during freeze drying process, which has been published on *Biomacromolecules* in 2013. On April, 2013, he was honored with the award for outstanding graduate student in polymer science and engineering by American Chemical Society. On June, 2013, he won the First Place of 2013 Wood Award honored by American forest product society (Two awards annually for outstanding wood science research). At present, he is the member of American Chemical Society (ACS), American forest product society (FPS) and Society of Wood Science and Technology (SWST). He is currently working as a research assistant at LSU. And he just got the letter of recommendation from the ESL-Spoken English committee of Louisiana State University. In addition, he has been awarded a four-year scholarship offered by China scholarship council (CSC) since 2010.